The University of Jordan
Authorization Form

I,   authorize the University of Jordan to supply copies of my Thesis/Dissertation to libraries or establishments or individuals on request.

Signature: S. Azar
Date: 18.8.2011

الجامعة الأردنيـــة
كلية الدراسات العليا

التاريـــخ: / /

نموذج رقم (١٦)
اقرار والتزام بالمعايير الأخلاقية والأمانة العلمية وقوانين الجامعة الأردنية وأنظمتها وتعليماتها لطلبة الدكتوراه

أنا الطالب: سعيد محمد شريف الأزعر الرقم الجامعي: (9060071)
تخصص: فيزياء الكليـــــة: العلوم

عنوان الاطروحة: ....
Investigation of Half-Metallic Behavior and spin polarization for the Heusler Alloys $Fe_{3-x}Mn_xZ$ (Z = Al, Ge, Sb): A First Principle Study

اعلن بأنني قد التزمت بقوانين الجامعة الأردنية وأنظمتها وتعليماتها وقراراتها السارية المفعول المتعلقة باعداد اطروحات الدكتوراه عندما قمت شخصيا" باعداد اطروحتي وذلك بما ينسجم مع الأمانة العلمية وكافة المعايير الأخلاقية المتعارف عليها في كتابة الأطروحات العلمية. كما أنني أعلن بأن اطروحتي هذه غير منقولة أو مستلة من أطاريح أو كتب أو أبحاث أو أي منشورات علمية تم نشرها أو تخزينها في أي وسيلة اعلامية، وتأسيسا" على ما تقدم فانني أتحمل المسؤولية بأنواعها كافة فيما لو تبين غير ذلك بما فيه حق مجلس العمداء في الجامعة الأردنية بالغاء قرار منحي الدرجة العلمية التي حصلت عليها وسحب شهادة التخرج مني بعد صدورها دون أن يكون لي أي حق في التظلم أو الاعتراض أو الطعن بأي صورة كانت في القرار الصادر عن مجلس العمداء بهذا الصدد.

توقيع الطالب: S. Aazar التاريخ: ١٨/ ٨ / ٢٠١١

INVESTIGATION OF HALF-METALLIC BEHAVIOR AND SPIN POLARIZATION FOR THE HEUSLER ALLOYS $Fe_{3-x}Mn_xZ$ (Z= Al, Ge, Sb): A FIRST PRINCIPLE STUDY

By
Said Moh'd Sharif Al Azar

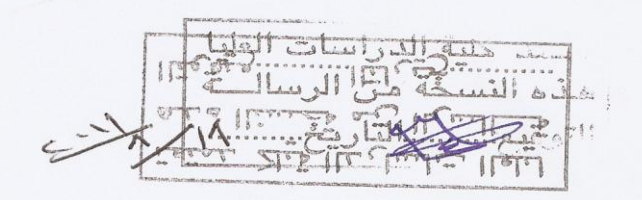
Supervisor
Dr. Jamil Mahmoud Khalifeh, Prof.

Co-Supervisor
Dr. Bothina Abdallah Hamad

This dissertation was submitted in partial fulfillment of the requirements for the Doctor of Philosophy Degree in Physics

Faculty of Graduate Studies
University of Jordan

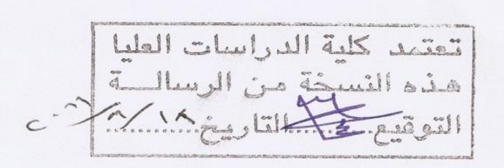
August 2011



COMMITTEE DECISION

This dissertation (INVESTIGATION OF HALF-METALLIC BEHAVIOR AND SPIN POLARIZATION FOR THE HEUSLER ALLOYS $Fe_{3-x}Mn_xZ$ (Z= Al, Ge, Sb): A FIRST PRINCIPLE STUDY) was Successfully defended and approval on (July, 2011).

Examination Committee	Signature
Dr. Jamil Mahmoud Khalifeh Prof. of Theoretical Solid State Physics	J M Khalifeh
Dr. Noureddine Chair Associate Prof. of Mathematical physics	N. Chair
Dr. Dia-Eddin Mahmoud Arafah Prof. of Experimental Solid State Physics	D.E. Arafah
Dr. Sami Hussein Mahmoud Prof. of Experimental Solid State Physics	S mahmood
Dr. Marouf Khalil Abdallah Prof. of Molecular Spectroscopy	
Dr. Ibrahim O. Abu-Aljarayesh Prof. of Solid State Physics (Yarmouk University)	Ibrahim



It is my pleasure to dedicate this work to my family, parents, wife, kids, brothers and friends. After the jasmine revolution in Tunis and 25th January revolution in Egypt I dedicate this work to all young people, who work to change the current status.

“Imagination is more important than knowledge. For knowledge is limited to all we now know and understand, while imagination embraces the entire world, and all there ever will be to know and understand.“

– Albert Einstien

ACKNOWLEDGMENTS

I would like to express my deepest gratitude to my supervisor Professor Jamil Khalifeh and to co-supervisor Dr. Bothina Hamad for their interest, assistance, guidance, support, encouragement and for wealthy and enlightening discussions throughout this work.

Also I present here my deep thanks to the committee members, for their reading of this dissertation and for their comments. I would also like to take the opportunity to thank all my colleagues in theoretical and computational physics lab, Dr. Ahmad Mosa for helping me in using the code, Dr. Ehsan Irikat, Dr. Mohammad Dalabeeh and the others for their continuous interest and the lovely discussions. I have benefitted greatly from many fruitful discussions with them.

I acknowledge Cyprus Institute where part of the numerical calculations was carried out using their Planck cluster at the Cyprus Institute, Nicosia, Cyprus. I present special thanks to Patrick Fitzhenry (Cyprus Institute) for his help and support of parallel compiling of Wien2k code in the cluster, and each person contributed to the success of this work.

The love, encouragements and support of my family are sincerely appreciated.

Thank you all very much.

CONTENTS

LIST OF FIGURES

LIST OF TABLES

ABSTRACT

INVESTIGATION OF HALF-METALLIC BEHAVIOR AND SPIN POLARIZATION FOR THE HEUSLER ALLOYS $Fe_{3-x}Mn_xZ$ (Z= Al, Ge, Sb): A FIRST PRINCIPLE STUDY

By

Said Moh'd Sharif Al Azar

Supervisor

Prof. Dr. Jamil Mahmoud Khalifeh

Co-supervisor

Dr. Bothina Abdallah Hamad

In this contribution we study, with ab initio accuracy over a wide concentration range, the effect of the main-group elements on the electronic structures and magnetic properties of bulk $Fe_{3-x}Mn_xZ$(Z=Al, Ge, Sb) alloys series. Manganese concentration and the main-group elements (Z) play an important role in the electronic structure and magnetic properties of these alloys. The influence of Mn concentration and main-group elements on the electronic and magnetic structure are discussed in this work. Furthermore, the half-metallic behavior is investigated for the alloys in the series.

Density functional theory based on full potential linearized augmented plane-wave (FPLAPW) method is used to investigate the structural, electronic and mag-

netic properties of $Fe_{3-x}Mn_xZ$ (Z= Al, Ge, Sb) Heusler alloys, where ($0 \leqslant x \leqslant 3$). The electronic exchange-correlation energy is treated under the generalized gradient approximation (GGA) according to the Perdew-Becke-Ehrenzhof parametrization.

Alloys with $x<2$ are found to exhibit a ferromagnetic phase, whereas the rest show ferrimagnetic phase. The total spin magnetic moment shows a trend consistent with Slater-Pauling type behavior with values ranging from 0 to 4 μ_B. Alloys with $x \geqslant 1$ are found to be half metallic with indirect band gaps along Γ-X symmetry line for stoichiometric and direct band gaps for nonstoichiometric alloys. It was found that Mn rich composition of $Fe_{3-x}Mn_xZ$ alloys have high spin polarization. The magnetic hyperfine field of Z atoms increases with increasing Mn concentration, and varies from -49.8 kG at x=0 to 98.9 kG at x=3 for Al, from 69.3 kG at x=0 to 373.9 kG at x=3 for Ge and from 220.2 x=0 to 550.3 kG at x=3 for Sb. Our calculated values for the spin magnetic moment and hyperfine fields closely agree with the previous experimental and calculational results.

CHAPTER 1

INTRODUCTION

In this contribution, the effects of varying Mn concentration and changing the main-group elements in Heusler alloys on the electronic and magnetic properties are studied in computational frameworks to investigate the half-metallicity behavior.

Half-metallic materials form a quite diverse collection of materials with very different chemical and physical properties and even the origin of the half-metallicity can be quite distinct. Half-metallic ferromagnets were initially predicted by de Groot and his collaborators in 1983 using first-principle calculations [de Groot *et al.* 1983]. Half-metals are hybrids between normal metals and insulators. At $T = 0$K, the majority-spin band is crossed by the Fermi level as in a normal metal while the Fermi level falls within a gap in the minority-spin band as in insulators (as T grows from zero, the gap in the minority spin component gets smaller, but still contains the Fermi level, and some thermally exited minority spin electrons cross the gap; the minority spin channel then behaves as a semiconductor.) leading to a perfect 100 % spin-polarization at the Fermi level. Such compounds should have a fully spin-polarized current.

The strong motivation to study half-metals is connected to perspective use in spintronics applications [Ẑutić *et al.* 2004] as spin-injection devices [Datta and Das 1990], spin-filters [Kilian and Victora 2000], tunnel junctions [Tanaka *et al.* 1999], giant magnetoresistance(GMR) [Caballero *et al.* 1998, Hordequin *et al.* 1998] colossal magnetoresistance(CMR) and tunnel magnetoresistance(TMR) [Moodera *et al.* 1995] devices. Half-metals are very interesting conceptually; they provide an opportunity to probe in a clear form some essentially many-particle effects [Irkhin and Katstelson 1990], whereas for

generic metallic system the Landau Fermi-liquid theory works [Nozieres 1964, Vonsovsky and Katsnelson 1989], most correlation effects being hidden in a parameter renormalization (such as effective mass, magnetic moment etc.). So that, the usually many-body effects lead only to renormalization of the quasiparticle parameters in the sense of Landau's Fermi liquid theory, the electronic *liquid* being *qualitatively* similar to the electron *gas* (see, e.g., [Nozieres 1964]). On the other hand, non-quasiparticle (NQP) states in half-metals, filling up the half-metallic gap states, are not described by the Fermi liquid theory [Chioncel *et al.* 2003, Chioncel *et al.* 2006]. At the same time, the new half-metals predicted and investigated are growing on the basis of band-structure calculations, as well as attempts to understand better the features of electronic structure and chemical bonding which are relevant to half-metallicity.

The most interesting half-metallic materials are the two types of Heusler alloys [Buschow and van Engen 1981, Galanakis nd Mavropoulos 2003b], some oxides (e.g CrO_2 and Fe_3O_4) [Schwarz 1986, Goodenough 1971, Camphausen *et al.* 1972], the CMR doped manganites (e.g. $La_{0.7}Sr_{0.3}MnO_3$) [Soulen *et al.* 1998, Park *et al.* 1998], the pyrites(e.g CoS_2) [Shishidou *et al.* 2001], the CMR double perovskites(e.g. Sr_2FeReO_6 and Sr_2FeMoO_6) [Bandyopadhyay 2000], the transition metal chalcogenides(e.g CrSe) [Xie *et al.* 2003] and pnictides (e.g CrAs and CrSb) [Galanakis 2002a, Galanakis nd Mavropoulos 2003b] in the zinc-blende or wurtzite structures, the europium chalcogenides(e.g EuS) [Horne *et al.* 2004], and the diluted magnetic semiconductors (e.g Mn impurities in Si or GaAs) [Sanvito and Hill 2000, Akai 1998]. Although the prospects for finding new half-metallic compounds are quite limited, prospects are better for finding new solid solutions with robust half-metallicity.

There are three main aspects responsible for the peculiarities of half-metallic ferromagnets:

1. The crystal structure.

2. The valence electron count, and covalent bonding.

3. The large exchange splitting of the Mn 3d electron band states.

There is no intrinsic behavior that constitutes the unmistakable signature of a half-metal. However, the 100 % spin polarization is considered an intrinsic property of half-metals. Conventional ferromagnetic metals are unsuitable source for spin polarization P into a semiconductor [Schmidt *et al.* 2000]. Adding the spin degree of freedom to the conventional electronic devices has several advantages like non-volatility, increased data processing speed, decreased electric power consumption and increased integration densities. In addition an increase of the efficiency of optoelectronic devices and even a self-assembled quantum computer [Bandyopadhyay 2000] are envisaged.

Generation of spin polarization usually means to create a nonequilibrium spin population. This can be achieved in several ways. While traditionally spin has been oriented using optical techniques in which circularly polarized photons transfer their angular momenta to electrons, for device applications electrical spin injection is more desirable. In electrical spin injection a magnetic electrode is connected to the sample. When the current drives spin-polarized electrons from the electrode to the sample, nonequilibrium spin accumulates there. Spin detection, which is also part of a generic spintronics scheme, typically relies on sensing the changes in the signals caused by the presence of nonequilibrium spin in the system. The common goal in many spintronics devices is to maximize the spin detection sensitivity to the point that it detects not the spin itself, but changes in the spin states.

Although it is not exactly clear how many half-metals are known to exist at this moment, half- metallic magnetism as phenomenon has been generally accepted. Formally the expected 100 % spin polarization of the charge carriers in a half-metallic ferromagnet. Half-metallic ferromagnet is a hypothetical situation that can only be approached in the limit of vanishing temperature and neglecting spin-orbital interactions. However, at low temperatures (as compared with the Curie temperature (T_C) which exceeds 1000 K for some half-metallic ferromagnets) and minor spin-orbit interactions, a half-metal deviates so markedly from a normal material. The half metallicity predicted by electronic structure

calculations becomes practically applicable. Nevertheless, direct experimental evidences of half-metallic structure for specific compounds are still rather poor. Perhaps, the unique method of testing genuine, bulk, half-metallic properties remains the spin-resolved positron annihilation [Hanssen *et al.* 1990]. This underexposed technique enables the direct measurement of the spin-polarization in the bulk. Advanced techniques borrowed from semiconductor technologies which access spatially resolved spin polarization at the Fermi level would be interesting alternatives for positron annihilation. Much other experimental effort is being devoted to measure half-metallicity and expected to advance the field such as, spin-polarized photoemission [Bona *et al.* 1985, Park *et al.* 1998], the spin-polarized scanning tunneling microscope (STM) [Wiesendanger *et al.* 1990], spin- polarized tunneling [Tanaka *et al.* 1999], infrared reflectance spectroscopy [Mancoff *et al.* 1999] and Andreev reflection measurement [Soulen *et al.* 1998] to measure the spin polarization.

Half-metallicity is not an easy property to detect experimentally. The reason for the experimental difficulties in not entirely clear. One constraint in preparing thin-film samples is that they cannot be arbitrarily annealed without changing the film structure. Thus, the degree of substitutional atomic disorder is expected to be higher in thin films than in bulk samples. A struggle to verify the existence of the gap in the minority-spin channel experimentally has not been reachable yet. The difficulty to observe a gap at finite temperatures is an intrinsic property of a ferromagnetic half-metal. In a many-particle description, thermal excitations of the electronic system are formed by superpositions of majority-spin states and virtual magnons appear in the Kohn-Sham (KS) band gap.

Because of the experimental complications , during a long time the electronic structure calculations play an important role in the search for new half-metals as well as the introduction of new concepts like half-metallic antiferromagnetism. The density functional theory (DFT) has become the primary tool for calculation of electronic structure in condensed matter, and is increasingly important for quantitative studies of molecules and other finite systems. The strength of a computational

approach is that it does not need samples: even nonexistent materials can be calculated. But in such an endeavor a clear goal should be kept in mind. Certainly, computational studies can help in the design of new materials, but the challenge is not so much in finding exotic physics in materials that have no chance of ever being realized. However, the main attention will be devoted to materials that either exist or are (meta) stable enough to have a fair chance of realization.

Despite the diverse successes of the electronic structure calculations, they have weaknesses as well. Most of the calculations are based on density functional theory in the local density approximation (LDA) or generalized gradient approximation (GGA). It is well known that these methods underestimate the band gap for many semiconductors and insulators, typically by 30%. It has been assumed that these problems do not occur in half-metals since their dielectric response is that of a metal. This assumption was disproved recently [Katsnelson *et al.* 2008]. On the other hand, electronic structure calculations usually deal with an ideally-ordered bulk stoichiometric compound. In some cases, there are electronic structure calculations of the surface, variations in stoichiometry, anti-site defects and non-stoichiometry which are usually ignored in the calculations. Sometimes the half- metallic character is robust with respect to these variations, but more often is not.

A calculation on the half-metal $La_{0.7}Sr_{0.3}MnO_3$ employing the GW approximation (that gives a correct description of band gaps in many semi-conductors) leads to a half-metallic band gap 2 eV in excess to the DFT value [Kino *et al.* 2003]. The consequences of this result are possibly dramatic: if it were valid in half-metallic magnetism in general, it would imply that many of the materials, showing band gaps in DFT based calculations of insufficient size to encompass the Fermi energy, are actually in reality *bona fide* half-metals.

1.1 Previous Studies

The first compound claimed to be half-metals was NiMnSb identified by calculations of de Groot et al [de Groot *et al.* 1983]. These authors coined the term half-metal. The first oxide to be identified as a half-metal in this way was CrO_2

[Schwarz 1986, Goodenough 1971]. It is worth to mention here that both CrO_2 and Fe_3O_4 [Camphausen *et al.* 1972] had been identified as half-metals before the term was actually coined.

The full-Heusler alloys Co_2MnSi and Co_2MnGe were the first half-metallic ferromagnets to be predicted where they have been found, by electron energy band calculations, to possess full spin polarization [Ishida *et al.* 1995]. Both the energy gap and the spin gap increase as the Z atomic number decreases in Co_2MnZ compounds [Picozzi *et al.* 2002]. The Co_2MnSi and Co_2MnGe films are grown and by performing superconducting quantum interference device (SQUID) magnetometry and point contact Andreev reflection measurements, a saturation magnetization of $5.01 \leqslant \mu \leqslant 5.15\ \mu_B$ and spin-polarization of about 50%-60% were obtained. Brown *et al.* using polarized neutron diffraction measurements have shown that there is a finite very-small minority spin density of states (DOS) at the Fermi level [Borwn *et al.* 2000] instead of an absolute gap in agreement with the ab initio calculations of Kübler *et al.* [Kübler *et al.* 1983]. The origin of minority band gap of the full Heusler alloys was discussed by Galanakis *et al.* [Galanakis *et al.* 2002c]. Furthermore, Heusler alloys of the type Fe_2MnZ [Fujii *et al.* 1995] and Mn_2FeZ [Luo *et al.* 2008] have been proposed theoretically to show half-metallicity which attracted more studies. Moreover, there has been an upsurge of interest in the ordered compound containing Fe. The V-based Heusler alloys Mn_2VZ (Z=Al, Ga, In, Si, Ge, Sn) are predicted to demonstrate half-metallic ferrimagnetism [Özdogan *et al.* 2006].

de Groot *et al.* [de Groot and Buschow 1986] proposed that the high magneto-optical Kerr effect (MOKE) of PtMnSb compound is intimately connected with its unusual half-metallic band structure. Much experimental effort is being devoted to NiMnSb [Tanaka *et al.* 1999, Schlomka *et al.* 2000] but nevertheless highly spin-polarized carrier injection from NiMnSb has not yet been achieved. The spin-resolved positron annihilation [Hanssen *et al.* 1990] , the first attempts to prove the half-metallicity used electron transport measurement, and infrared reflectance spectroscopy [Mancoff *et al.* 1999], support the half-metallic nature of NiMnSb.

Neutron diffraction gives a magnetic moment of 4.0(2) μ_B [Helmholdt *et al.* 1984] and resistivity does not exhibit the low-temperature T^2 dependence characteristic for spin-flip scattering [Otto *et al.* 1989].

Extrinsic factors, such as structural defects, including atomic disorder, and surface or interface states, may explain the low experimental spin polarization [Ritche *et al.* 2003, Singh *et al.* 2004, Kämmerer *et al.* 2004, Singh *et al.* 2006]. The disorder in the sublattices [Orgassa *et al.* 1999] or impurity bands included by a high concentration of point defects [Picozzi *et al.* 2004] may close the gap in the bulk half-metallic Heusler alloys as shown by first-principle calculations. Also the half-metallicity in Heusler alloys is a crystal symmetry effect [Fang *et al.* 2002]. It is very sensitive to any imperfections in the crystal. Concerning relevant theoretical studies, there is a substantial literature devoted to a variety of ordered Heusler-type phases and related systems where many previous studies are concerned to explain the effect of impurities concentration on the structural and magnetic properties of Heusler alloys. An extensive review of $Fe_{3-x}T_xSi$ alloys for various transition metals (T) has been carried out by Niculescu *et al.* [Niculescu *et al.* 1983]. Pugaczowa-Michalska *et al.* [Pugaczowa-Michalska *et al.* 2005] examined the effect of local environment on the formation of local magnetic moments of $Fe_{3-x}Mn_xAl$ alloys in the concentration range $0 \leqslant x \leqslant 0.5$. Recently, Hamad *et al.* [Hamad *et al.* 2010] studied theoretically the electronic structure and spin polarization of bulk $Fe_{3-x}Mn_xSi$ and $Fe_{3-y}MnSi_y$ alloys and found that the half-metallic behavior starts at x=0.75 with a small direct band gap that increases for higher Mn concentrations. In the case of $Fe_{3-x}Cr_xSi$, the $L2_1$ phase is found to be more stable one in comparison with the A15 phase for $x \leq 1.5$ beyond which the A15 phase become more stable [Hamad *et al.* 2011]. Recently, Hülsen *et al.* concluded that a large interval of Mn concentrations ranging from 25 % to 60 % in $Co_{2-x}Mn_{x+1}Si$ where potentially half-metallic compositions may occur [Hülsen *et al.* 2009]. The first-principle calculations of the quaternary Heusler alloys $Co_2[Cr_{1-x}Mn_x]Al$, $Co_2Mn[Al_{1-x}Sn_x]$ and $[Fe_{1-x}Co_x]_2MnAl$ [Galanakis 2004] demonstrated the Slater-Pauling behavior

and half-metallic properties.

According to the study of Sasioglu *et al.*, in the full-Heusler alloys, the nearest neighbor exchange coupling has an influence on the magnetic order [Sasioglu *et al.* 2005]. In normal Heusler alloys, if the manganese atoms are nearest neighbors, the coupling between their moments tends to be antiferromagnetic [Acet *et al.* 2002, Liu *et al.* 2006]. Luo *et al.* concluded recently that the magnetic structure of Mn_2NiZ(Z= In, Sn, Sb) is mainly determined by the main-group element Z instead of the distance between the Mn atoms [Luo *et al.* 2009]. The highest magnetic moment ($6\mu_B$) and Curie-temperature (1100K) in the classes of Heusler compounds as well as half-metallic ferromagnets was revealed for Co_2FeSi [Wurmehl *et al.* 2005]. It was found empirically that the Curie temperature of Co_2-based Heusler compounds can be estimated from a nearly linear dependence on the magnetic moment [Fesher *et al.* 2006].

1.2 Statement of Purpose

The goal of this research work is to study, with ab initio accuracy over a wide concentration range, the effect of the main-group elements on the electronic structures and magnetic properties of the bulk of $Fe_{3-x}Mn_xZ$(Z=Al, Ge, Sb) alloy series. Manganese concentration and the main-group elements (Z) play an important role in the electronic structure and magnetic properties of these alloys. The influence of Mn concentration and main-group elements on the electronic and magnetic structure are discussed in this work. Furthermore, the half-metallic behavior is investigated for some alloys in the series. We are thus able to delineate clearly how the majority and minority spin states and magnetic moments in Fe_3Ge develop when the Fe atoms in the lattice is substituted by Mn atoms, and/or when Ge is replaced by a metalloid of different valence.

1.3 Thesis Outline

This dissertation is designed as follow: after the brief introduction, the main theoretical assumptions and approaches of the half-metallic behavior are introduced in chapter two. The third chapter explains the computational details and the theory

frameworks used to find the physical characters and behaviors. In chapter four, we arrange the results and discussion. Finally, conclusions and open issues are discussed in chapter five.

CHAPTER 2

HALF-METALLICITY AND HEUSLER ALLOYS

2.1 Half-Metal Classifications

Coey and Venkatesan proposed that we can classify the half-metallic ferromagnets with encompassing localized and itinerant electron systems as well as possible semimetals and semiconductors [Coey *et al.* 2002]. The definition of half-metal as mentioned before is semiconducting for electrons of one spin orientation, whereas it is metallic for electrons with the opposite spin orientation. Such compounds exhibit nearly fully spin polarized conduction electrons. It assumes a magnetically-ordered state with an axis to define the spin quantization. For clarity, we consider

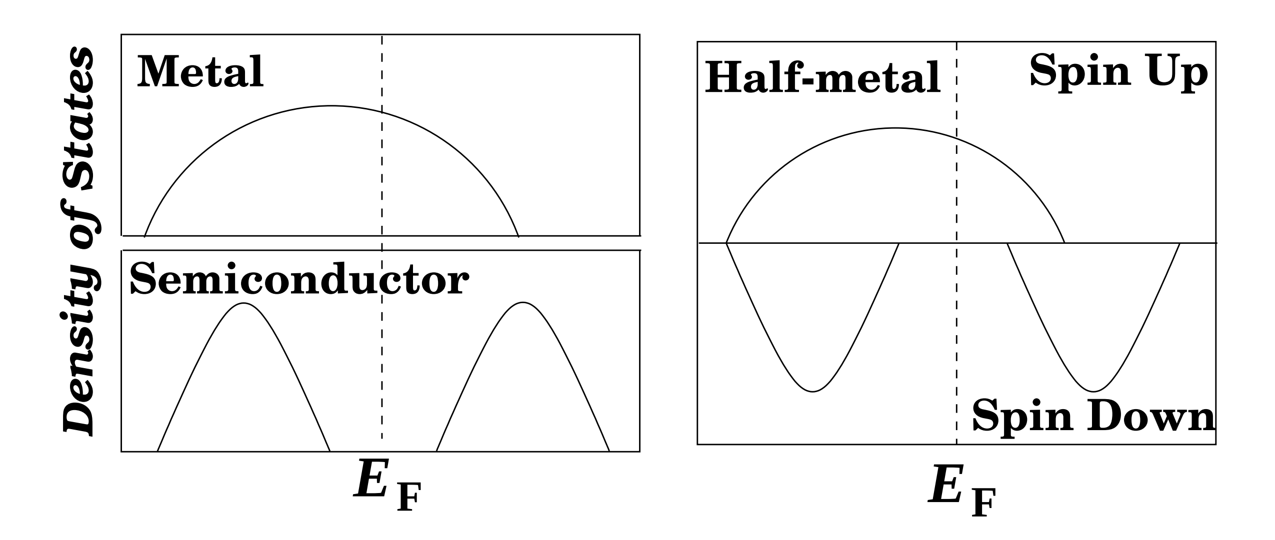


Figure 2.1.1. A schematic representation of the density of states of a half-metal as compared to a normal metal and a normal semiconductor.

the situation at zero temperature, where there is no spin mixing. A schematic representation of the density of states of a half-metal as compared to normal metal and a normal semiconductor is shown in Fig. 2.1.1. Normal ferromagnets, even strong ferromagnets, are not half-metals. Cobalt and nickel, for example, have fully spin-polarized d-bands with a filled majority spin $3d$ band and only minority d electrons at the Fermi level E_F, but the Fermi level also crosses the $4s$ band which is almost unpolarized so there is a density of both majority and minority electrons. In order to arrive at a situation where there are only majority or minority electrons at E_F, it is necessary to reorder the $3d$ and $4s$ bands of the ferromagnetic transition metals. This can be achieved by pushing the bottom of the $4s$ band up above E_F or by lowering the Fermi level below the bottom of the $4s$ band. Otherwise a hybridization gap might be introduced at E_F for one spin orientation. However, all half-metals are stoichiometric compounds, or solid solutions.

The two possible types for compounds of a single spin orientation at E_F are types I_A and I_B. Type I_A half-metal is metallic for majority electrons, but semiconducting for minority electrons, whereas the opposite is true for the type I_B half-metal. Half-metallic oxides where $4s$ states are pushed above E_F by s-p hybridization are of type I_A when the transition metal has less than five d-electrons, but those with more than five d-electrons are of type I_B. Likewise, half-metallic Heusler alloys with heavy p-elements like Sb tend to have the $3d$ levels depressed below the $4s$ band

Table 2.1.1. The Half-metals classification after Coey and Venkatesan (2002).

Type	DOS	Conductivity	spin up electrons at E_F	spin down electrons at E_F	example
I_A	half-metal	metallic	itinerant	none	CrO_2 or NiMnSb
I_B	half-metal	metallic	none	itinerant	Sr_2FeMoO_6 or Mn_2VAl
II_A	half-metal	nonmetallic	localized	none	
II_B	half-metal	nonmetallic	none	localized	Fe_3O_4
III_A	metal	metallic	itinerant	localized	$(La_{0.7}Sr_{0.3})MnO_3$
III_B	metal	metallic	localized	itinerant	
IV_A	semimetal	metallic	itinerant	localized	
IV_B	semimetal	metallic	localized	itinerant	$Tl_2Mn_2O_7$
V_A	semiconductor	semiconducting	few, itinerant	none	GaAs
V_B	semiconductor	semiconducting	none	few, itinerant	

edge by p-d hybridization. In a second class of half-metals, type II, the carriers at the Fermi level are in a band that is sufficiently narrow for them to be localized. The heavy carriers form polarons and conduction is then by hopping from one site to another with the same spin [Ziese and Thompson 2001]. A third class of half-metals (type III), known as “transport half-metals“, have localized majority carriers and itinerant (delocalized) minority carriers or vice versa [Nadgorny *et al.* 2001]. A density of states exists for both sub-bands at E_F, but the carriers in one band have a much larger effective mass than those in the other. So far as electronic transport properties are concerned, only one sort of carriers contributes significantly to the conduction.

Normally, there is no connection or confusion between a half-metal and a semimetal. A semimetal, of which bismuth is the textbook example, has small and equal numbers of electrons and holes (0.01 per atom) due to a fortuitously small overlap between valence and conduction bands. However, when the semimetal is magnetically ordered with a great difference in effective mass between electrons and holes, it is possible that it could resemble the previous type of half-metal. We refer to these as type IV half-metals. The type V half-metals are the magnetic semiconductors such as (Ga,Mn)As. This classification is summarized in Table 2.1.1.

2.2 Heusler Alloys

Heusler alloys [Heusler 1903] are ternary, magnetic, intermetallic compounds. They have attracted attention since they show great potential for spintronics and electromechanical applications. Fig. 2.2.3 shows the different elements combinations to form Heusler alloys [Fruchart *et al.* 1988]. Heusler alloys are good model systems for studying localized $3d$ metallic magnetism since there is negligible overlap between the $3d$ wave functions.

Intermetallic Heusler alloys are amongst the most attractive half-metallic systems due to the high Curie temperatures, low coercivities, and the structural similarity to the binary semiconductors such as GaAs. From a chemical point of view, Heusler alloys are found with two phases. Firstly, the half-Heusler with

formula XYZ ($C1_b$) can be stabilized only through covalent bonding, therefore, the semi-Heusler alloys are observed only if Z=Sn, Sb and Bi (within a narrow range of a valence electrons number). Secondly, the full-Heusler alloys with formula X_2YZ ($L2_1$) exist when Z=Al, Si, Ga, Ge, Sn, Sb and Bi. As the XYZ structure is far from compact, it may be a subject to lattice instabilities; disorder generally occurs between *d* metals, the more so the closer they are in the periodic table. The crystal structure of the two types of Heusler compounds is illustrated in Fig. 2.2.2 with the position shifted by $(\frac{1}{4}, \frac{1}{4}, \frac{1}{4})$ with respect to the standard $Fm\bar{3}m$ cell to make the CsCl superstructure better visible.

Recently, functional materials such as Heusler alloys have attracted attention in fundamental and engineering science because of their new possible applications and phenomena. Heusler alloys have been the subject of experimental and theoretical interest due to three unique properties. Firstly, Half-metallic behavior [de Groot *et al.* 1983]. Secondly, magnetic shape memory effect [Webster *et al.* 1984]: the magnetic shape memory alloys are types of magnetic materials that undergo structural transformation upon changing applied magnetic

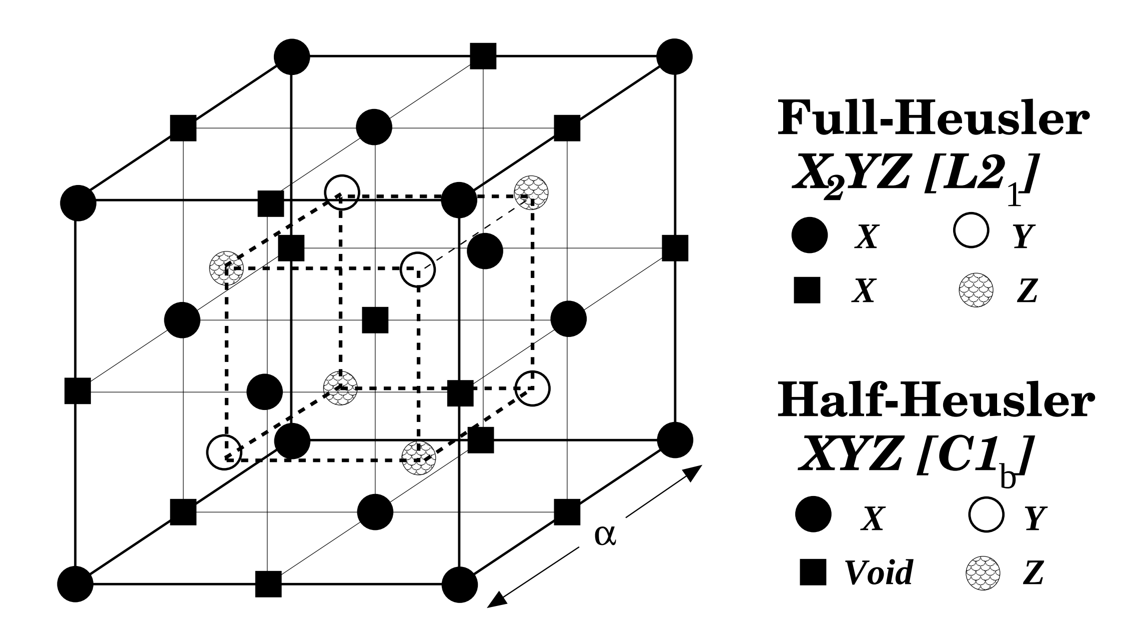


Figure 2.2.2. The conventional lattice cell for both Full and Half Heusler alloys structure.

field. Thirdly, the inverse magnetocaloric effect [Pecharsky and Gschneidner 1997] where some magnetic materials possess a reversible change in temperature caused by exposing the material to a changing magnetic field.

In addition to these three unique properties, Heusler alloys also provide fundamental aspects for magnetism in complex systems, so that electronic structure calculations from first-principles have been extensively used to predict new materials with predefined properties in order to maximize the efficiency of devices. Furthermore, the rule described by Kübler *et al.* [Kübler *et al.* 1983], states that Mn on the B-site in Heusler compounds tends to have a high, localized magnetic moment [Kübler *et al.* 1983, Weht and Pickett 1999, Buschow and van Engen 1981] plays an important role in Heusler compounds. According to electronic structure calculations, in the $C1_b$ compounds, Mn on the B-site has a magnetic moment of approximately 4 μ_B. Mn may be formally described as Mn^{3+}, with a d^4 configuration. Table 2.2.2 summarized the magnetic phenomena that may be studied using Heusler alloys.

Table 2.2.2. Magnetic phenomena that may occur in Heusler alloys.

Magnetic phenomena	Example	Reference
Localized $3d$ metallic magnetism	Cu_2MnAl	[Kübler *et al.* 1983]
Weak itinerant ferromagnetism	Co_2TiSn	[van Engen *et al.* 1983]
Pauli paramagnet	Ni_2TiSn	[Pierre *et al.* 1993]
Heavy fermion like	Fe_2TiSn and	[Ślebarski *et al.* 2000]
	Fe_2VAl	[Nishino *et al.* 1997]
Antiferromagnetism	Ni_2MnAl	[Fujita *et al.* 2004]

In Heusler alloys there is always some degree of chemical disorder, heavily influencing many of their physical properties. In the fully ordered Heusler alloy, the four sublattices A, B, C, and D are occupied by X, Y, X, and Z atoms, respectively giving the $L2_1$ type of order. In reality, this fully ordered state is hard to be attained, and there is a variety of possible disorder. When X atoms remain ordered and full disorder occurs between Y and Z sites only, the alloys have a B2 (CsCl

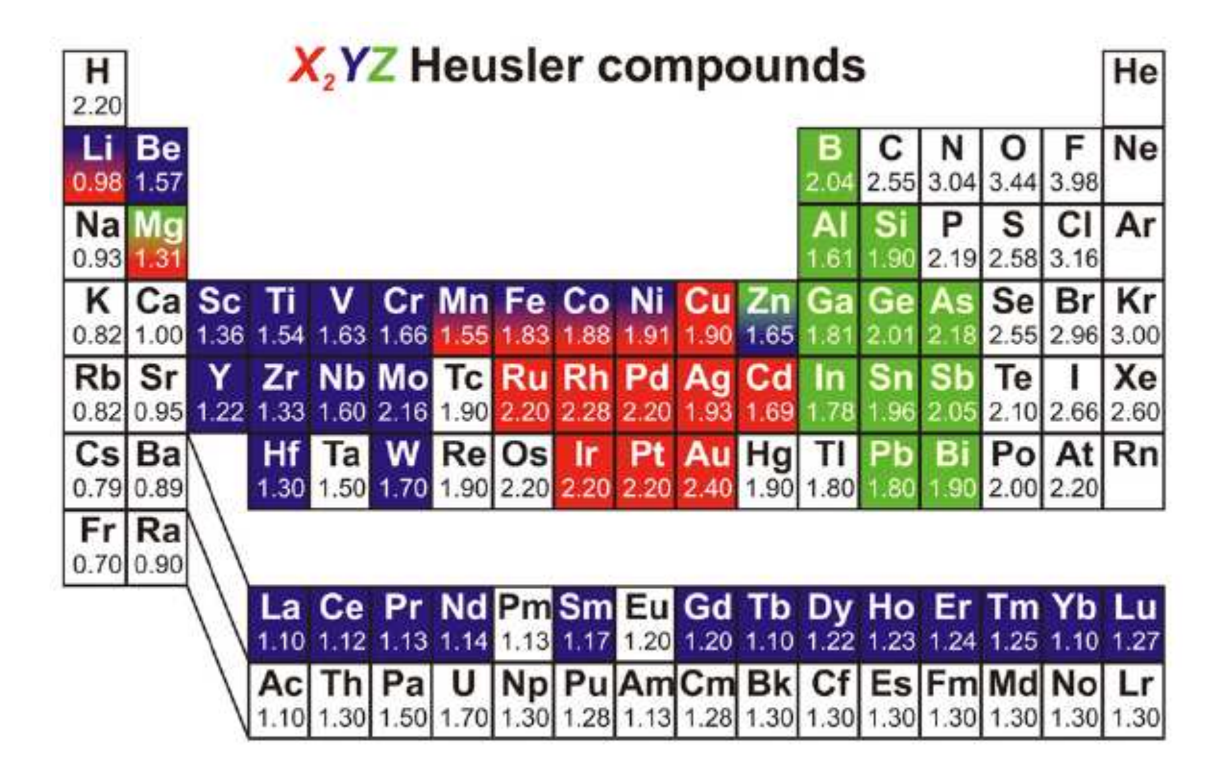


Figure 2.2.3. Periodic table of the elements. The huge number of Heusler alloys can be formed by combination of the different elements according to the color scheme.

type) structure. If disorder occurs between one X site and either Y or Z sites, the atomic arrangement may lead to a DO$_3$ (Fe_3Al) structure, and eventually, an A2 structure occurs if there is the atomic arrangement when random order occurs between all X, Y and Z sites. The X atoms serve primarily to determine the lattice parameter, while the Z atoms mediate the interaction between the Y d states. In the next two subsection we discuss separately the two type of Heusler alloys.

2.2.1 Half-Heusler Alloys

The half-Heusler compounds have a stoichiometric composition of XYZ crystallize in the face centered cubic (C1$_b$) structure with one formula unit per unit cell. The space group is F$\bar{4}$3m (No. 216) and the prototype is AgAsMg or AlLiSi. The Y and Z atoms are located at $4a(0, 0, 0)$ and $4b(\frac{1}{4}, \frac{1}{4}, \frac{1}{4})$ positions forming the rock

salt structure arrangement. The X atom is located in the octahedral coordinated pocket, at one of the cube center positions, $4c(\frac{1}{2}, \frac{1}{2}, \frac{1}{2})$ and leave the $4d$ $(\frac{3}{4}, \frac{3}{4}, \frac{3}{4})$ empty. When the Z-atomic positions are empty, the structure is analogous to zinc blende structure which is common for large number of semiconductors.

2.2.2 Full-Heusler Alloys

The crystal structure of ternary intermetallic compounds of the formula X_2YZ is cubic (see Fig. 2.2.4) with three different structural phases as illustrated in the following diagram.

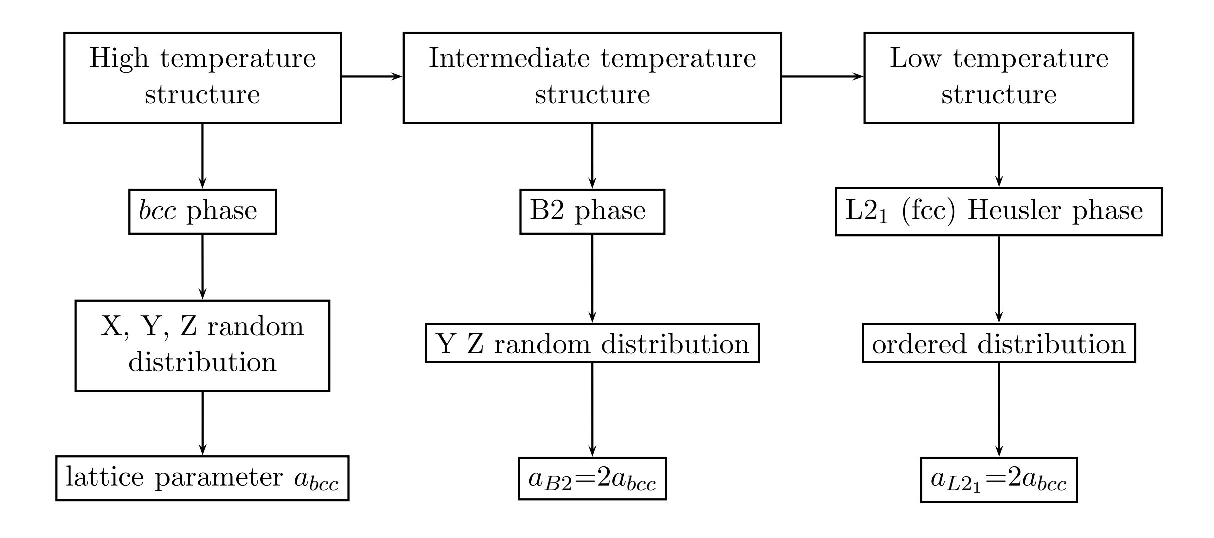


Figure 2.2.4. The three structural phases of the ternary compounds with formula X_2YZ.

The B2 and the $L2_1$ phases develop from the high temperature *bcc* structure by chemical ordering of the atoms on the 4 *fcc* sublattices in two steps via two second order structural phase transitions (*bcc*-B2) and (B2-$L2_1$). Experimentally, the Fe_3Ge with DO_3 structure are recorded between 90 K to 978 K; above this temperature the material transforms to the hexagonal phase [Deijver *et al.* 1976].

The X_2YZ full Heusler compounds crystallize in the cubic $L2_1$ structure (space group no 225:$Fm\bar{3}m$), the prototype is $AlCu_2Mn$. In general , the X and Y atoms

are transition metals and Z is a main group element. The X atoms are placed on the Wyckoff positions $8c$ $(\frac{1}{4}, \frac{1}{4}, \frac{1}{4})$. The Y and Z atoms are located on $4a$ (0,0,0) and $4b$ $(\frac{1}{2}, \frac{1}{2}, \frac{1}{2})$ positions, respectively. The cubic $L2_1$ structure is looked upon as four interpenetrating *fcc* sub-lattices, two of which are equally occupied by X. The two X-site *fcc* sub-lattices combine to form a simple cubic sub-lattice. The Y and Z atoms occupy alternatively the center of the simple cubic sub-lattice resulting in a CsCl-type superstructure. The cubic X_2YZ compounds are not only found with the $AlCu_2Mn$ type structure but also with the $CuHg_2Ti$ type structure. The $CuHg_2Ti$ type structure (called inverse Heusler) exhibits T_d symmetry (space group no 216:$F\bar{4}3m$). In this structure X atoms occupy the nonequivalent $4a$ and $4c$ Wyckoff positions at (0,0,0) and $(\frac{1}{4}, \frac{1}{4}, \frac{1}{4})$, the Y and Z are located at $4b$ $(\frac{1}{2}, \frac{1}{2}, \frac{1}{2})$ and $4d$ $(\frac{3}{4}, \frac{3}{4}, \frac{3}{4})$ position, respectively. All four positions adopt T_d symmetry and there is no position with O_h symmetry. This structure is similar to the XYZ compounds with $C1_b$ structure, but with the vacancy filled by an additional X atom. This structure is frequently observed if the nuclear charge of the Y element is larger than the one of the X element from the same period.

2.3 The Spin Polarization

Functionality of devices that exploit charge as well as spin degrees of freedom depends in a crucial way on the behavior of the spin polarization of current carriers [Prinz 1998]. Unfortunately, many potentially promising half-metallic systems exhibit dramatic decrease in the spin polarization. Crystal imperfections [Ebert and Schutz 1991], interfaces [de Wijs and de Groot 2001], and surfaces [Galanakis 2003a] constitute important examples of static perturbations of the ideal periodic potential which affect the states in the half-metallic gap.

In addition, several other depolarization mechanisms were suggested that are based on magnon and phonon excitations [Dowben and Skomski 2003, Skomski 2007]. The coupling between atomic moments can be treated in terms of the Heisenberg-type interactions. The sign and magnitude of the exchange constants determines whether the spin structure is collinear or not [Sandratskii 2001].

The definition of spin polarization is

$$P = \frac{N_{\uparrow}(E_F) - N_{\downarrow}(E_F)}{N_{\uparrow}(E_F) + N_{\downarrow}(E_F)} \tag{2.1}$$

where $N_{\uparrow}(E_F)$ and $N_{\downarrow}(E_F)$ are the density of states at the E_F for the majority and minority spin state, respectively.

The question why DOS is so often used as a measure of spin polarization, even though such definition is irrelevant for transport properties? The answer is coming from experiment where the most common way to perform tunneling or similar experiments is to follow the details of the contact conductance as a function of voltage. In such a case the characteristic scale for the voltage change is the superconducting gap. The normal state electronic structure does not change over such a small energy range, so the only important factor is the variation of the superconducting DOS with energy. The normal state DOS and velocity can be assumed constant and factored out. Of course, it is not the case when two different sheets of the Fermi surface, or two different spin channels, are compared [Mazin 1999].

The filling of the energy gap is very important for possible applications of half-metals in spintronics: in fact, half-metals have deciding advantages only provided that $T \ll T_C$. Since a single-particle Stoner-like theory leads to much less restrictive (but unfortunately completely wrong) inequality $T \ll \Delta$, where $\Delta = 2|I|S$ is the spin splitting, here I is the Stoner parameter and S is the total spin, the many-body treatment of the spin-polarization problem (inclusion of collective spin-wave excitations) is crucial. Generally, for temperatures which are comparable with T_C, there are no essential difference between half-metallic and "ordinary" ferromagnets since the gap is filled.

Itoh *et al.* [Itoh *et al.* 2000] calculated the polarization for a ferromagnet-insulator magnetic tunnel junction with and without spin fluctuations in a thermally randomized atomic potential. The results indicate that the effect of spin fluctuations is significant. The idea of spin fluctuations was further developed by Ležaić *et al.* [Ležaić *et al.* 2006] by considering the competition between hybridization and

thermal spin fluctuation in the NiMnSb which drop abruptly at temperatures much lower than the Curie point.

2.4 Generalized Slater-Pauling Rule

Slater-Pauling rule states that the magnetic moment is determined by the mean number of valence electrons per atom. The integer spin moment criterion, or an extension of it to cover the case of a solid solution, is a necessary but not a sufficient condition for half-metallicity. High spin polarization and magnetic moment of half-metallic ferromagnets can be treated within the generalized Slater-Pauling rule [Galanakis *et al.* 2002c, Fesher *et al.* 2006]. According to the original formulation by Slater and Pauling, the magnetic moments μ of $3d$ elements and their binary compounds can be described by the mean number of valence electrons n_V per atom. A plot of μ versus magnetic valence $\mu(n_M)$ is called the generalized Slater-Pauling rule, as described by Kübler *et al.* [Kübler *et al.* 1983]. According to Hund's rule it is often favorable that the majority d states are fully occupied ($n_{d\uparrow} = 5$). Starting from $m = 2n_\uparrow - n_V$, this leads to the definition of the magnetic valence as $n_M = 10 - n_V$, so that the magnetic moment per atom is given by $m = n_M + 2n_{sp\uparrow}$.

In the case of localized moments, the Fermi energy is pinned in a deep valley of the minority electron density. This constrains $n_{d\downarrow}$ to be approximately 3, and $m = n_V - 6 - 2n_{sp\uparrow}$. Half-metallic ferromagnets are supposed to exhibit a real gap in the minority density of states where the Fermi energy is pinned. Then the number of occupied minority states has to be an integer. Thus, the Slater-Pauling rule will be strictly fulfilled with the spin magnetic moment per atom $m = n_V - 6$. The situation for the half-metallic and non-half-metallic full Heusler alloys is shown in Fig. 2.4.5.

For ordered compounds with different kinds of atoms it may be more convenient to consider the total spin magnetic moment M_t of all atoms of the unit cell. This quantity scales with the number of valence electron Z_t: $M_t = Z_t - 18$ for the half-Heusler and $M_t = Z_t - 24$ for the full-Heusler alloys. Thus in both types of compounds the spin magnetic moment per unit cell is strictly integer for the

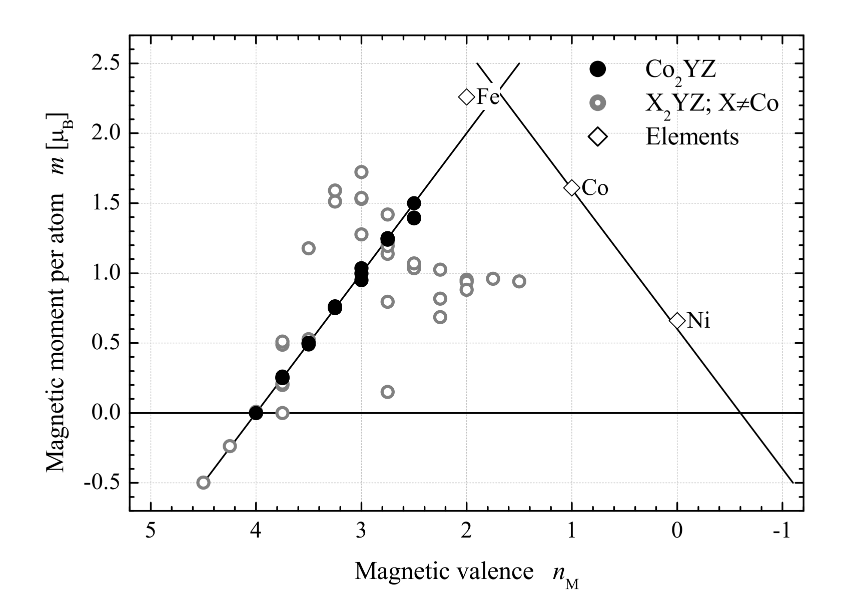


Figure 2.4.5. Slater Pauling graph for Heusler compounds.

half-metallic ferromagnet (HMF) (see Fig. 2.4.6). On the other hand, for alloys with non-integer site occupancies like the quaternaries $X_2Y_{1-x}Y_xZ$ the moment may become non-integer depending on the composition, even for the HMF state.

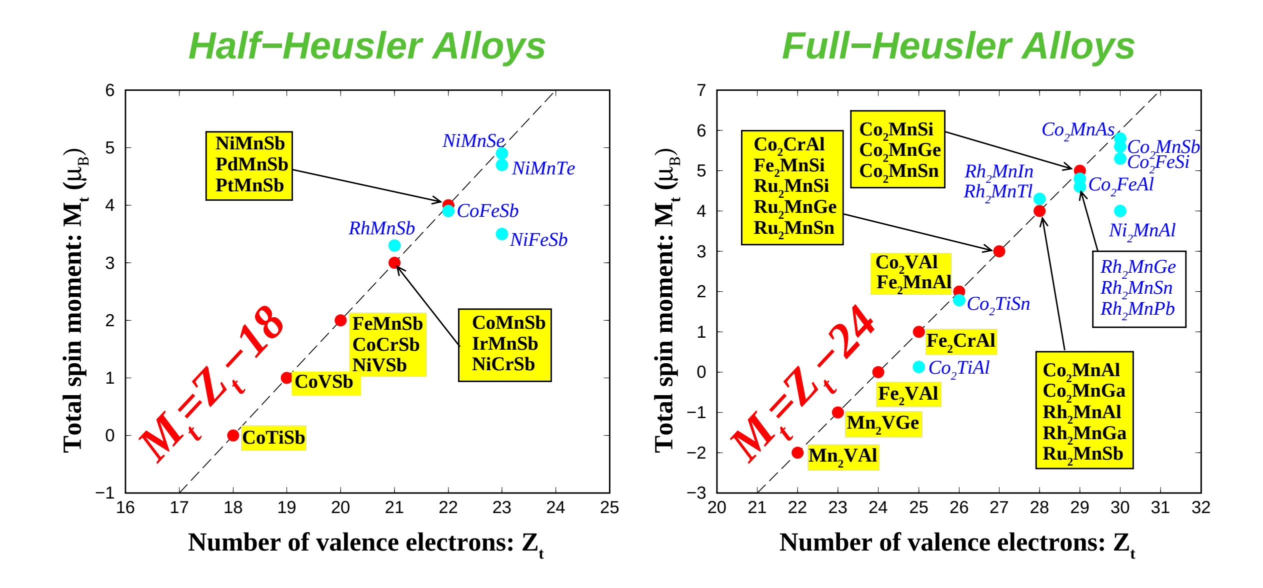


Figure 2.4.6. The Slater-Pauling behavior and the calculated total spin moments for full- and half-Heusler alloys.

Moreover, the generalized Slater-Pauling rule for non-stoichiometric full-Heusler can be expressed as

$$M_{tot} = N_v - 24n_Z \tag{2.2}$$

where n_Z is the number of Z atoms in the unit cell.

An interesting feature of the half-metallic Heusler alloys is that the Rhodes-Wolfarth ratio p_C/p_s (p_C are the effective moments, p_s the saturation moments) can be essentially smaller than unity [Katsnelson *et al.* 2008]. It therefore follows that the inequality $p_C/p_s < 1$ is a striking property of half-metallic ferromagnets, which could be used in their preliminary experimental identification.

This behavior may be explained by a change of electronic structure. The temperature dependence of magnetic moment in the paramagnetic state may be due to short-range magnetic order (local densities of states are similar to those in the ferromagnetic state). It is expected that such changes are particularly large in the case of half-metals and they should be of qualitative nature. From the many-electron model point of view, the decrease of the local moment with increasing temperature is connected with the absence of corrections to ground state magnetization of the type magnon damping. However, such corrections do occur at high temperatures.

2.5 Origin of the Gap

In half-metals, there are two different gaps that have to be defined. The band gap, which is the energy gap between the highest occupied valence state and the lowest unoccupied conduction state in the minority spin channel, and the half-metallic gap (spin gap), which is defined as the energy gap between the highest occupied valence state and the Fermi state in the minority spin channel. The schematic band gap (E_g) and spin (half-metal) gap (E_s) of half-metals are illustrated in Fig. 2.5.7.

In full-Heusler alloys, the X atoms form a simple cubic lattice and both Y and Z atoms occupy the body centered sites and have 8 X atoms as nearest neighbors. The distance between the X atoms is a second neighbor distance. Although, the covalent

hybridization between these atoms is qualitatively very important. The $5d$ states are divided into two degenerate states: first, twofold degenerate $e_g(d_{r^2}, d_{x^2-y^2})$, second , the threefold degenerate $t_{2g}(d_{xy}, d_{yx}, d_{zx})$ states. In a first step, the covalent hybridization occur between the two X atoms where the bonding hybrids (denoted by e_g or t_{2g}) and the antibonding orbitals (denoted by e_u or t_{1u}) are formed by the e_g and t_{2g} states coupling between two X atoms. In a second step, the hybridization between X-X hybridize orbitals and with the Y d orbitals. All 5 X-Y bonding bands are occupied and all 5 X-Y antibonding bands are empty, and E_F falls in between the 5 nonbonding ($2\times e_u$ and $3\times t_{1u}$) X bands, where the $3\times t_{1u}$ are occupied and the $2\times e_u$ bands are empty. The Fig. 2.5.8 illustrate the origin of the gap in the minority band in full-Heusler alloys.

The existence of a gap in the minority spin channel containing the Fermi level, implies that the exchange splitting in the half metallic ferromagnets is such that the application of an external field in the direction of the spin polarization does not produce any increment in the magnetization, *i.e.*, we have a vanishing spin susceptibility.

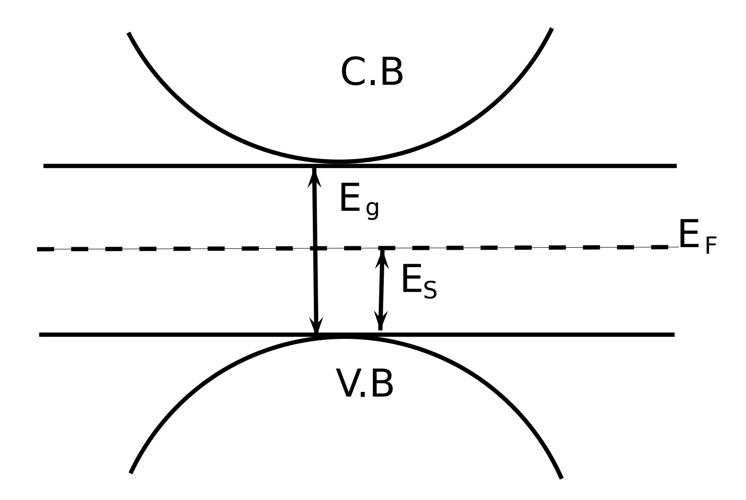


Figure 2.5.7. The schematic band gap (E_g) and spin-gap (E_s) of half-metals.

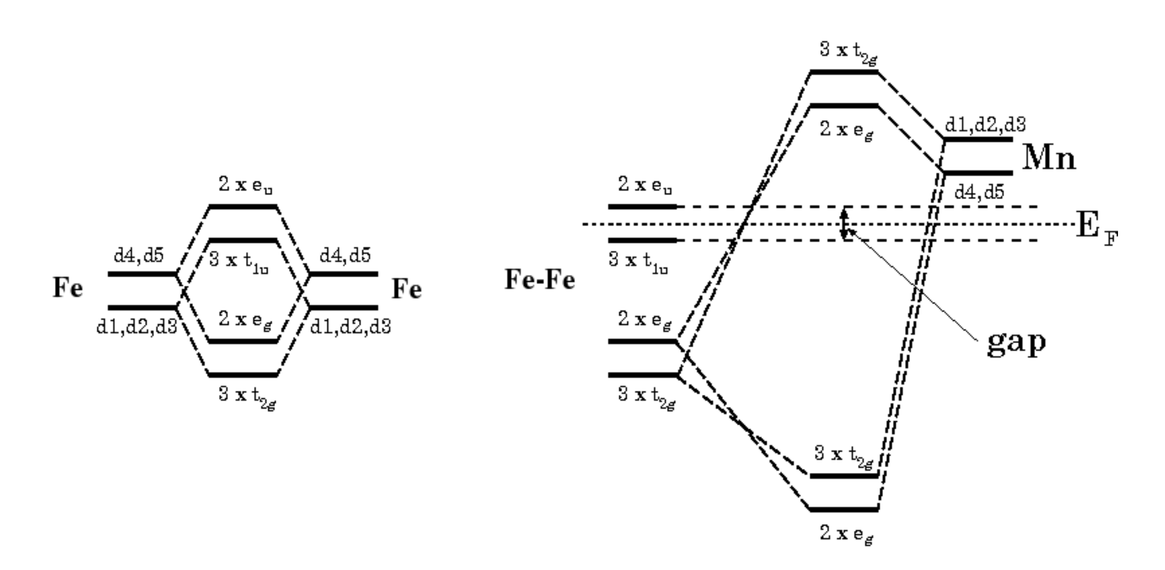


Figure 2.5.8. Schematic illustration of the origin of the gap in the minority band in full-Heusler alloys.

CHAPTER 3

THEORETICAL FORMALISM

3.1 Introduction

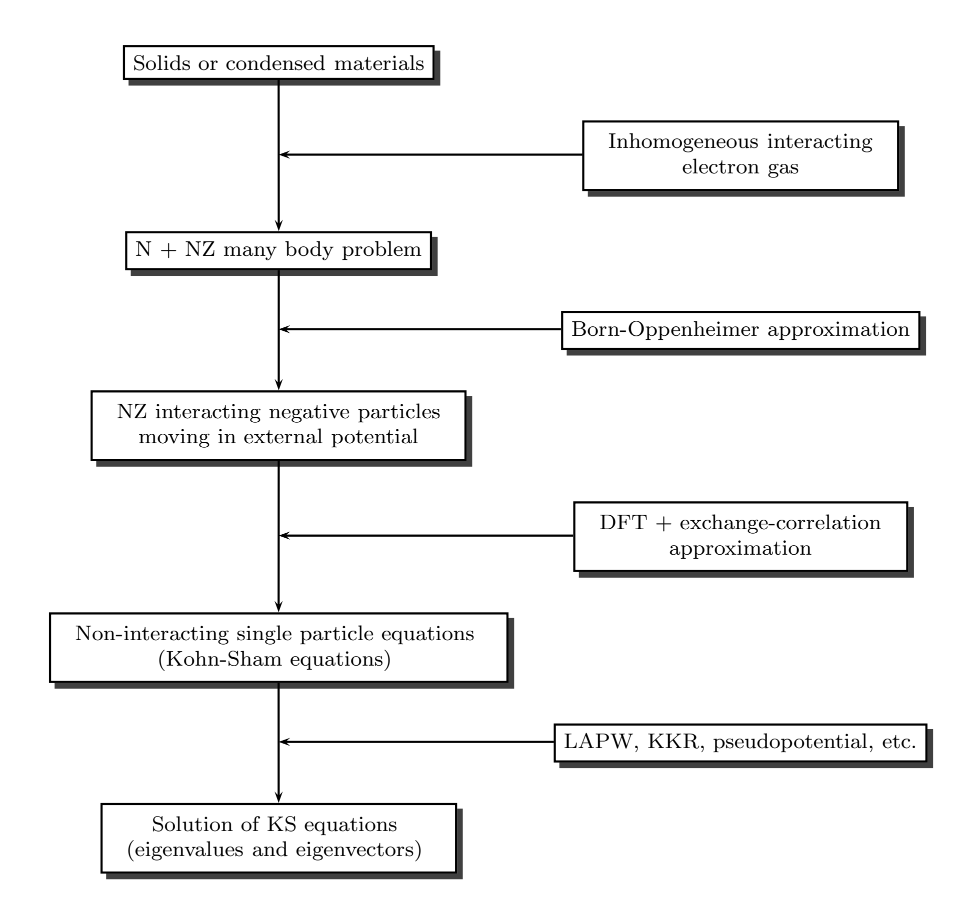


Figure 3.1.1. The progress stages for solving the many-body problems flowchart.

A crystalline material is an arrangement of atoms in a lattice. The atoms in the material can be separated into two parts: the negative light particles (electrons) and the positive heavy particles (nuclei). If there are N nuclei, then we are dealing with a

N+ZN quantum many-body problems. The simplest model system representing and illustrating key properties of interacting electrons and characteristic magnitudes of electronic energies in condensed matter is the homogeneous electron gas, in which the nuclei are replaced by a uniform positively charged background. The progress stages for solving the many-body problems are summarized in the flowchart in Fig. 3.1.1.

3.2 Basic Equations for the Interacting Electrons and Nuclei in Solids

The non-relativistic Hamiltonian for the system of electrons and nuclei,

$$\begin{aligned}\hat{\mathbf{H}} &= -\frac{\hbar^2}{2m_e}\sum_i \nabla_i^2 + \sum_{i,I}\frac{Z_I e^2}{|\mathbf{r}_i - \mathbf{R}_I|} + \frac{1}{2}\sum_{i\neq j}\frac{e^2}{|\mathbf{r}_i - \mathbf{r}_j|} \\ &\quad -\sum_I \frac{\hbar^2}{2M_I}\nabla_I^2 + \frac{1}{2}\sum_{I\neq J}\frac{Z_I Z_J e^2}{|\mathbf{R}_I - \mathbf{R}_J|},\end{aligned} \tag{3.1}$$

where M_I, Z_I and Z_J are the nucleus mass and nucleus charge of I^{th} and J^{th} nucleus respectively, $\mathbf{R}_I$ and $\mathbf{R}_J$ are the position of I^{th} and J^{th} nucleus respectively, $\mathbf{r}_i$ and $\mathbf{r}_j$ are the i^{th} and j^{th} electron position respectively. Here the first term is the kinetic energy contributions from the electrons, the second term is the electron-nucleus attraction, and the rest are from electron-electron repulsive, nuclei kinetic energy and nucleus-nucleus repulsive, respectively. Here relativistic effects, spin-orbit coupling, magnetic fields, and quantum electrodynamics are not included. To solve equations of this Hamiltonian the following two assumptions must be take firstly,

1. The adiabatic approximation (or Born-Oppenhemer approximation)

   The nuclei are too massive to follow the rapidly changing spatial distribution of the electrons, therefore we consider two Schrödinger equations, one for the electrons and the other for the nuclei. By using Born-Oppenheimer approximation, which assume that the electrons move faster than the nuclei because they much less massive, so the nuclei are treated as frozen particles and all their quantum effects are neglected. If the mass of nuclei set to infinity, then the kinetic energy of the nuclei can be ignored. The origin problem convert to ZN quantum many-body problems for negative (electrons) particles moving in the external potential of the nuclei.

2. The effective field approximation

   It is possible to consider separately the motions of individual electrons. Each of them is considered as moving in the effective field of the (stationary) nuclei and all the other electrons. Screening is the effect in many-body

system whereby the particles collectively correlate to reduce the net interaction among any two particles. Such as Thomas-Fermi screening and Debye screening in a classical system.

A homogeneous system is completely specified by its density $n = \mathrm{N}_e/\Omega$, where N_e is number of electrons and Ω is the volume, which can be characterized by the parameter r_s, defined as the radius of a sphere containing one electron on average, r_s is a measure of the average distance between electrons. Of course, density is not constant in a real solid and it is interesting to determine the variation in density. In order to understand the interacting gas as a function of density, it is useful to express the Hamiltonian in terms of scaled coordinates $\tilde{\mathbf{r}} = \mathbf{r}/\mathrm{r}_s$ instead of atomic units. The Hamiltonian for the homogeneous system is derived by replacing the nuclei interaction in Eqn. 3.1 with a uniform positively charged background, which leads to

$$\hat{\mathbf{H}} = (\frac{a_0}{r_s})^2 \sum_i [-\frac{1}{2}\tilde{\nabla}_i^2 + \frac{1}{2}\frac{r_s}{a_0}(\sum_{j\neq i}\frac{1}{|\tilde{\mathbf{r}}_i - \tilde{\mathbf{r}}_j|} - \frac{3}{4\pi}\int d^3\tilde{\mathbf{r}}\frac{1}{|\tilde{\mathbf{r}}|})], \tag{3.2}$$

3.3 The Fundamentals of Standard Density Functional Theory (DFT)

The well-established scheme to calculate electronic properties of condensed materials is based on the DFT, for which Walter Kohn has received the Nobel Prize in chemistry in 1998. DFT is a universal approach to solve the quantum mechanical many-body problems, where the system of interacting electrons is mapped in a unique manner onto an effective non-interacting system that has the same total density [Hohenberg and Kohn 1964]. The attraction of density functional theory is evident by the fact that one equation for the density is remarkably simpler than the full many-body Schrödinger equation that involves 3N degrees of freedom for N electrons. According to the variational principle a set of effective one-particle Schrödinger equations, the so-called Kohn-Sham equations [Kohn and Sham 1965], must be solved. The non-relativistic Hamiltonian of the many-electron system under the influence of an external potential $v(\mathbf{r})$ and the mutual Coulomb repulsion is written as:

$$\hat{H} = \hat{T} + \hat{U} + \hat{V}_{ext} \tag{3.3}$$

where $\hat{T}$ is the kinetic energy operator, $\hat{U}$ is the electron-electron interaction and $\hat{V}_{ext}$ is the external potential which could be written in second quantization form as

$$\hat{T} = \frac{1}{2}\int \nabla\psi^*(\mathbf{r}).\nabla\psi(\mathbf{r})d\mathbf{r},$$

$$\hat{U} = \frac{1}{2}\int \frac{1}{|\mathbf{r}-\mathbf{r}'|}\psi^*(\mathbf{r})\psi^*(\mathbf{r}')\psi(\mathbf{r}')\psi(\mathbf{r})d\mathbf{r}',$$

and

$$\hat{V}_{ext} = \int v(\mathbf{r})\psi^*(\mathbf{r})\psi(\mathbf{r})d\mathbf{r}$$

The charge density of particles ρ is given by expectation value of the density operator $\hat{\rho}(\mathbf{r}) = \sum_{i=1} \delta(\mathbf{r} - \mathbf{r}_i)$,

$$\rho(\mathbf{r}) = \frac{\langle\Psi|\hat{\rho}(\mathbf{r})|\Psi\rangle}{\langle\Psi|\Psi\rangle},$$

It plays a central role in electronic structure theory. For simplicity the nondegenerate ground state situations will be dealing.

Thomas-Fermi and X_α Methods

The electronic density $\rho(\mathbf{r})$ plays a central role and in which the system of electrons is pictured more like a classical liquid. Crude descriptions of inhomogeneous systems like atoms and impurities in metals. Thomas-Fermi model [Thomas 1926, Fermi 1926] is a statistical model assuming that the number of electrons is large in the system and could be regarded as a completely degenerate Fermi gas of nonuniform density $\rho(\mathbf{r})$. The total energy of such system in an external field is

$$E_{TF}[\rho] = \frac{3}{10}(3\pi^2)^{\frac{2}{3}} \int \rho^{\frac{5}{3}}(\mathbf{r})d\mathbf{r} + \int V_{ext}(\mathbf{r})\rho(\mathbf{r})d\mathbf{r} + \frac{1}{2}\int\int \frac{\rho(\mathbf{r}_1)\rho(\mathbf{r}_2)}{|\mathbf{r}_1 - \mathbf{r}_2|}d\mathbf{r}_1 d\mathbf{r}_2. \quad (3.4)$$

Here, V_{ext} is the external potential generated by the nuclei,

$$V_{ext}(\mathbf{r}) = \sum_{k=1}^{M} \frac{-Z_k}{|\mathbf{R}_k - \mathbf{r}|}. \quad (3.5)$$

The Thomas-Fermi approach starts with approximations that are too crude, missing essential physics and chemistry, such as shell structures of atoms and binding of molecules. Thus, it falls short of the goal of a useful description of electrons in matter.

Slater [Slater 1951] proposed to approximate the exchange potential V_x by the one of a non-interacting electron gas replacing the corresponding charge density $\rho_0(\mathbf{r})$ by the local charge density density $\rho(\mathbf{r})$ in the solid:

$$V_x(\mathbf{r}) = -6\alpha(\frac{3\rho(\mathbf{r})}{8\pi})^{\frac{1}{3}}, \quad (3.6)$$

where α is an arbitrary dimensionless parameter. The case of α=1 corresponds to a homogeneous electron gas. This approach is called the X_α method to solve the Hartree-Fock [Hartree 1928, Fock 1930] equations. Both Thomas-Fermi theory and X_α Method are constructed as an approximation to solve the Schrödinger equation or Hartree-Fock equation and not as an exact theory.

3.3.1 The Hohenberg-Kohn Theorems

The two Hohenberg and Kohn theorems [Hohenberg and Kohn 1964] are used to formulate the density functional theory as an exact theory of many-body systems. The relations established by Hohenberg and Kohn are illustrated in Fig. 3.3.2 and the first theorem is

Theorem 1 *" It states that once you know the ground state electron density in position space any ground state property is uniquely defined."*

The ground state electron density ρ_0 (in atoms, molecules or solids) uniquely defines the total energy E or any ground state property; i.e., must be a functional of the density in the position space. Thus one does not need to know the many-body wave function. The noninteracting particles of this auxiliary system move in an effective local one-particle potential, which consists of a classical mean-field (Hartree) part and an exchange-correlation part V_{xc} (due to quantum mechanics) that, in principle, incorporates all correlation effects exactly. This theorem is just an existence theorem. The second Hohenberg-Kohn theorem is

Theorem 2 *"It states that once the functional that relates the electron density in position space with the total electronic energy is known, one may calculate it approximately by inserting approximate densities ρ'. Furthermore, just as for the variational method for wave functions, one may improve any actual calculation by minimizing $E_e[\rho']$."*

The total energy functional is

$$\begin{aligned} E_{HK}[\rho] &= T[\rho] + E_{int}[\rho] + \int d\mathbf{r} V_{ext}(\mathbf{r})\rho(\mathbf{r}) + E_{II} \\ &\equiv F_{HK}[\rho] + \int d\mathbf{r} V_{ext}(\mathbf{r})\rho(\mathbf{r}) + E_{II} \end{aligned} \tag{3.7}$$

where T[ρ] is the kinetic energy of interacting system, E_{II} is the interaction energy of the nuclei. The functional F_{HK} is universal including kinetic and potential of the interacting electron system.

$$F_{HK}[\rho] = T[\rho] + E_{int}[\rho], \tag{3.8}$$

The major part of the complexities of the many electron problems are associated with the determination of the universal functional $F_{HK}[\rho]$. The universal functional $F_{HK}[\rho(\mathbf{r})]$, which applies to all electronic systems in their ground state no matter what the external potential is. An expression for $F_{HK}[\rho(\mathbf{r})]$ has been obtained to describe correctly the long range Friedel charge oscillations set up by a localized perturbation, when ρ deviates only slightly from uniformity, *i.e.*, $\rho(\mathbf{r})=\rho_0 + \tilde{\rho}(\mathbf{r})$, with $\tilde{\rho}/\rho_0 \rightarrow 0$. The case of a slowly varying, but not necessarily almost constant density, $\rho(\mathbf{r}) = \varphi(\mathbf{r}/\ r_s)$, $r_s \rightarrow 0$. Then the functional E[ρ] alone is sufficient

to determine the exact ground state energy and density. As a consequence, the theorems of Hohenberg and Kohn show only that it is possible to calculate any ground-state property, but not how. Furthermore, Mermin [Mermin 1965] shown that the theorems of Hohenberg and Kohn for the ground state carry over to the equilibrium thermal distribution by constructing the density corresponding to the thermal ensemble. However, the proof proceeds by *reductio ad absurdum*. Figure 3.3.2 shows the schematic representation of Hohenberg and Kohn theorem.

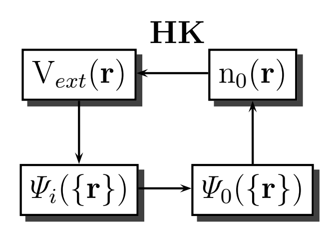


Figure 3.3.2. Schematic representation of Hohenberg and Kohn theorem.

3.3.2 The Kohn-Sham Ansatz

The Hohenberg-Kohn theorems provide a formalistic proof for the correctness of the approach of Thomas-Fermi, but do not provide any practical scheme for calculating ground-state properties from the electron density. The Kohn-Sham approach is to replace the difficult interacting many-body system obeying the Hamiltonian Eq. 3.1 with a different auxiliary system that can be solve more easily.

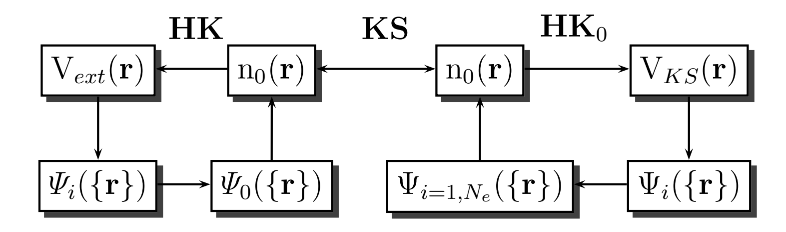


Figure 3.3.3. Schematic representation of Kohn-Sham *ansatz*.

Figure 3.3.3 shows the schematic representation of the Kohn-Sham *ansatz* which is based on two assumptions:

1. Non-interacting V representations

The ground state density of the real interacting system is equal to that of an auxiliary non-interacting system. There are no rigorous proofs for real systems of interest.

2. The auxiliary Hamiltonian is chosen to have the kinetic operator and an effective potential, $\mathrm{V}_{eff}^{\sigma}(\mathbf{r})$.

Kohn-Sham Trick

The trick of Kohn and Sham is now as follows. They considered a fictitious system of non-interacting particles. They assumed that this system has the same density and energy as in the real system. To ensure that they have the same density and energy as in the real system, these particles are assumed to move with kinetic energy T_0 in some external potential $\mathrm{V}_{eff}(\vec{r})$. However, since the particles are non-interacting, their total energy expression is considerably simpler,

$$E_e = T_0[\rho(\mathbf{r})] + \int V_{eff}(\mathbf{r})\rho(\mathbf{r})d\mathbf{r}$$

3.3.3 Spin-Polarized Kohn-Sham Equations

Spin density functional theory is essential in the theory of atoms and molecules with net spins, as well as solids with magnetic order. To deal with magnetic materials, the single-particle Kohn-Sham equation is extended to include spin (denoted by σ) and can be written as:

$$(H_{KS}^{\sigma} - \epsilon_i^{\sigma})\psi_i^{\sigma}(\mathbf{r}) = 0, \tag{3.9}$$

where ϵ_i^{σ} is the spin-polarized eigenvalue, $\psi_i^{\sigma}(\mathbf{r})$ is the spin-polarized non-interacting eigenvectors and H_{KS}^{σ} is the spin-polarized Kohn-Sham Hamiltonian, which is given by

$$H_{KS}^{\sigma}(\mathbf{r}) = -\frac{1}{2}\nabla^2 + V_{KS}^{\sigma}(\mathbf{r}), \tag{3.10}$$

the spin-polarized Kohn-Sham potential V_{KS}^{σ} could be written by two terms

$$\phi^{\sigma}(\mathbf{r}) = V_{ext}^{\sigma}(\mathbf{r}) + \int \frac{\rho^{\sigma}(\mathbf{r}')}{|\mathbf{r}-\mathbf{r}'|}d\mathbf{r}', \tag{3.11}$$

and

$$\mu_{xc}^{\sigma}(\rho) = \frac{\delta E_{xc}[\rho]}{\delta\rho(\mathbf{r},\sigma)} = \delta(\rho^{\sigma}\epsilon_{xc}(\rho^{\sigma}))/\delta\rho^{\sigma}, \tag{3.12}$$

where μ^{σ} is the spin-polarized exchange-correlation contribution to the chemical potential of a uniform gas of density ρ. Where ρ given by

$$\rho(\mathbf{r}) = \sum_{\sigma}\rho(\mathbf{r},\sigma) = \sum_{\sigma}\sum_{i=1}^{N}|\psi_i^{\sigma}(\mathbf{r})|^2, \tag{3.13}$$

where the summation over σ refers to the two spin channels.

3.3.4 Exchange-Correlation Functionals

After Kohn-Sham approach, the exchange correlation energy may be defined as the difference between the energy of the real interacting many-body system and the auxiliary independent-particle system with electron-electron interactions replaced by the Hartree.

$$\begin{aligned} E_{xc}[\rho] &= F_{HK}[\rho] - (T_s[\rho] + E_{Hartree}[\rho]) \\ &= \langle \hat{T} \rangle - T_s[\rho] + \langle \hat{V}_{int} \rangle - E_{Hartree}[\rho], \end{aligned} \tag{3.14}$$

where T is the kinetic energy of the interacting system, T_s is the kinetic energy of the noninteracting system and V_{int} is the interacting potential. The genius of the Kohn-Sham approach is that by explicitly separating out the independent-particle kinetic energy and the long-range Hartree terms, the remaining exchange-correlation functional $E_{xc}[\rho]$ can reasonably be approximated as a local or nearly local functional of the density. Another less important fold is the ansatz leads to tractable independent-particle equations. The full exchange-correlation energy including kinetic terms can be found in two ways: kinetic energy can be determined from the virial theorem [Gori-Giorgi *et al.* 2000] or from the coupling constant integration formula [Martin 2004]. The exact functional form of the potential V_{xc} is not known and thus one needs to make approximations. Early applications were done by using results from quantum Monte Carlo calculations for the homogeneous electron gas, for which the problem of exchange and correlation can be solved exactly, leading to the original LDA. Local density approximation works reasonably well but has some shortcomings mostly due to the tendency of overbinding, which cause e.g., too small lattice parameters.

Local Spin Density Approximation (LSDA)

For polarized homogeneous system the local spin density approximation (LSDA) are used instead of LDA, where

$$\begin{aligned} E_{xc}^{LSDA}[\rho^{\uparrow}, \rho^{\downarrow}] &= \int d\mathbf{r}\rho(\mathbf{r})\epsilon_{xc}^{hom}(\rho^{\uparrow}(\mathbf{r}), \rho^{\downarrow}(\mathbf{r})) \\ &= \int d\mathbf{r}\rho(\mathbf{r})[\epsilon_{x}^{hom}(\rho^{\uparrow}(\mathbf{r}), \rho^{\downarrow}(\mathbf{r})) + \epsilon_{c}^{hom}(\rho^{\uparrow}(\mathbf{r}), \rho^{\downarrow}(\mathbf{r}))] \end{aligned} \tag{3.15}$$

where the $\rho^{\uparrow}$ and $\rho^{\downarrow}$ refer to spin up (majority spin) and spin down (minority spin), respectively. Here the axis of quantization of the spin assumed to be the same at all points in space. The fractional spin polarization defined as

$$\zeta(\mathbf{r}) = \frac{\rho^{\uparrow}(\mathbf{r}) - \rho^{\downarrow}(\mathbf{r})}{\rho(\mathbf{r})} \tag{3.16}$$

There are many parametrization forms of E_{xc}^{LSDA} such as von Barth and Hedin parametrization (for more details see ref. [von Barth and Hedin 1972]).

Generalized Gradient Approximation (GGA)

We briefly describe some of the physical ideas that are the foundation for construction of GGAs.

1. The gradient of the density $|\nabla n^{\sigma}|$ "Gradient expansion approximation" (GEA) carried out by Herman *et al.* [Herman *et al.* 1969].

2. The lower-order expansion of the exchange and correlation energies is known. The GEA does not lead to consistent improvement over the LSDA.

The generalized form of the exchange-correlation energy is written as:

$$E_{xc}^{GGA}[\rho^{\uparrow},\rho^{\downarrow}] = \int d\mathbf{r}\rho(\mathbf{r})\epsilon_{xc}(\rho^{\uparrow}(\mathbf{r}),\rho^{\downarrow}(\mathbf{r}),|\nabla\rho^{\uparrow}|,|\nabla\rho^{\downarrow}|,....)$$
$$= \int d\mathbf{r}\rho(\mathbf{r})\epsilon_{x}^{hom}F_{xc}(\rho^{\uparrow}(\mathbf{r}),\rho^{\downarrow}(\mathbf{r}),|\nabla\rho^{\uparrow}|,|\nabla\rho^{\downarrow}|,....), \quad (3.17)$$

where F_{xc} is dimensionless and $\epsilon_x^{hom}(x) = \frac{3}{4\pi}(\frac{9\pi}{4})^{\frac{1}{3}}/r_s$ is the exchange energy of the unpolarized homogeneous gas.

To facilitate practical calculations, F_{xc} must be parametrized analytic functions. A first-principles numerical GGA can be constructed by starting from the second-order density-gradient expansion for the exchange-correlation hole surrounding the electron in the system of slowly varying density, then cutting off its spurious long-range parts to satisfy sum rules on the exact hole. The semilocal form of Eq. 3.17 is too restrictive to reproduce all the known behaviors of the exact functional. The Perdew, Burke and Ernzerhof (PBE96) [Perdew *et al.* 1996] parametrization of GGA exchange-correlation energy begin by divided the exchange-correlation energy into the correlation part E_c^{GGA} and the exchange part E_x^{GGA}. In the case of uniform scaling to the high-density limit [n($\mathbf{r}$) $\rightarrow \lambda^3 n(\lambda\mathbf{r})$ and $\lambda \rightarrow \infty$, whence $r_s \rightarrow 0$ as λ^{-1}] the correlation energy is written as

$$E_c^{GGA} = -\frac{e^2}{a_0}\int d\mathbf{r}\rho\gamma\phi^3 \times \ln\left[1 + \frac{1}{\chi s^2/\phi^2 + (\chi s^2/\phi^2)^2}\right], \quad (3.18)$$

where s = $|\nabla\rho|/2k_F\rho = (r_s/a_0)^{\frac{1}{2}}\phi t/c$ is another dimensionless density gradient as t, γ=0.031 091, c = $(3\pi^2/16)^{\frac{1}{3}} \approx 1.2277$, ϕ is a spin-scaling factor, and $\chi = (\beta/\gamma)c^2 exp(-\omega/\gamma) \approx 0.72161$. And the exchange energy is written as

$$E_x^{GGA} = \int d\mathbf{r}\rho(\mathbf{r})\epsilon_x^{unif}(\rho)F_x(s), \quad (3.19)$$

where $\epsilon_x^{unif} = -3e^2k_F/4\pi$ and the simple F_x(s) is

$$F_x(s) = 1 + \kappa - \kappa/(1 + \mu s^2/\kappa),$$

where $\kappa = 0.804$ and $\mu = \beta(\pi^2/3) \simeq 0.21951$, the effective gradient coefficients for exchange. The interest values in real system are $0 \lesssim s \lesssim 3$ and $0 \lesssim r_s/a_0 \lesssim 10$.

For most physical r_s, GGA favors density inhomogeneity more than LSDA. One very important result is that for materials at typical solid densities ($r_s \approx 2$ - 6) the correlation energy is much smaller than the exchange energy; however, at very low densities (large r_s) correlation becomes more important and dominates in the regime of the Wigner crystal ($r_s > \approx 80$). This perspective illustrates the importance in DFT calculations of improving the functional, since this defines the quality of the calculation.

3.3.5 Strategies for Solving the Kohn-Sham Equations

There are three basic approaches to solve Kohn-Sham equation and the calculation of independent-particle electronic states in materials: First, Plane wave and grid methods (pseudopotential, projector augmented wave (PAW), orthogonalized plane wave (OPW)); Second, localized atomic (-like) orbitals as linear combination of atomic orbitals (LCAO) and the semiempirical tight-binding method; Third, Atomic sphere methods as Korringa-Kohn-Rostoker (KKR), augmented plane wave (APW), linear muffin-tin-orbital (LMTO) and linear augmented plane wave (LAPW). Many computer programs that can solve the DFT equations are available but they differ in the basis sets. Basis sets used in different electronic structure calculations are

- Slater-type Orbitals
- Gaussian-type Orbitals
- Plane wave
- Numerical Basis Functions
- Augmented Wave it may be
    1. APW method = plane waves + numerical basis functions.
    2. Augmented spherical wave(ASW) or LMTO methods = spherical waves + numerical basis functions.

The latest schemes to solve the KS equations are the use of the modern pseudo-potentials or the full-potential methods. There are also simplified versions of electronic structure calculations such as LMTO or ASW methods, in which often the atomic sphere approximation (ASA) is made, where within the self-consistency cycle a spherically averaged potential and charge density is assumed around each atomic site.

Different methods have their advantages or disadvantages when it comes to computing various quantities. For example, properties, which rely on the knowledge of the density close to the nucleus (hyperfine fields, electric field gradients, etc.), require an all-electron description rather than a pseudo-potential approach with unphysical wave functions near the nucleus. On the other hand for an efficient

optimization of a structure, in which the shape (and symmetry) of the unit cell changes, it is very helpful to know the corresponding stress tensor. These tensors are much easier to obtain in pseudo-potential schemes and thus are available there. In augmentation schemes, however, such algorithms become more tedious and consequently are often not implemented. On the other hand all-electron methods do not depend on choices of pseudo-potentials and contain the full wave function information. Thus, the choice of method for a particular application depends on the properties of interest and may affect the accuracy, ease or difficulty to calculate them.

In solid crystalline materials the periodicity of the potential and density with help of Bloch theory, also the symmetry make the many-body problem more easy and solvable. If the wave functions or densities of the core electrons are treated as being identical to their isolated-atom quantities this is known as a frozen-core approximation.

It is very common to separate the determination of the $c_{i\alpha}$ and the determination of the self- consistent charge density in density functional calculations. It is necessary to repeatedly determine the $c_{i\alpha}$ that solve the single particle equations for fixed charge density using standard matrix techniques. The Kohn-Sham Hamiltonian and overlap matrices, **H** and **S** are constructed and the matrix eigenvalue equation,

$$(\mathbf{H} - \epsilon_i \mathbf{S}) c_i = 0, \tag{3.20}$$

is solved at each **k**-point in the irreducible wedge of the Brillouin zone using standard linear algebra routines.

The wave functions expanded in plane-waves can be transformed efficiently from reciprocal space (coefficients of plane-wave expansion) to real space (values on a real space grid) using fast Fourier transforms (FFTs) means that many operators can be made diagonal. The main reason d'etre of non-plane-wave basis sets is to reduce the size of the secular equation for materials.

3.3.6 Self-Consistency in Density Functional Calculations

The historically dominant approach has been to refine the density iteratively by solving Eqs. (3.9) and (3.11) to (3.13) self-consistently. It is begins with assuming guess ρ, constructs ϕ from Eq. (3.11) and μ_{xc} from Eq. (3.12), and finds a new ρ from Eqs. (3.9) and (3.13). This is the basis of the standard self-consistency cycle illustrate in Fig. 3.3.4. Where the simplest mixing scheme is straight mixing (broyden scheme) given by:

$$\rho_{in}^{i+1} = (1 - \alpha)\rho_{in}^{i} + \alpha \rho_{out}^{i}, \tag{3.21}$$

where the superscript refers to the iteration number and α is the mixing parameter. Here, there are two questions should be answered: first, how the difference DFT codes calculate (estimate) the guess electron density (ρ_{in}) to start the self-consistence calculation? There are many possibilities for a first guess.

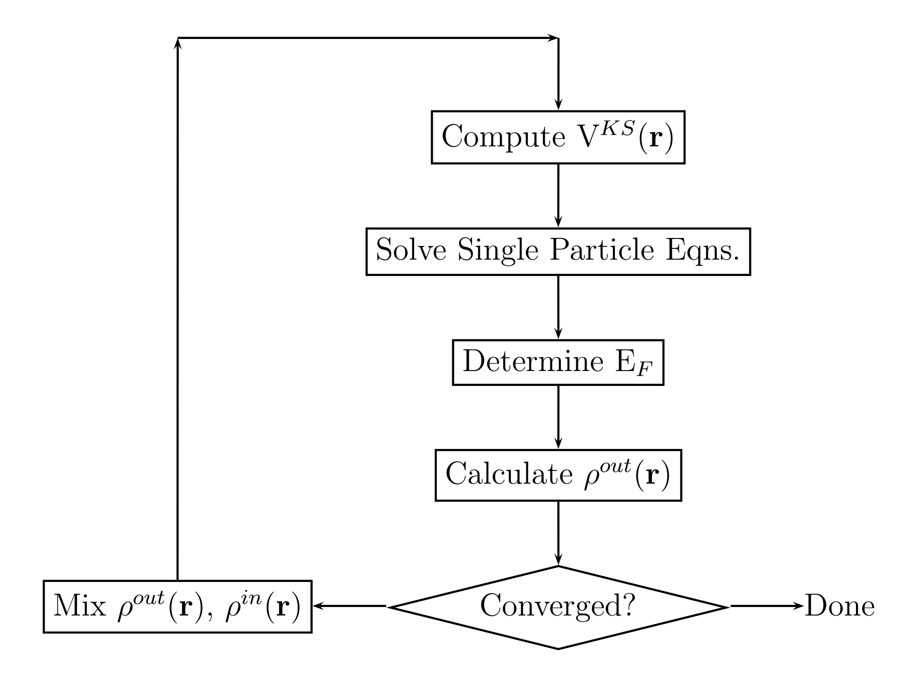


Figure 3.3.4. Schematic flow-chart for self consistent functional calculations.

Most codes start with a superposition of atomic densities. But it is even possible to start with a random density. Second, as we know the most simplest do by DFT are using the electron density instead of the wave function but all DFT codes calculate the KS wave function and then calculate the density? The KS wave functions are not the real (many body) wave function of your system. The real wave function is a very complicated object $\Psi(\mathrm{x}_1,\mathrm{x}_2,...,\mathrm{x}_N)$ which depends on all N coordinates x_i of the N electrons. It has to obey precise rules as to symmetry and interchange of two electrons, etc. DFT allows you not to consider this complicated many-body wave functions. In principle, in DFT we only need the density instead. But unfortunately, nobody managed to write a good approximation of the kinetic energy in terms of the density alone. This is why Kohn and Sham have introduced the KS orbitals. They are single particle wave functions $\phi_i(x)$ which are much less complicated than the many-body wave functions $\Psi(x_1,...,x_N)$. They depend only on a single position, like the density. Using the KS wave functions, we may write the kinetic energy as

$$-\frac{1}{2m_e}\sum_i \int dx \phi_i^*(x) d^2/dx^2 \phi_i(x),$$

As a result, working with single particle orbitals are much easier than many-body orbitals [Gebauer 2010].

3.4 Full Potential Linearized Augmented Plane Wave (FP-LAPW) Implementation

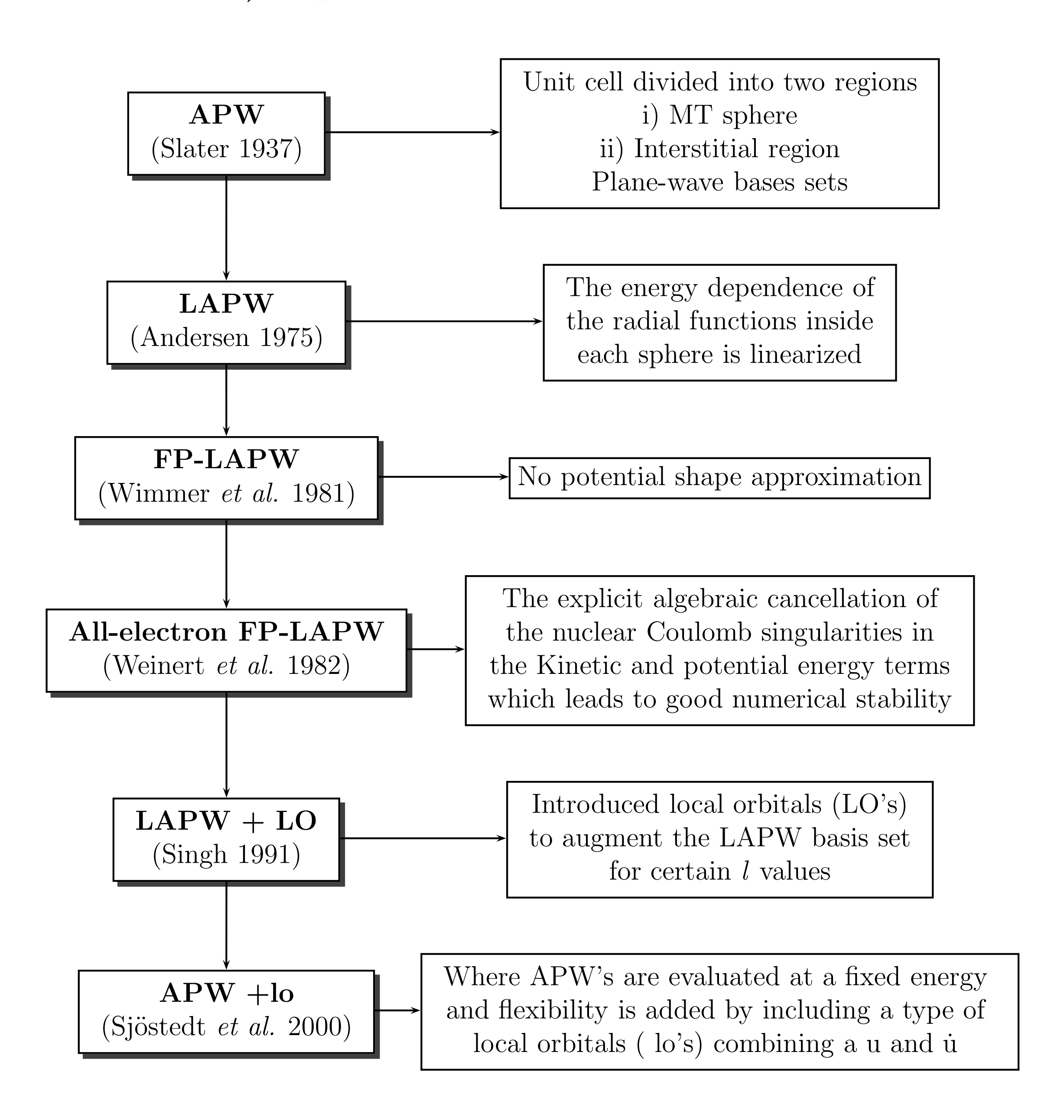


Figure 3.4.5. The historical progress of the FP-LAPW method flow chart.

We summarize the historical progress of the FP-LAPW method [Wimmer *et al.* 1981] in the flowchart Fig. 3.4.5. Which is one among

the most precise schemes for solving the Kohn-Sham equations. There are several programs employing this method such as FLAPW (Freeman's group), FLEUR (Blügel's group), D. Singh's code and others. Here we focus on the WIEN code [Blaha *et al.* 1990] that was developed during the last two decades and is used worldwide by more than 500 groups coming from universities and industrial laboratories.

The muffin tin approximation (MTA) has been frequently used since 1970s and works reasonably well in highly coordinated (closed packed) systems. However, for covalently bonded solids, open or layered structures, MTA is a poor approximation and leads to serious discrepancies with experiment. In all these cases a full-potential treatment is essential. In the full-potential schemes both, the potential and charge density, are expanded into lattice harmonics inside each atomic sphere and as a Fourier series in the interstitial region. As illustrated in Fig. 3.4.6 in the next section.

The foundation of full-potential calculation was laid by the pioneering work of the Freeman group leading to the FP-LAPW [Wimmer *et al.* 1981]. The full-potential (LAPW) method enhanced the potential in LAPW by expand it in interstitial region ($\mathbf{I}$) and muffin-tin sphere ($\mathbf{S}_{MT}$) as

$$V_{eff}(\mathbf{r}) = \begin{cases} \sum_{K}^{|K|\leqslant K^{pot}} V_{eff}(\mathbf{K})e^{i\mathbf{K}.\mathbf{r}} & \mathbf{r} \in \mathbf{I} \\ \sum_{lm}^{l_{max}} V_{eff}^{lm}(\mathbf{r}_\alpha)Y_{lm}(\mathbf{r}_\alpha) & \mathbf{r} \in \mathbf{S_{MT}} \end{cases} \tag{3.22}$$

where $\mathbf{K}^{pot}$ and l_{max} determine the highest reciprocal lattice vectors included in the sum. In order to have the smallest number of LM values in the lattice harmonics expansion (Eq. (3.22)) a local coordinate system for each atomic sphere is defined according to the point group symmetry of the corresponding atom. A rotation matrix relates the local to the global coordinate system of the unit cell. In addition to reducing the number of LM terms in Eq. (3.22) the local coordinate system also provides orbitals that are properly oriented with respect to the ligands, which may help the interpretation. The choice of sphere radii is not very critical in full potential calculations in contrast to MTA, in which one would, *e.g.*, obtain different radii as optimum choice depending on whether one looks at the potential (maximum between two adjacent atoms) or the charge density (minimum between two adjacent atoms). Therefore in MTA one must make a compromise between these two criteria which are both reasonable. In full potential calculations one can efficiently handle this problem and is rather insensitive to the choice of atomic sphere radii.

3.4.1 The Augmented Planewave (APW) Method

The main assumption of APW [Slater 1937] is to divide the space into two regions with different basis expansions. The basis sets used in APW are plane-waves in the interstitial region and the radial solutions inside non-overlapping atom centered spheres $\mathbf{S_{MT}}$ (see Fig. 3.4.6).

$$\phi(\mathbf{r}) = \begin{cases} \Omega^{-\frac{1}{2}} \sum_{\mathbf{G}} c_{\mathbf{G}} e^{i(\mathbf{G}+\mathbf{K}).\mathbf{r}} & \mathbf{r} \in \mathbf{I} \\ \sum_{lm} A_{lm} u_l(r) & \mathbf{r} \in \mathbf{S_{MT}} \end{cases} \tag{3.23}$$

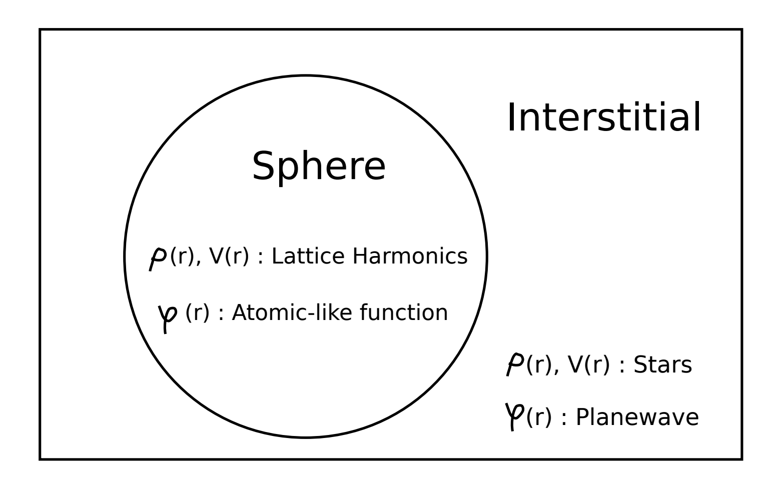


Figure 3.4.6. Partitioning of the unit cell into atomic sphere and an interstitial region. Stars and lattice harmonics are symmetrized plane-waves and spherical harmonics used to represent the charge density and potential

where **G** and **K** are the reciprocal lattice vectors and the wavevector respectively, $c_{\mathbf{G}}$ and A_{lm} are expansion coefficients, $\phi(\mathbf{r})$ is a wave-function, Ω is the cell volume and u_l(r) is the regular solution of radial Schrödinger equation. The APWs are not orthogonal so there would be a non-trivial overlap matrix, **S**. A further difficulty with the APW method is that it is hard (but not impossible) to extend it to use a general crystal potential. Another, less serious, difficulty with the APW method is the so called asymptote problem. To circumvent these difficulties several modifications of the APW method are proposed. Bross and co-workers proposed to choose a multiple radial functions having the same logarithmic derivative. They are matched to the plane-waves, with the requirement that both the value and first derivative of the wave function be continuous [Bross *et al.* 1970].

Four schemes of augmentation (APW, LAPW, LAPW+LO, APW+lo) have been suggested over the years and illustrate the progress in this development of APW-type calculations. The energy dependence of the atomic radial functions can be treated in different ways. In APW it is done by choosing a fixed energy E; which leads to a non-linear eigenvalue problem, since the basis functions become energy dependent. In LAPW, suggested by Andersen[Andersen 1975], a linearization of this energy dependence is used by solving the radial Schrödinger equation for a fixed linearization energy E_c but adding an energy derivative of this function to increase the variational flexibility. Inside sphere the atomic function is given by a sum of partial waves (radial functions times spherical harmonics). In the APW plus local orbitals (APW+lo), method by Sjöstedt *et al.*[Sjöstedt *et al.* 2000] developed, the matching is again (as in APW) only done in value. The crystalline wave functions (of Bloch type) are expanded in these APWs leading (in the latter two cases of LAPW or APW+lo) to a general eigenvalue problem. The size of the matrix is mainly given by the number of plane waves (PWs) but is increased

slightly by the additional local orbitals that are used. As a rule one needs about 50-100 PWs for every atom in the unit cell in order to achieve good convergence. APW+lo leads on the one hand to a significant speed up (by an order of magnitude) and, on the other hand, to a comparable high accuracy with respect to LAPW [Andersen 1975, Koelling and Arbman 1975]. The new version combines the best features of all APW-based methods. It was known that LAPW converges somewhat slower than APW due to the constraint of having differential basis functions and thus it was advantageous to go back to APW. However, the energy-independent basis introduced in LAPW is crucial, since it avoids the non-linear eigenvalue problem of APW, and thus is kept. The local orbitals provide the necessary variational flexibility that make the new scheme efficient[Singh 1991].

3.4.2 The Linearized Augmented Planewave (LAPW) Method

The first LAPW calculations[Andersen 1975, Koelling and Arbman 1975] where within the MT approximation and used a model potential. Follow that, fully self-consistent slab[Jepsen *et al.* 1978, Hamann *et al.* 1981] and bulk[Hamann 1979] codes were developed, and after that full-potential (no MT or other approximation to the charge density or potential) codes began appearing [Hamann 1979, Wimmer *et al.* 1981, Blaha *et al.* 1990]. In LAPW method the basis functions inside the spheres are linear combinations of radial functions, and their derivatives with respect to the linearization parameters, E_l. In the non-relativistic case the LAPW basis functions are,

$$\phi(\mathbf{r}) = \begin{cases} \Omega^{-\frac{1}{2}} \sum_{\mathbf{G}} c_{\mathbf{G}} e^{i(\mathbf{G}+\mathbf{K}).\mathbf{r}} & \mathbf{r} \in \mathbf{I} \\ \sum_{lm} [A_{lm} u_l(r) + B_{lm} \dot{u}_l(r)] & \mathbf{r} \in \mathbf{S_{MT}} \end{cases} \tag{3.24}$$

where the A_{lm} B_{lm} are coefficients for the radial wave functions u_l(r) and the energy derivative radial wave function $\dot{u}_l$(r). The representation of the charge density and potential in the LAPW method as well as the wave functions. A plane-wave expansion could be used in the interstitial and a spherical harmonic expansion inside the sphere. where the charge density is given by

$$\rho(\mathbf{r}) = \begin{cases} \sum_{n,s} \rho_{n,s}^{PW} \cos(k_n z) \Phi_s(\mathbf{r}) & \mathbf{r} \in \mathbf{I} \\ \sum_{\nu} \rho_{\nu}(\mathbf{r}_\alpha) K_{\nu}(\hat{r}_\alpha) - 2 Z_\alpha \delta(\mathbf{r}_\alpha) & \mathbf{r} \in \mathbf{S_{MT}}, \end{cases} \tag{3.25}$$

where $\rho_{n,s}^{PW}$ and $\rho_\nu(\mathbf{r})$ are the density in the interstitial and in the νth sphere respectively, Z_α is the atomic number, $\delta(\mathbf{r}_\alpha)$ is the dalta function and $K_\nu(\hat{r}_\alpha)$ is defined as

$$K_\nu(\hat{r}_\alpha) = \sum_m C_m(\nu) Y_{l_\nu m}(\hat{r}_\alpha), \tag{3.26}$$

is a lattice harmonic (the symmetrized spherical harmonics), $\mathbf{r}_\alpha = \mathbf{r} - \mathbf{R}_\alpha$ is the position of the atomic sphere α and $\Phi_s(\mathbf{r})$ is the two dimensional plane-wave star function

$$\Phi_s(\mathbf{r}) = \frac{1}{n_0} \sum_R exp[i\hat{R}\mathbf{G}_s.(\mathbf{r} - \mathbf{t}_R)], \tag{3.27}$$

where $\mathbf{G}_s$ is a 2D star representative reciprocal-lattice vector, $\hat{R}$ is the point-group part of the 2D space group operation, n_0 is the number of space group operations and $\mathbf{t}_R$ is a nonprimitive 2D translation vector.

In the LAPW method, as it is normally implemented, the cost of computing the Hamiltonian and overlap matrices is smaller than the diagonalization time, but only by a factor of two to five, depend on the details of the system. The crystal momentum $\mathbf{k}$ is defined as a good (conserved) quantum number.

The LAPW method introduces errors of order $(\epsilon - E_l)^2$ in the wave function; this, combined with the variational principle, yields errors of order $(\epsilon - E_l)^4$ in the band energy. There is no asymptote problem in the LAPW method. The LAPW basis has greater flexibility than the APW method inside the spheres, *i.e.* two radial functions instead of one. This mean that there is no difficulty in treating non-spherical potentials inside the spheres; although the optimum value of E_l is not known a priori, this flexibility arising from $\dot{u}_l(r)$ allows an accurate solution. The price to be paid for the additional flexibility of the LAPW basis are the higher plane-wave cutoffs to achieve a given level of convergence. Singh [Singh 1991] adding specially constructed local orbitals (LO) to the basis to permit relaxation of the linearization without an increase in the plane-wave cutoff. The LO's local orbital in LAPW + LO method is,

$$\phi_{LO}(\mathbf{r}) = \begin{cases} 0 & \mathbf{r} \in \mathbf{I} \\ (a_{lm}^{\alpha,LO} u_{1l}(r) + b_{lm}^{\alpha,LO} \dot{u}_{1l}(r) + c_{lm}^{\alpha,LO} u_{2l}(r)) Y_{lm}(\hat{\mathbf{r}}) & \mathbf{r} \in \mathbf{S_{MT}}, \end{cases} \tag{3.28}$$

where u_{1l} and $\dot{u}_{1l}$ are the radial function and its energy derivative at energy E_{1l}, u_{2l} is the radial function at energy E_{2l}. The three coefficients a,b and c are determined by the requirements that the LO's should have zero value and slope at the MT sphere boundary and the normalization.

The method APW+lo [Sjöstedt *et al.* 2000], are shown to be highly effective in reducing the basis set sizes, especially for materials with large interstitial spaces and/or mixtures of atoms that require high plane-wave cutoffs with those requiring lower cutoffs. The lo's local orbital in APW +lo is,

$$\phi_{lo}(\mathbf{r}) = \begin{cases} 0 & \mathbf{r} \in \mathbf{I} \\ (a_{lm}^{\alpha,lo} u_{1l}(r) + b_{lm}^{\alpha,lo} \dot{u}_{1l}(r)) Y_{lm}(\hat{\mathbf{r}}) & \mathbf{r} \in \mathbf{S_{MT}}, \end{cases} \tag{3.29}$$

Here the two coefficients a and b are determined by the normalization and the condition that $\phi_{lo}(R_{MT})$ has zero value.

Role of the Linearization Energies

Learning how to set the linearized energy (E_l) is a frequent source of grief for newcomers to the LAPW method. It would be simply to set E_l near the centers of the bands of interest to be assured of reasonable results, and one could envisage computing the total energy for several reasonable choices of E_l and selecting the set that gave the lowest energy. The augmenting functions, $u_l Y_{lm}$ and $\dot{u}_l Y_{lm}$ are

orthogonal to any core state that is strictly confined within the LAPW sphere. The ghost band state occurs above the true core state eigenvalue, and often in the valence part of the spectrum because the radial functions with E_l are not well suited to representing the semi-core wave function. Using the local orbital extension which permit an accurate treatment of both the core and valence states in a single energy window by adding extra variational freedom for selected angular momentum l. The various E_l should be set independently and must be set near the band energy if the band in question has significant character of the given l.

3.4.3 Synthesis of the LAPW Basis Functions

To synthesis of the LAPW basis functions amounts to determine (1) the radial functions, u_l(r) and $\dot{u}_l$(r) and (2) the coefficients a_{lm} and b_{lm} that satisfy the boundary condition. Other two quantities will be determined are the angular momenta cutoffs, l_{max} for the spherical representation and the plane-wave cutoff, K_{max}. The criterion, $R_\alpha K_{max} = l_{max}$ connect between them. The symmetrized plane-waves or stars, Φ_s (as defined in Eq. (3.27)).

Construction of the Radial Functions

The radial Schrödinger equation (non-relativistic implementation) with the spherically averaged crystal potential $V(r)$, at the linearization energy E_l is

$$[-\frac{d^2}{dr^2} + \frac{l(l+1)}{r^2} + V(r) - E_l]ru_l(r) = 0, \tag{3.30}$$

the solution are the radial functions, u_l(r) and taking the derivative with respect to the linearization energy, one obtains,

$$[-\frac{d^2}{dr^2} + \frac{l(l+1)}{r^2} + V(r) - E_l]r\dot{u}_l(r) = ru_l(r). \tag{3.31}$$

Predictor-corrector methods used to solved these differential equations on the radial mesh. it is convenient to enforce the normalization of u_l(r) and to orthogonalize u_l and $\dot{u}_l$.

Relativistic Radial Functions

Relativistic effects are more important only when the kinetic energy is large. In solids, the band energies of interest are small, this means that the relativistic corrections need to be incorporated in regions where the potential is strongly negative, *i.e.* near the nuclei. In the medium range of atomic numbers (up to about 54) the so-called scalar relativistic schemes [Koelling and Harmon 1977] are often used, which describe the main contraction or expansion of various orbitals (due to the Darwin s-shift or the mass-velocity term) but omit spin orbit splitting. This version is computationally easy and thus is highly recommended for

all systems. The spin orbit part can be included in a second-variational treatment [MacDonald *et al.* 1980]. For very heavy elements it is necessary to add $p_{1/2}$ orbitals [Kuneš *et al.* 2001] or to solve Dirac's equation.

In the LAPW method, the relativistic corrections can be safely neglected in the interstitial region, and the only modifications are to the radial functions in the spheres and the components of the Hamiltonian that operate on them. Furthermore, relativistic effects are important only when the kinetic energy is large. The Dirac equation and its energy derivative used instead of the non-relativistic radial equation and retain the relativistic terms when evaluating the sphere contribution to the Hamiltonian matrix elements. The scalar-relativistic approximation which mean the neglected of spin-orbit effects is used to treat the valence electrons. Where the scalar-relativistic Hamiltonian or Pauli Hamiltonian write as,

$$\hat{H} = \frac{1}{2m}[\mathbf{P} + \frac{e}{c}\mathbf{A}(\mathbf{r},t)]^2 - e\phi(\mathbf{r},t) + \frac{e\hbar}{2mc}\sigma.\mathbf{B}(\mathbf{r},t), \tag{3.32}$$

For fully-relativistic solutions, we need the solution of the Dirac equation inside the MT sphere, which is written as

$$\Phi_{\kappa\mu} = \begin{bmatrix} g_\kappa \chi_{\kappa\mu} \\ -if_\kappa \sigma_r \chi_{\kappa\mu} \end{bmatrix} \tag{3.33}$$

where κ is the relativistic quantum number, $\chi_{\kappa\mu}$ is a two-component spinor and the radial coordinate has been suppressed. Here, the two functions f_κ and g_κ satisfy the following radial equations:

$$f'_\kappa = \frac{1}{c}(V-E)g_\kappa + (\frac{\kappa-1}{r})f_\kappa$$

$$g'_\kappa = -\frac{(\kappa-1)}{r}g_\kappa + 2Mcf_\kappa,$$

with M=m + $\frac{1}{2c^2}$(E-V), at energy, E. Define Koeling and Harmon function,

$$\phi_\kappa = \frac{1}{2Mc}g'_\kappa,$$

where g'_κ is the radial derivative, m is the mass, c is the speed of light. After dropping spin-orbit and defining $P_l = rg_l$ and $Q_l = rcg_l$, the scalar-relativistic equations become

$$P'_l = 2MQ_l + \frac{1}{r}P_l \tag{3.34}$$

and

$$Q'_l = -\frac{1}{r}Q_l + [\frac{l(l+1)}{2Mr^2} + (V-E_l)]P_l. \tag{3.35}$$

As in non-relativistic equation, these two equations can be solved numerically using standard predictor-corrector. The spin-orbit term can be added in the final step and then we reach to the fully relativistic solution.

3.4.4 Solution of Poisson's Equation

The Kohn Sham potential consists of an exchange correlation term, $V_{XC}(\mathbf{r})$ and a Coulomb term, $V_C(\mathbf{r})$, which is the sum of the Hartree potential, $V_H(\mathbf{r})$ and the nuclear potential. then the Poisson's equation of Coulomb term (in atomic units, e^2=1) is

$$\nabla^2 V_C(\mathbf{r}) = 4\pi\rho(\mathbf{r})$$

The solution of Poisson's equation in reciprocal space is

$$V_C(\mathbf{G}) = \frac{4\pi\rho(\mathbf{G})}{|\mathbf{G}|^2}$$

Two groups ([Hamann 1979] and Weinert [Weinert 1981]) developed a hybrid method known as the pseudo-charge method which is used to solve the Poisson's equation and illustrated in the following diagram Fig. 3.4.7.

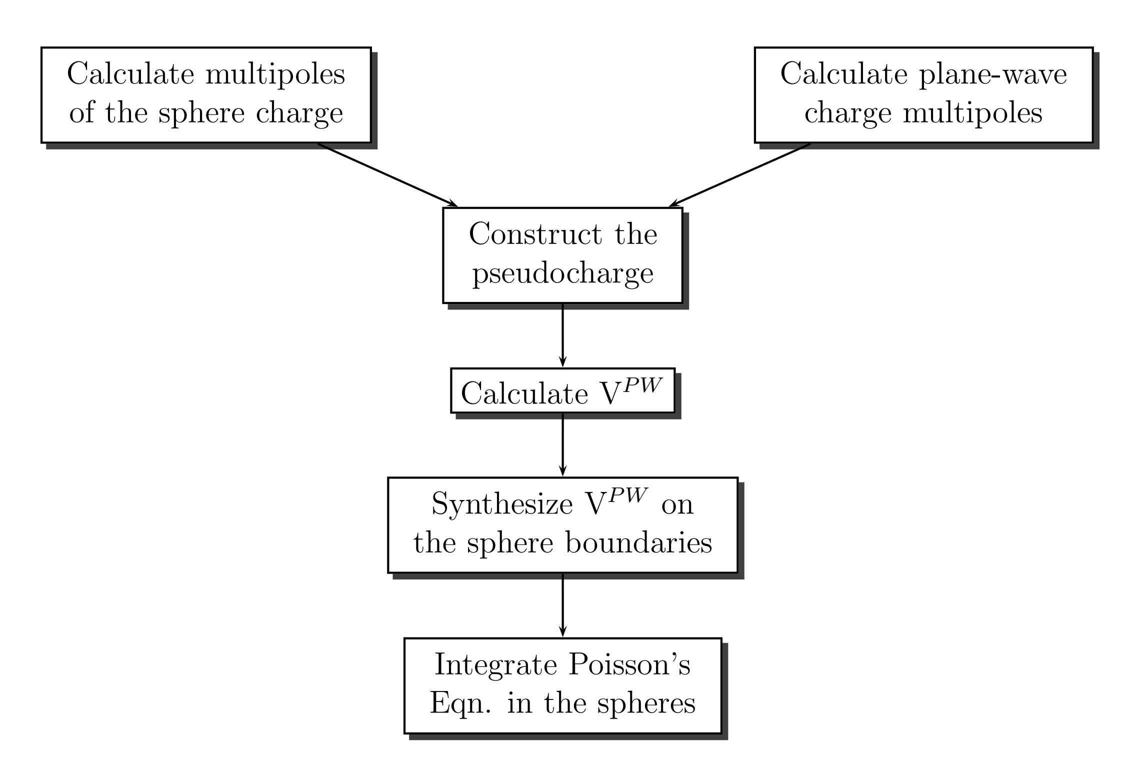


Figure 3.4.7. The pseudo-charge method diagram which is used to solve the Poisson's equation.

3.4.5 Brillouin Zone Integration and the Fermi Energy

In crystal, evaluation of many quantities (total energy, charge density, force, ...) required integration over the Brillouin zone, and using symmetry reduce to integrals over the irreducible wedge of Brillouin zone (IBZ). The most used

approaches are the tetrahedron method [Lehmann *et al.* 1970, Blöchl *et al.* 1994] and the special points method [Monkhorst *et al.* 1976, Pack and Monkhorst 1977]. In the tetrahedron method, the zone is divided into tetrahedral and the band energies and wave functions are calculated at **k**-points on the vertices. where the Fermi energy are determined by interpolated the band energies between the vertices. On the other hand, the special points method are performed as weighted sums over a grid of representative **k**-points.

Determination of the Fermi Energy by using special points and temperature broadening [Abragam 1961] is carried out by:

$$\sum_{\mathbf{k},j} w(\mathbf{k}) F(\epsilon_{\mathbf{k},j}, E_F, T) = n_{tot}, \tag{3.36}$$

where the sum is over the special **k**-points and bands(j), $w(\mathbf{k})$ is the weight factor that describes the number of states at energy $\epsilon_{\mathbf{k},j}$ and F is a Fermi broadened occupation function defined as:

$$F(\epsilon, E_F, T) = [exp(\frac{\epsilon - E_F}{kT}) + 1]^{-1}$$

Here Eq. (3.36) is solved by bisection method to estimate the Fermi energy.

3.4.6 Total Energy in Spin-Polarized Systems

Generalized the standard DFT to the spin-polarized DFT needs the charge density to be augmented by a magnetization density. In nature, magnetism is often non-collinear *i.e.* the magnetization direction, in fact, vary from place to place. The reasons for the non-collinearity:

- Fermi surface effects leading to spin spirals.
- Frustration of exchange interactions as in triangular lattice systems.
- Frustration between spin-orbit and exchange, like in U_3P_4
- DZyaloshinskii-Moriya interaction, which leads to the helical magnetic order of MnSi.

However, many interesting magnetic systems either are collinear or are well approximated as collinear. The total electron density may be divided into two parts that depends on the two spin channels

$$\rho(\mathbf{r}) = \rho\uparrow(\mathbf{r}) + \rho\downarrow(\mathbf{r}) \tag{3.37}$$

and the difference between two densities give the spin magnetic moments m,

$$m(\mathbf{r}) = \rho\uparrow(\mathbf{r}) - \rho\downarrow(\mathbf{r}) \tag{3.38}$$

The total energy of a periodic solid (with frozen nuclear positions) within the DFT framework is given simply by,

$$E[\rho\uparrow,\rho\downarrow] = T_s[\rho\uparrow,\rho\downarrow] + U[\rho\uparrow,\rho\downarrow] + E_{xc}[\rho\uparrow,\rho\downarrow]. \tag{3.39}$$

where $T_s[\rho\uparrow,\rho\downarrow]$ is the kinetic energy of a noninteracting electron gas and is given by

$$T_s[\rho\uparrow,\rho\downarrow] = \sum i \int \psi_i^*(\vec{r})\mathbf{K}_{op}\psi_i(\vec{r})d\vec{r}. \tag{3.40}$$

The one-particle kinetic energy operator $\mathbf{K}_{op}$ is given nonrelativistically or relativistically. The ψ_i's are solutions of the effective one-electron Schrödinger (or Dirac) equation

$$[\mathbf{K}_{op} + V_{eff}(\vec{r})]\psi_i(\vec{r}) = \epsilon_i\psi_i(\vec{r}) \tag{3.41}$$

The effective potential operator $V_{eff}(\vec{r})$ is

$$V_{eff}(\vec{r}) = V_c(\vec{r}) + \mu_{xc}(\vec{r})$$

$U[\rho\uparrow,\rho\downarrow]$ is the interaction energy between all charges in the system:

$$\begin{aligned} U[\rho\uparrow,\rho\downarrow] = \frac{1}{2}[&\int \frac{[\rho\uparrow(\vec{r}\,)+\rho\downarrow(\vec{r}\,)][\rho\uparrow(\vec{r}\,')+\rho\downarrow(\vec{r}\,')]d\vec{r}}{|\vec{r}-\vec{r}\,'|} \\ &- 2\sum_\alpha Z_\alpha \int \frac{[\rho\uparrow(\vec{r}\,)+\rho\downarrow(\vec{r}\,)]d\vec{r}}{|\vec{r}-\vec{R}_\alpha|} + {\sum_{\alpha,\beta}}' \frac{Z_\alpha Z_\beta}{|\vec{R}_\alpha - \vec{R}_\beta|}] \end{aligned} \tag{3.42}$$

where Z_i is the nuclear charge at $\vec{R}_i$. Assuming N unit cells of volume Ω in the crystal and put Coulomb potential at $\vec{r}$ we write

$$U = \frac{N}{2}\left[\int_\Omega [\rho\uparrow(\vec{r}\,)+\rho\downarrow(\vec{r}\,)]V_c(\vec{r}\,)d\vec{r} - \sum_\nu Z_\nu V_M(\vec{\gamma_\nu}\,)\right] \tag{3.43}$$

We have defined Coulomb potential ($V_c(\vec{r}\,)$) and a generalized Madelung potential ($V_M(\vec{\gamma_\nu})$), i.e., the Coulomb potential at γ_ν due to all charges in the crystal except for the nuclear charge at this site, as

$$V_c(\vec{r}\,) = \int \frac{[\rho\uparrow(\vec{r}\,')+\rho\downarrow(\vec{r}\,')]}{|\vec{r}-\vec{r}\,'|}d\vec{r} - \sum_\alpha \frac{Z_\alpha}{|\vec{r}-\vec{R}_\alpha|}, \tag{3.44}$$

and

$$V_M(\vec{\gamma}_\nu) = \int \frac{[\rho\uparrow(\vec{r}\,)+\rho\downarrow(\vec{r}\,)]d\vec{r}}{|\vec{r}-\vec{\gamma}_\nu|} - {\sum_\alpha}' \frac{Z_\alpha}{|\vec{R}_\alpha - \vec{\gamma}_\nu|}, \tag{3.45}$$

The average potential on a sphere of radius R_ν centered at $4\vec{\gamma}_\nu$ due to all charges is given by

$$S(R_\nu) = S_0(R_\nu) + Z_\nu/R_\nu. \tag{3.46}$$

If we assume that we want the potential at the center of the sphere (l=0) then V_M is written as

$$\begin{aligned} V_M(\vec{\gamma}_\nu) &= \frac{1}{R_\nu}\left[R_\nu S_0(R_\nu) + Z_\nu - Q_\nu\right] + \sqrt{4\pi}\int_0^{R_\nu} drr[\rho_{00}\uparrow(r_\nu) + \rho_{00}\downarrow(r_\nu)] \\ &= \frac{1}{R_\nu}\left[R_\nu S_0(R_\nu) + Z_\nu - Q_\nu\right] + \left\langle \frac{1}{r}[\rho\uparrow(\vec{r}) + \rho\downarrow(\vec{r})]\right\rangle_\nu, \end{aligned} \tag{3.47}$$

A simple expression for the kinetic energy per unit cell can be obtained by multiplying Eq. (3.41) by ψ_i^*, integrating and summing over all occupied states to yield

$$\begin{aligned} T_s[\rho\uparrow,\rho\downarrow] &= \sum_i \epsilon_i - \int_\Omega V_{eff}(\vec{r}\,)[\rho\uparrow(\vec{r}\,) + \rho\downarrow(\vec{r}\,)]d\vec{r} \\ &= \sum_i \epsilon_i - \int_\Omega V_c(\vec{r}\,)[\rho\uparrow(\vec{r}\,) + \rho\downarrow(\vec{r}\,)]d\vec{r} \\ &\quad - \int_\Omega \mu_{xc}(\vec{r}\,)[\rho\uparrow(\vec{r}\,) + \rho\downarrow(\vec{r}\,)]d\vec{r} \end{aligned} \tag{3.48}$$

Then the total energy per unit cell is

$$\begin{aligned} E &= \sum_i \epsilon_i - \frac{1}{2}\left[\left[\int_\Omega V_c(\vec{r}\,)[\rho\uparrow(\vec{r}\,) + \rho\downarrow(\vec{r}\,)]d\vec{r} + \sum_\nu Z_\nu\left\langle\frac{1}{r}[\rho\uparrow(\vec{r}) + \rho\downarrow(\vec{r}\,)]\right\rangle_\nu\right]\right. \\ &\quad - \int_\Omega \mu_{xc}(\vec{r}\,)[\rho\uparrow(\vec{r}\,) + \rho\downarrow(\vec{r}\,)]d\vec{r} - \frac{1}{2}\sum_\nu \frac{Z_\nu}{R_n u}\left[R_\nu S_0(R_\nu) + Z_\nu - Q_\nu\right] \\ &\quad + E_{xc}[\rho\uparrow,\rho\downarrow]. \end{aligned} \tag{3.49}$$

3.4.7 Computational Details

Density functional theory [Hohenberg and Kohn 1964, Kohn and Sham 1965], using the all-electron full-potential linearized augmented plane-wave (FP-LAPW) method [Singh 1989, Weinert 1981, Wimmer *et al.* 1981] implemented in WIEN2k [Blaha *et al.* 1990] package, is used to calculate the electronic structure and magnetic properties of a series of $Fe_{3-x}Mn_xZ$(Z=Al,Ge,Sb) compounds. The electronic exchange-correlation energy is treated using the generalized gradient approximation parametrized by Perdew-Burke-Ernzerhof (GGA-PBE) [Perdew *et al.* 1996]. The total energy dependence on the cell volume is fitted to the Murnaghan equation of state (EOS) [Murnaghan 1944] by:

$$E_{tot}(V) = \frac{B_0 V}{\acute{B}(\acute{B}-1)}\left[\left(\frac{V_0}{V}\right)^{\acute{B}} + \acute{B}\left(1 - \frac{V_0}{V}\right) - 1\right] + E_0 \tag{3.50}$$

where B_0 is the bulk modulus, $\acute{B}$ is the bulk modulus derivative and V_0 is the equilibrium volume.

By assuming the muffin-tin model for the crystal potential, the spherical harmonic expansion is used inside the muffin-tin sphere, and the plane wave basis set is chosen outside the sphere. The maximum value of angular momentum l_{max} =10 is taken for the valence wave function expansion inside the atomic spheres, while the charge density was Fourier expanded up to G_{max} = 14 (a.u.)$^{-1}$. The plane wave cut-off value $K_{max} \times R_{MT} = 8$ is used in the expansion of the plane wave in the interstitial region of the unit cell, where R_{MT} denotes the smallest atomic sphere radius (muffin tin radius) and K_{max} gives the magnitude of the largest K vector in the plane-wave expansion. The R_{MT} are taken to be 2.3 a.u. for Fe, Mn and to be 2.16 a.u. for Al, Ge and Sb.

The energy cut-off specified in the generated free atomic density was a bout -95 eV to separate the core and band states. The starting potential for the next cycle was typically obtained by a roughly 10% mixing of the new potential.

For k-space integration,a $15 \times 15 \times 15$ mesh was used in the irreducible wedge of the Brillouin zone(BZ). The BZ integrations were performed using the modified tetrahedron interpolation method [Blöchl *et al.* 1994](with division of 1/48-th of the BZ into 192 small tetrahedral).

For all calculations, the precision of the energy is 5.0 $\times 10^{-7}$,and the precision of the wave function and the potential are 1.0 $\times 10^{-6}$. Furthermore, fully relativistic effects are taken into account for core electrons, whereas scaler relativistic approximation is used for valence electrons. Indeed, it was found theoretically by Mavropoulos *et al.* [Mavropoulos *et al.* 2004] that the spin-orbit interaction has only a weak influence on the half-metallic ferromagnetism in Heusler compounds. Later Picozzi *et al.* [Picozzi *et al.* 2002] and Galanakis [Galanakis 2005] reported the same for Co_2-based Heusler compounds. Therefore, spin-orbit interaction is neglected in the calculations discussed here. Before the main calculations carried out the converging test should be performed to ensure that the total energy is converged both as a function of k-points and as a function of the cut-off energy for the plane wave basis set.

CHAPTER 4

RESULTS AND DISCUSSION

Introduction

This chapter presents our results and its analysis with details. It is divided into two sections, the first one is dealt with the stoichiometre Heusler alloys whereas the second for the non-stoichiometre.

4.1 Stoichiometric $Fe_{3-x}Mn_xZ$ (Z= Al, Ge, Sb) Systems

4.1.1 Structural properties

The variation of total energy with the volume is fitted to Muranghan equation of state (EOS) [Murnaghan 1944] to obtain the equilibrium lattice parameter and bulk modulus. Figures 4.1.1 to 4.1.3 show the minimization of total energy versus the lattice parameter. Table 4.1.1 lists these EOS parameters along with the available experimental data and previous theoretical calculations using different models. The calculated lattice parameters for various alloys are in a good agreement with previous experimental measurements [Bansal *et al.* 1994, Vinesh *et al.* 2009, Zhou and Bakker 1995, Rodriquez-Carvajal 1993, Takizawa *et al.* 2002, Yamashita *et al.* 2003] and also with the predictions of other computational methods [Lechermann *et al.* 2002, Fujii *et al.* 1995, Luo *et al.* 2008, Fujii *et al.* 2008]. Quantitatively, it is less than the experimental value by about 1 % and larger than previous computational results by about 1 %. In addition, the calculated bulk modulus decreases as Mn concentration increases.

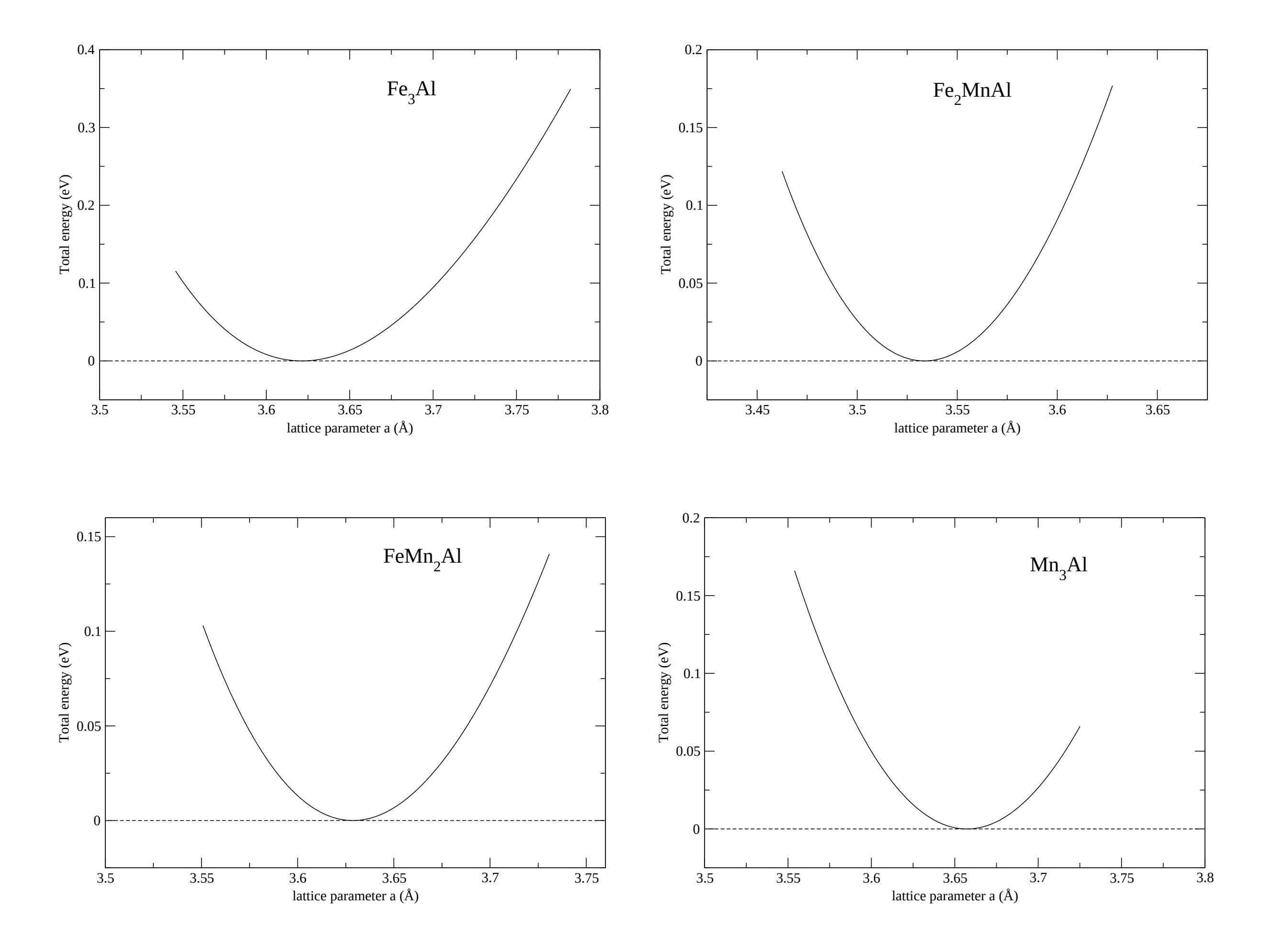


Figure 4.1.1. Calculated total energy for the stoichiometric $Fe_{3-x}Mn_xAl$ with the concentration x=0, 1, 2 and 3 as a function of lattice parameters.

We adopted the DO_3 structure for Fe_3Z(Z=Al, Ge, Sb) parent alloys although the $L1_2$ structure is the most stable according to GGA calculations, where we found that $\triangle E_{L1_2-DO_3}$= 59.6 , 12.0 and 122.0 meV for the compounds Fe_3Al, Fe_3Ge and Mn_3Sb, respectively. Furthermore, experimental results for Fe_3Z(Z=Al, Ge) indicate that the DO_3 structure is the stable phase in the narrow temperature range 900 K $<$ T $<$ 920 K for Fe_3Al and 373 K $<$ T $<$ 673 K for Fe_3Ge. However, below 900 K (373 K) the stable phase is the Cu_3Au-type ($L1_2$) structure for Fe_3Al (Fe_3Ge). So the DO_3 structure of Fe_3Z(Z=Al, Ge) is metastable and can be obtained experimentally by quenching. The equilibrium stable structure for Fe_3Al, Fe_3Ge and Mn_3Sb are controversial.

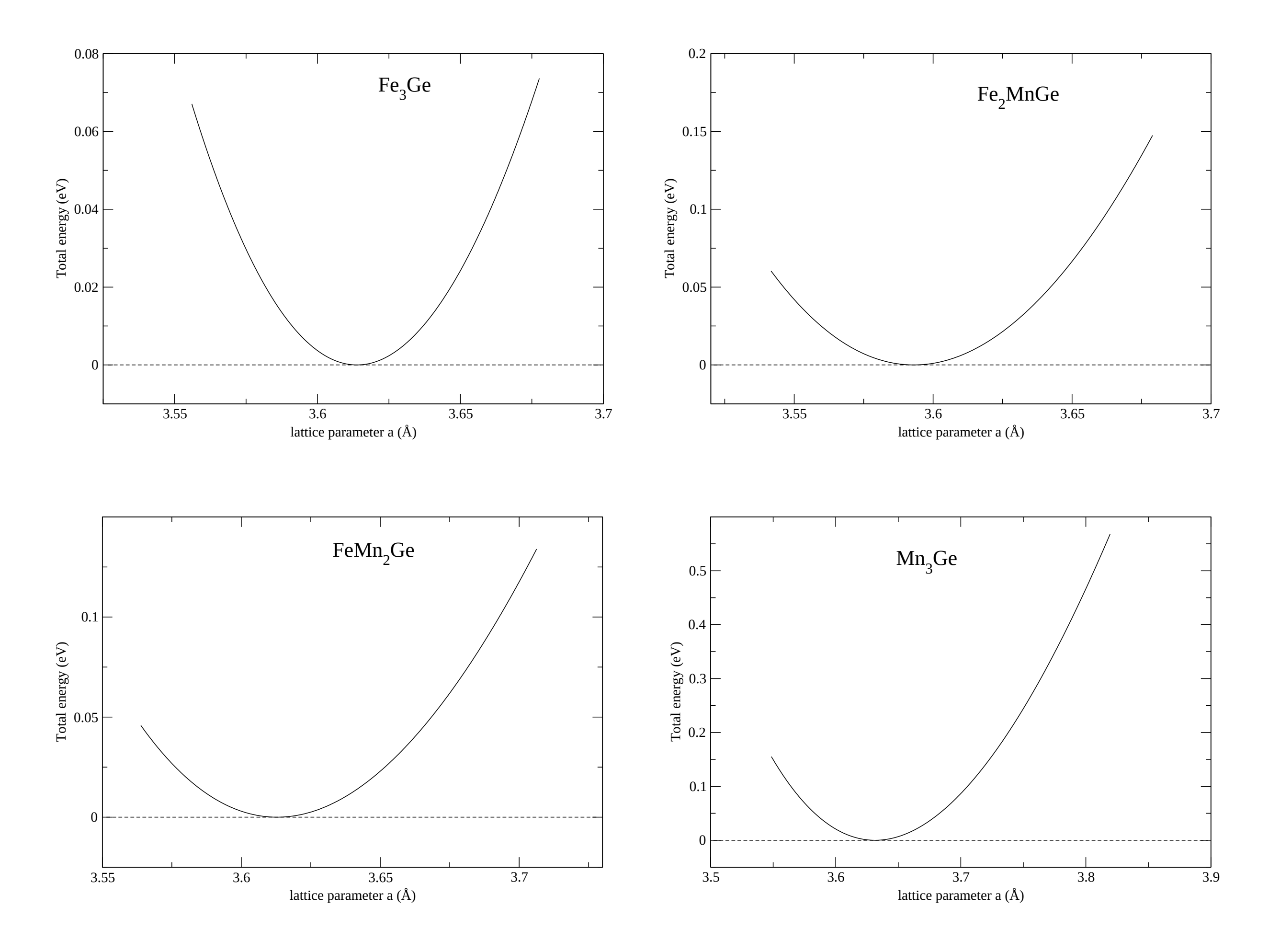


Figure 4.1.2. Calculated total energy for the stoichiometric $Fe_{3-x}Mn_xGe$ with the concentration x=0, 1, 2 and 3 as a function of lattice parameters.

Full Heusler alloys of the chemical formula Fe_2MnZ exhibit the $L2_1$ structure ($AlCu_2Mn$-type). Here, the two iron atoms occupy equivalent crystallographic sites A and C, while B sites are occupied by Mn atoms, and the metalloid (Z) on the D sites. The Mn atoms in the B sites are surrounded by 8 Fe[A,C] first nearest neighbors (nn's) forming a *bcc* arrangement. Consequently, each of Fe[A,C] atoms has 4 Mn[B] and 4 Z[D] as first nn's. The 4 metalloids [D] are located in a relative tetrahedral arrangement with respect to each other; this is also the case for the 4 Mn atoms in the B site. On the other hand, Mn_2FeZ possesses $CuHg_2Ti$-type structure, where the Mn atoms have two different sites, the Mn[A] atoms have 4 Mn[B] and 4 Al[D] as first nn's, while Mn[B] atoms are surrounded by 4 Mn[A] and

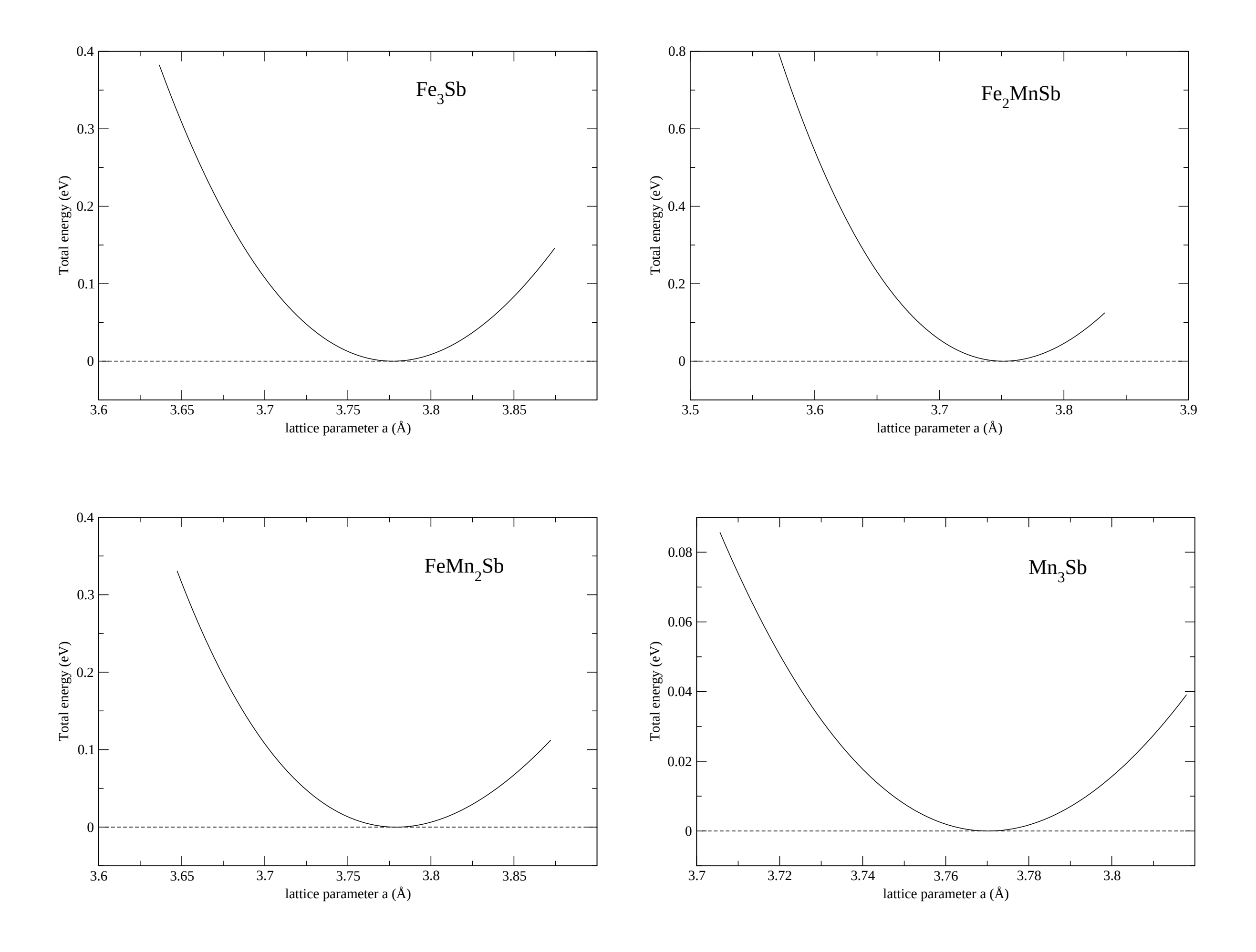


Figure 4.1.3. Calculated total energy for the stoichiometric $Fe_{3-x}Mn_xSb$ with the concentration x=0, 1, 2 and 3 as a function of lattice parameters.

4 Fe[C] as first nn's.

For the purpose of studying the effect of changing Mn concentration on the electronic and magnetic structures, we used a supercell of 16 atoms for all systems, see Fig. 2.2.2. The site preference of Mn atoms substituted is examined for some selected structures of the three series compounds up to x=3, where we found that they prefer to occupy B-site until they are completely filled. Then they start to fill A- or C-sites. For example, in Mn_2FeAl Heusler alloy, the effect of Mn-Al disorder is calculated by simulating the antisite substitution. This Mn-Al disorder significantly degrades the half metallicity of Mn_2FeAl.

Table 4.1.1. Structure, optimized lattice parameter (a), bulk modulus (B), the maximum valence electron band energy ($E_{V(max)}$), the minimum conduction electron band energy ($E_{C(min)}$), band gap (E_g), half-metallic gap (E_S) and polarization (P). For comparison and completeness, we tabulated experimental values and results from previous calculations.

compound	structure	$a(A°)$	B (GPa)	$E_{V(max)}$(eV)	$E_{C(min)}$(eV)	E_g (eV)	E_S(eV)	P(%)	Ref.
Fe_3Al	DO_3	5.750	169.9					35	
		5.738	169.3						[Lechermann *et al.* 2002]
		5.820(exp)							[Bansal *et al.* 1994]
	$L1_2$	3.653	169.4						
		3.651	174.9						[Lechermann *et al.* 2002]
Fe_2MnAl	$L2_1$(Fm-3m)	5.683	200.9	0.740	1.205	0.465		81	
		5.670							[Fujii *et al.* 1995]
		5.850(exp)							[Vinesh *et al.* 2009]
Mn_2FeAl	$L2_1$(F-43m)	5.760	150.2	0.674	1.218	0.544		99	
		5.725							[Luo *et al.* 2008]
Mn_3Al	DO_3	5.806	143.9	0.555	1.098	0.543	0.116	100	
		5.723							[Fujii *et al.* 2008]
Fe_3Ge	DO_3	5.736	167.7					20	
		5.760(exp)							[Zhou and Bakker 1995]
	$L1_2$	3.642	179.6						
		3.667(exp)							[Zhou and Bakker 1995]
Fe_2MnGe	$L2_1$(Fm-3m)	5.703	217.6	0.845	1.392	0.547		96	
	DO_3	5.780(exp)							[Rodriquez-Carvajal 1993]
Mn_2FeGe	$L2_1$(F-43m)	5.718	214.4	0.893	1.376	0.482		87	
		5.675							[Luo *et al.* 2008]
Mn_3Ge	DO_3	5.765	197.2	0.828	1.326	0.497		96	
		5.749							[Fujii *et al.* 2008]
	$L1_2$	3.654	170.5						
		3.800(exp)							[Takizawa *et al.* 2002]
Fe_3Sb	DO_3	5.996	159.5					28	
		5.900(exp)							[Bansal *et al.* 1994]
Fe_2MnSb	$L2_1$(Fm-3m)	5.955	192.6	0.979	1.668	0.689		82	
Mn_2FeSb	$L2_1$(F-43m)	5.999	141.2	0.731	1.127	0.396	0.063	100	
		5.925							[Luo *et al.* 2008]
Mn_3Sb	DO_3	5.985	174.4	0.768	1.375	0.607	0.043	100	
		5.930							[Fujii *et al.* 2008]
	$L1_2$	3.811	177.1						
		4.000(exp)							[Yamashita *et al.* 2003]

Nuclear magnetic resonance (NMR), Mössbauer and neutron diffraction measurements indicate that Mn atoms replace Fe atoms in Fe_3Z alloys only at B sites [Niculescu *et al.* 1983]. In the ternary compounds series $Fe_{3-x}T_xSi$ [Niculescu *et al.* 1983] and $(Fe_{1-x}M_x)_3Ga$ [Ishida *et al.* 1989], where T and M denote transition metal impurities (Mn, V) with valence electrons less than Fe, show strong preference for the B sites. However, those impurities (Co, Ni) with more valence electrons than Fe prefer A or C sites. Interestingly, Cr has anomalous behavior where it is distributed almost randomly at A, B, and C sites in $Fe_{3-x}Cr_xSi$ [Satua *et al.* 1993].

4.1.2 Electronic Structure

The calculated total and atom-resolved density of states (DOS) for $Fe_{3-x}Mn_xZ$ (Z= Al , Ge, Sb) are presented in Figs. 4.1.4 to 4.1.6. Due to the same crystal structure and site preference in these alloys, it can be seen that the general shape of their total DOS is quite similar in both spin channels. The majority spin states in Fe_3Z are almost full whereas minority spin states are only partly occupied leading to a sizable total spin magnetic moment for these compounds. The major contribution at Fermi level is from Fe[A,C] states. Furthermore, the majority conduction band is mainly contributed from both Fe[A,C] and Fe[B] atoms. The site-resolved DOS show how the Fe[A,C] close the gap in Fe_3Z compounds. From partial DOS spectrum of Fe_3Al and Fe_2MnAl as shown in Fig. 4.1.7, it is found that d-t_{2g} partial DOS are responsible for closing the gap. Drastic changes in the majority and minority states of Fe[A,C] DOS and to the total DOS occur when Fe is substituted by Mn atom in the B site. Consequently, for the Fe_2MnZ compounds, the valance and conduction bands in the minority spin channel are separated by a gap. Hence E_F is situated at the dip where there is a negligible DOS. We note that the main difference between Fe_2MnAl total DOS and those of the other two alloys Fe_2MnGe and Fe_2MnSb is the pseudogap appearing in its majority channel.

The compounds with the chemical composition Mn_2FeZ are examined in the two possible structure types ($AlCu_2Mn$ and $CuHg_2Ti$), where the $CuHg_2Ti$-type is found to be the most stable in all cases, in agreement with a previous theoretical study [Luo *et al.* 2008]. These alloys are found to have band gaps in the minority spin channels,(see Figs. 4.1.4 to 4.1.6) with energy gaps as in Table 4.1.1. For the case of Mn_3Z compounds the majority states become approximately half occupied and the band gaps in the minority states are wider.

The calculated local DOSs for the $Fe_{3-x}Mn_xAl$ series alloys are also shown in Fig. 4.1.4. The d states of Mn[B] are splitted into a doublet with e_g symmetry and a triplet with t_{2g} symmetry in the cubic crystal field. The origin of the gap in Mn_2FeZ, according to Galanakis *et al.* [Galanakis *et al.* 2002c], is established by

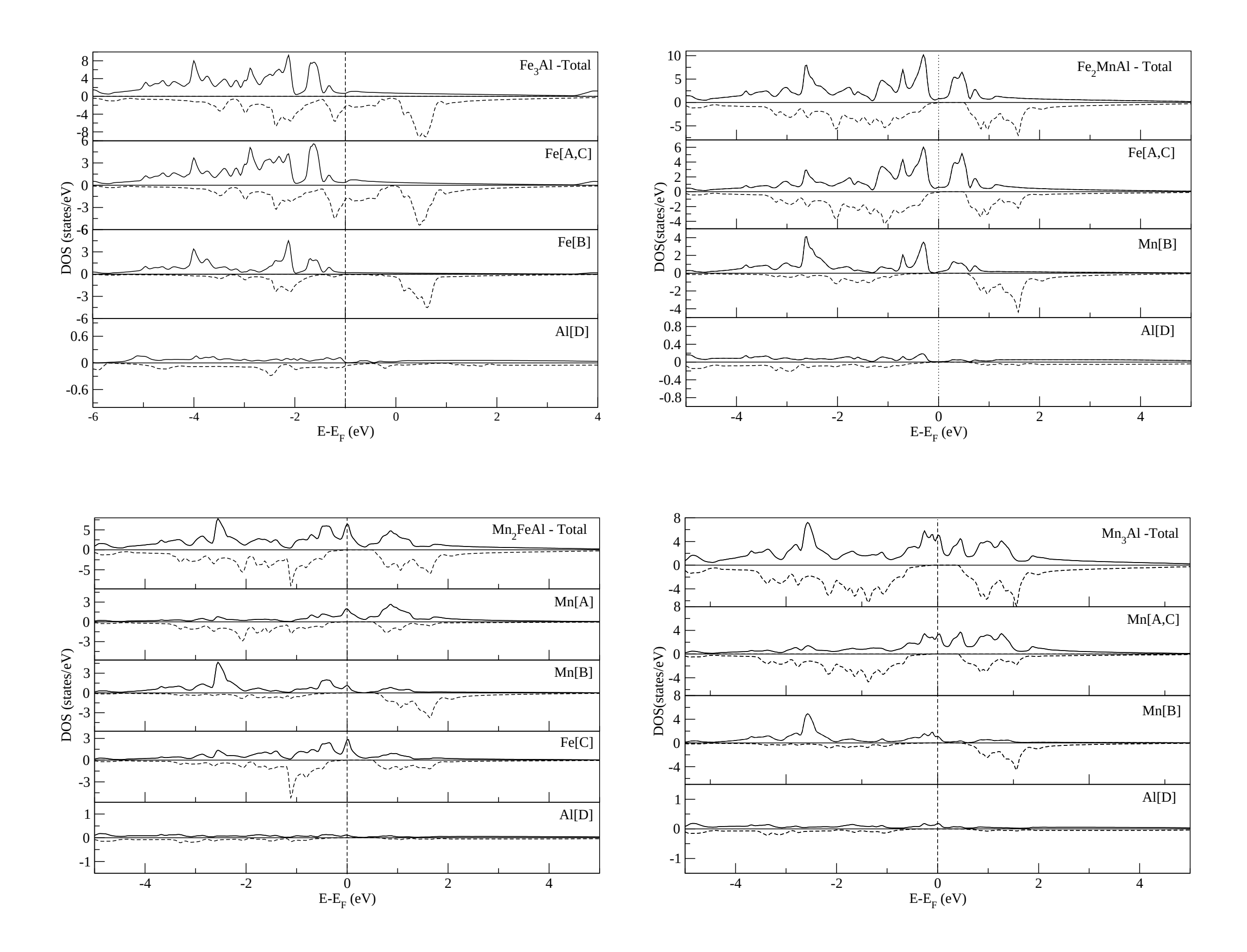


Figure 4.1.4. Total and atom-resolved DOS of the stoichiometric $Fe_{3-x}Mn_xAl$ for the concentration x=0, 1, 2 and 3.

the hybridization between the nearest neighbors of the Mn-Mn 3d orbital and also between the next nearest neighbors Fe-Mn 3d orbital. Thus, nonbonding states (e_u and t_{1u}) in the minority states are caused. It is well known that in covalent hybridization between high-valent and low-valent atoms, the bonding hybrids are mainly localized at the high-valent transition metal atom, such as Fe, while the unoccupied antibonding states are mainly at the low-valent transition metal, such as Mn [Galanakis *et al.* 2002b]. The energy region between -5 and +2 eV consists mainly of the 3d electrons of Fe and Mn atoms. It is clear that the Fe and Mn 3d states behave quite differently. In all alloys the 3d states of Fe locate in the region of -5 to +2 eV and almost identical in both spin directions. The Fe 3d

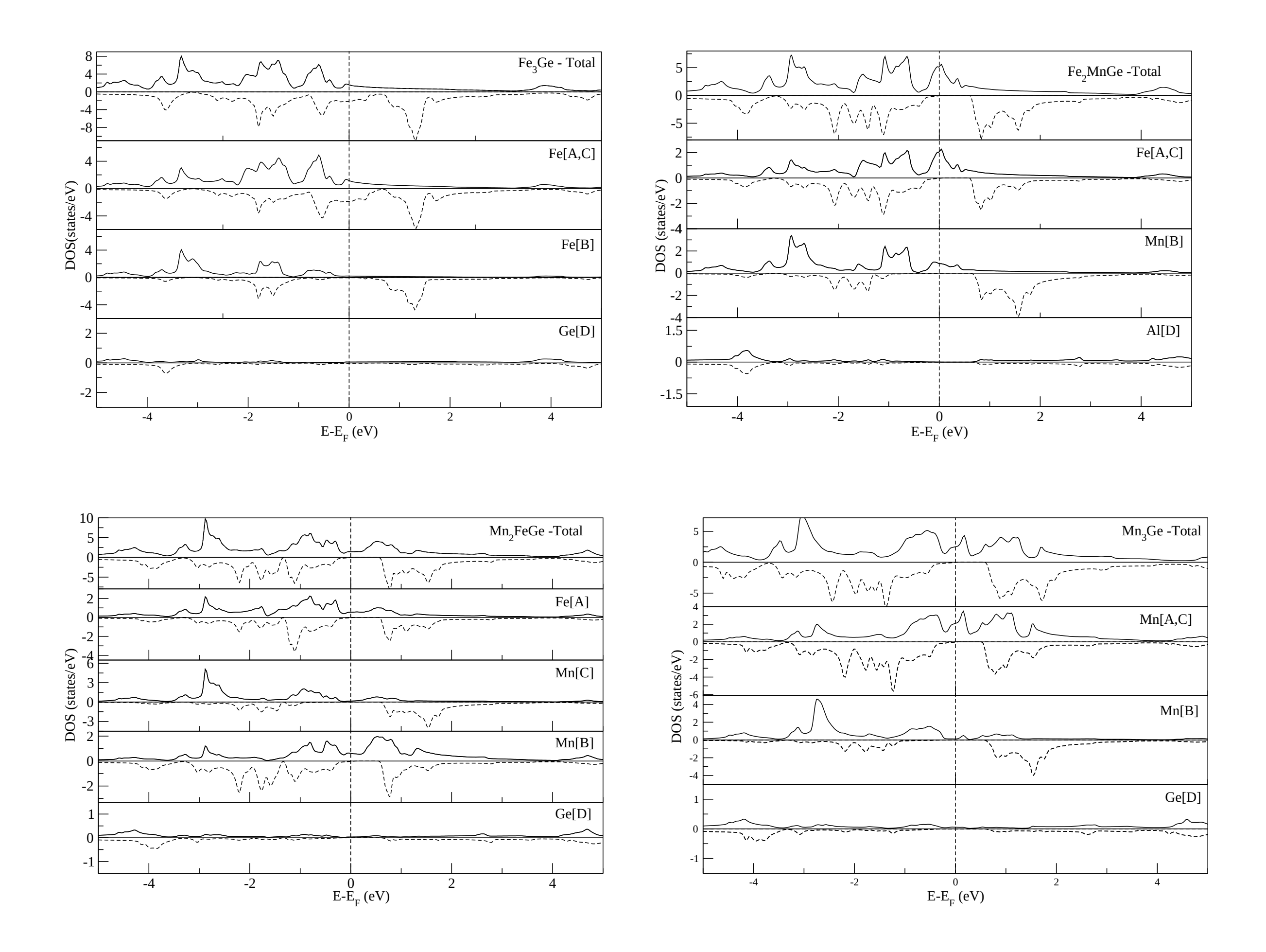


Figure 4.1.5. Total and atom-resolved DOS for the stoichiometric $Fe_{3-x}Mn_xGe$ for the concentration x=0, 1, 2 and 3.

states are almost completely occupied and show no exchange splitting. Therefore the Fe atoms only have a small moments and contribute little to the magnetism. The Mn $3d$ states extend from -3 to +2 eV, and a clear exchange splitting is observed between majority- and minority-spin states. This is the main source of the magnetic moment in these alloys. The partial DOS of the Mn atom at the B site shows a two-peak structure. This may be traced back to the e_g-t_{2g} splitting in cubic crystal field. In the majority-spin band, the bonding and antibonding peaks of Mn[B] are both below E_F. While in the minority- spin band, the antibonding peak is high above E_F. This large exchange splitting in DOS between majority and minority states leads to a large localized spin magnetic moment at the Mn[B]

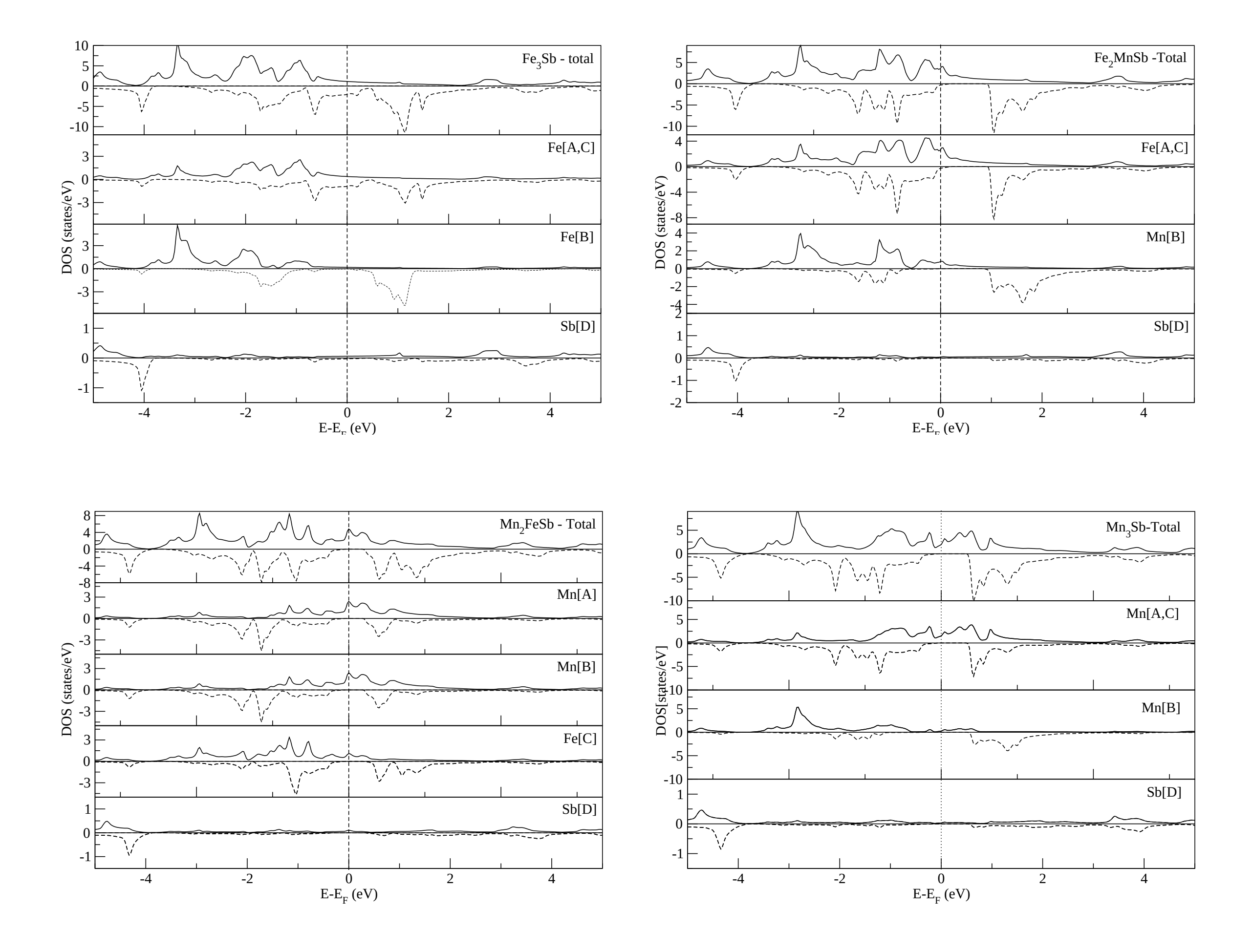


Figure 4.1.6. Total and atom-resolved DOS of the stoichiometric $Fe_{3-x}Mn_xSb$ for the concentration x=0, 1, 2 and 3.

sites [Kübler *et al.* 1983].

To illustrate more precisely the band gap, which is the energy gap between the highest occupied valence state and the lowest unoccupied conduction state in the minority spin channel, and the half-metallic gap (spin gap), which is defined as the energy gap between the highest occupied valence state and the Fermi state in the minority spin channel, the bandstructures are plotted for the different alloys in Figs. 4.1.8 to 4.1.10. Also the atom-resolved DOSs are used to clarify the contribution of individual electronic states. The lowest valence band located at majority and minority spin states between approximately -14 eV and -6 are totally

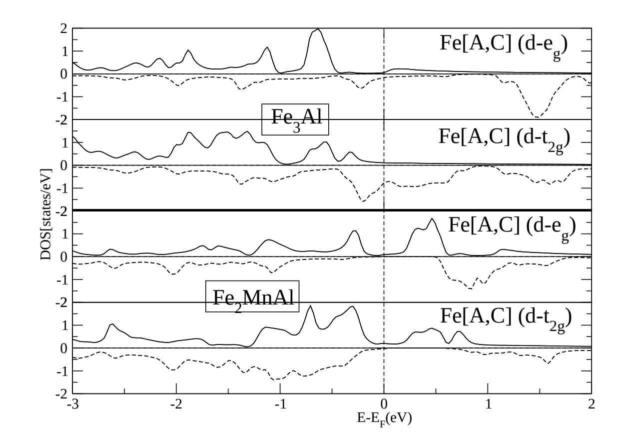


Figure 4.1.7. The Fe[A,C] d-e_g and d-t_{2g} partial DOS of Fe_3Al and Fe_2MnAl structures. Majority spin (solid line) and minority spin (dashed line).

due to Al 3s (-9 eV to -6 eV), Ge 4s (-12 eV to -9.5 eV), and Sb 5s (-12.5 eV to -10.5 eV) electrons does not appeared here. The next three bands between approximately -6 eV and -3 eV in $Fe_{3-x}Mn_xAl$ series, -7 eV to -3.5 in $Fe_{3-x}Mn_xGe$ series and -7.5 eV to -4 eV in $Fe_{3-x}Mn_xSb$ series are attributed to Al, Ge or Sb p and Fe and/or Mn d states(p-d hybridization). The upper bands between -3 eV and above Fermi level are mostly due to Fe and Mn d state. Comparison of majority and minority partial DOS shows that the double peak structure appeared arises from the hybridization of sp element p states and Fe 3d states, which forms covalent bond.

The common-band model which describes the formation of bonding and antibonding states with different weights on the different atoms, however, provides insight into the electronic structure of this class of compounds. The shape of the minority gap is mainly determined by the states of the atoms at the (A,C) sites as the gap in minority spin DOS of the B-site is much wider than those of A and C sites. In the X_2YZ Heusler compounds, X neighboring are $d_{x-x} \approx 3$ Å, resulting in the stronger overlap of d-like wave functions and in the appearance of the narrow energy gaps in DOS plots [Tobola *et al.* 1996].

The calculated spin-polarization are listed in Table 4.1.1. From this table, one can see that the full Heusler alloys exhibit high spin-polarized state (greater than 80 %), whereas the (Fe_3Z) binary alloys exhibit lower values (less than 40 %).

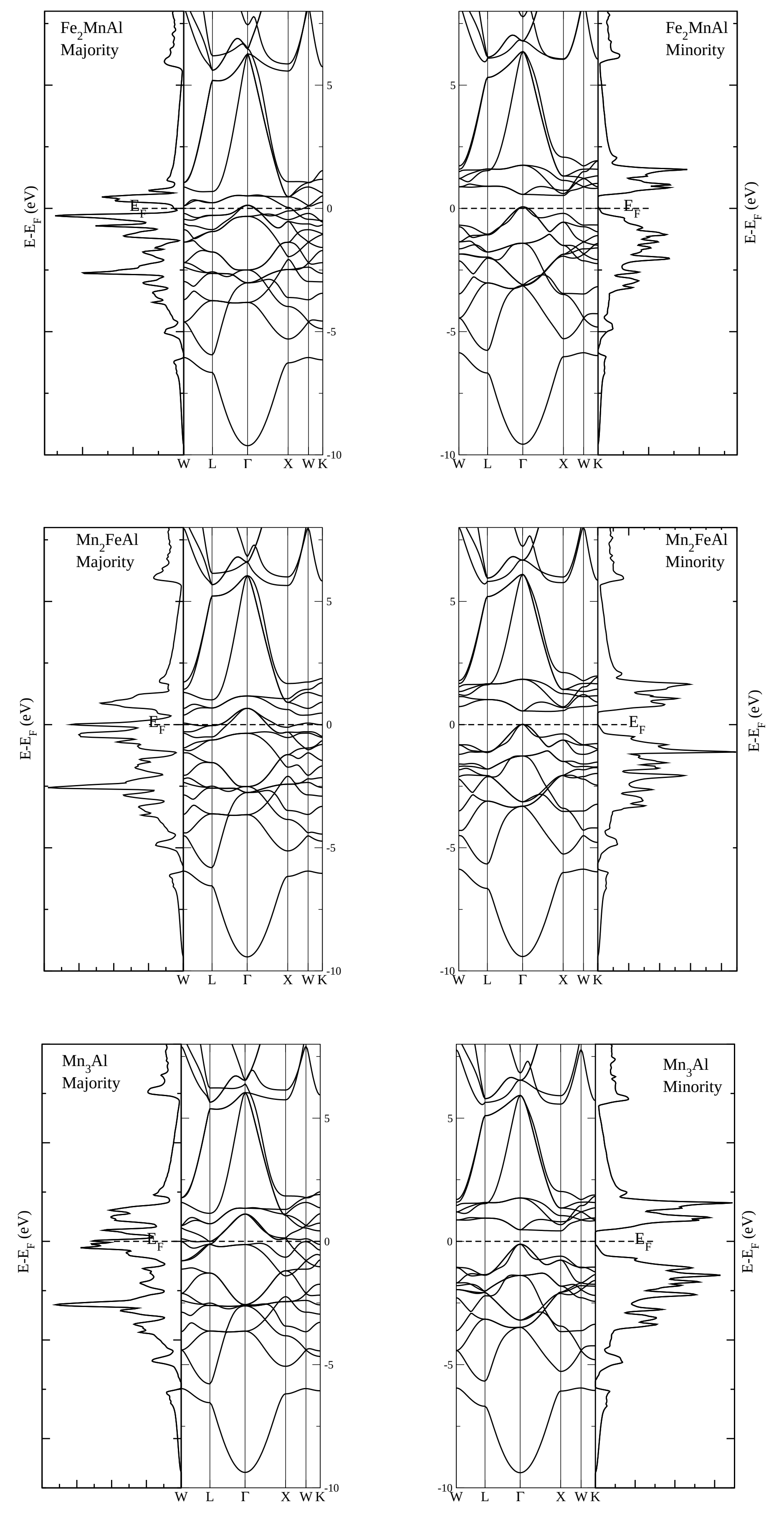


Figure 4.1.8. Total spin-projected DOS and bandstructure of stoichiometric $Fe_{3-x}Mn_xAl$ for the concentration x=0, 1, 2 and 3.

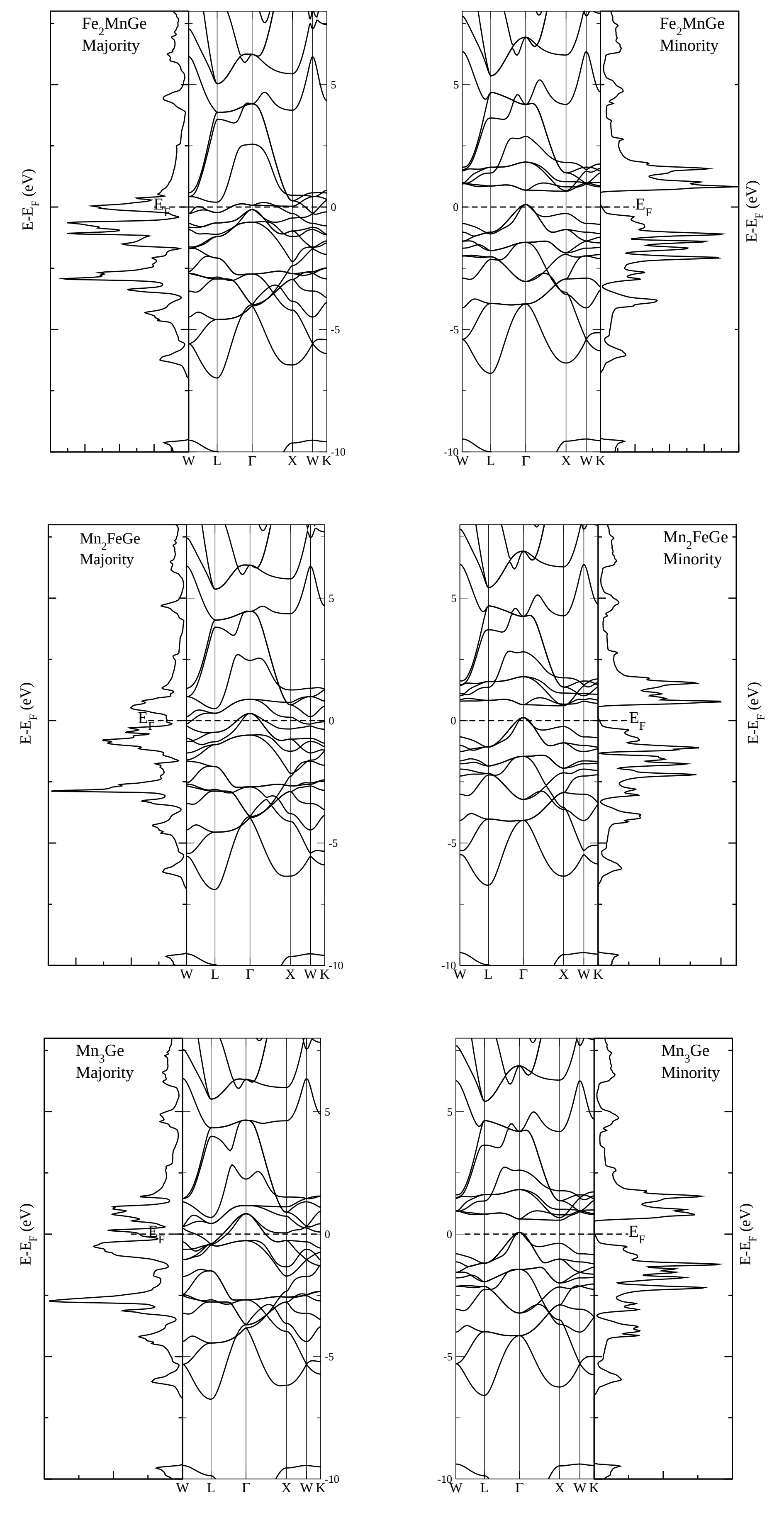


Figure 4.1.9. Total spin-projected DOS and bandstructure of stoichiometric $Fe_{3-x}Mn_xGe$ for the concentration x=0, 1, 2 and 3.

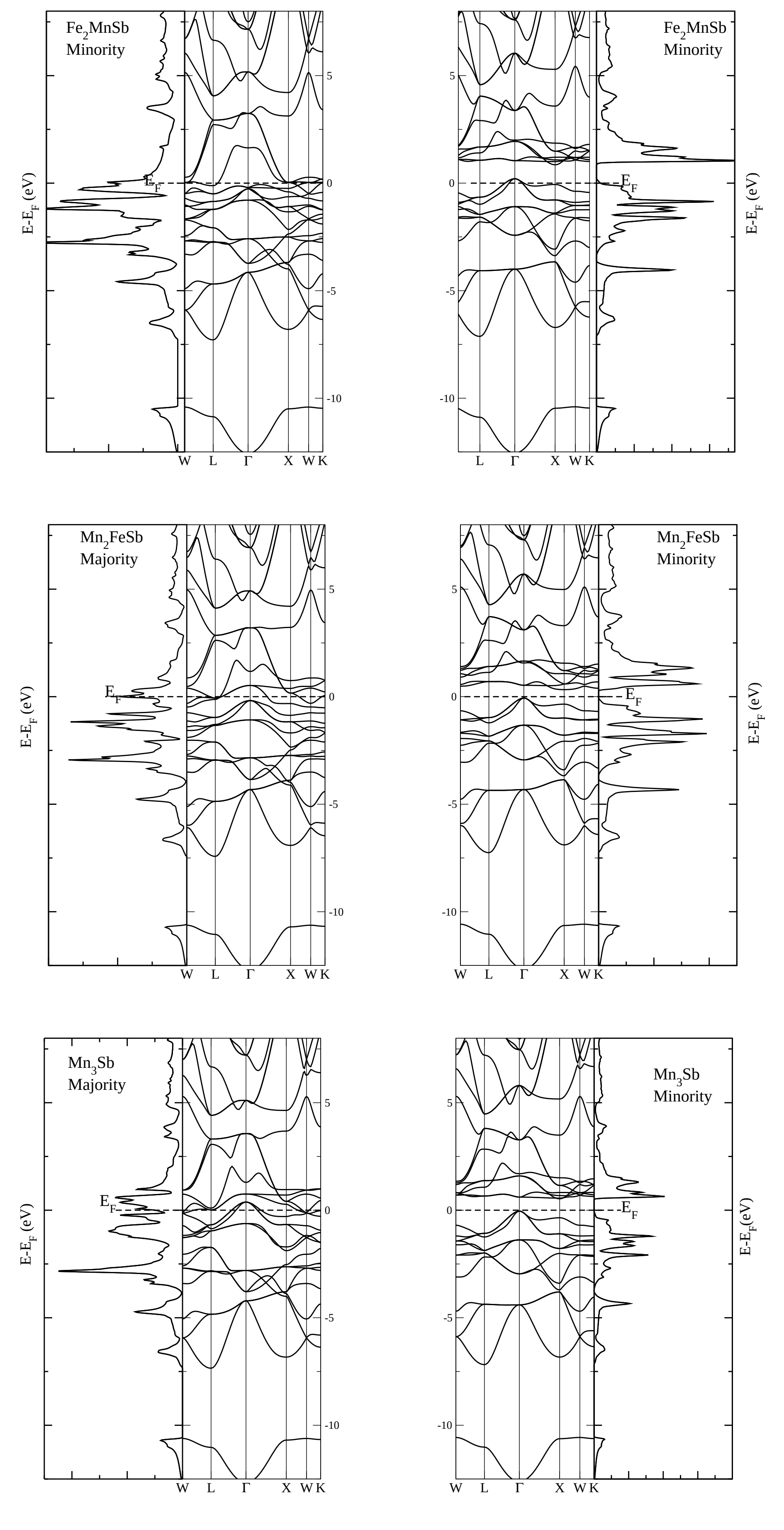


Figure 4.1.10. Total spin-projected DOS and bandstructure of stoichiometric $Fe_{3-x}Mn_xSb$ for the concentration x=0, 1, 2 and 3.

4.1.3 Spin Magnetic Moments

It is found that the Fe rich compounds (Fe_3Z and Fe_2MnZ) exhibit ferromagnetic phase, while the Mn rich compounds (Mn_2FeZ and Mn_3Z) are ferrimagnetic where the moments of Mn[A] and Mn[B] are large and antiparallel. The antiferromagnetic behavior is examined for the Mn_3Z alloys where the antiferromagnetic(AF) phase is found to be more stable than the ferromagnetic phase with energy difference 257 meV or $\sim$ 64 meV/atom in Mn_3Al alloy with zero total spin magnetic moment, consistent with Slater-Pauling rule. On the other hand, both Mn_3Ge and Mn_3Sb have ferrimagnetic phases.

In Table 4.1.2, we list the total and atom-resolved spin magnetic moments of different compound series. The calculated total spin magnetic moments increase with increasing the number of valence electrons and decrease with increasing Mn concentration, which are related to the extra electrons in the metalloid and the antiferromagnetic coupling of Mn moments, respectively.

The ferromagnetic half-metallic materials obey the Slater-Pauling rule [Galanakis *et al.* 2002c] as follows:

$$m_{HMF} = n_V - 6 \tag{4.1}$$

where m_{HMF} is the mean magnetic moment per atom and n_V is the mean number of valence electrons per atom. In the case of the compounds having four atoms per unit cell, one has to subtract 24 (6 multiplied by the number of atoms) form the accumulated number of valence electrons in unit cell N_V to find the spin magnetic moment per unit cell

$$m = N_V - 24 \tag{4.2}$$

Our calculated total spin magnetic moments obey Slater-Pauling behavior except on the Fe_3Z compounds, which gives larger values than those obtained from Slater-Pauling rule. Furthermore, the calculated local spin magnetic moments of Mn[B] sites roughly stay concentration independent for the different alloys, while the Fe[A,C] and Mn[A,C] site moments increase with x (see Table 4.1.2). By comparison with the available experimental values extrapolated to zero tempera-

ture and other comparable theoretical studies, quantitatively, these concentration variations agree very well with experiments, concerning the total moment. The spin moments of Fe atoms in Heusler compounds containing *sp* atom in different periods of the periodic table decrease with increasing the atomic number, whilst the spin moments of Mn show opposite behavior. This implies that, for the compounds with the larger atomic number *sp* atoms, the hybridization between Fe and Mn is smaller than compounds with the smaller atomic number of *sp* atoms, which results in a smaller Fe spin moment and a larger Mn spin moment and eventually makes the Mn moment even more localized.

Table 4.1.2. Calculated total spin magnetic moments $M^{TOT}(\mu_B)$, the local magnetic moments $m(\mu_B)$ and the magnetic phase for the $Fe_{3-x}Mn_xZ$ (Z= Al,Ge,Sb) alloys series.

structure	$M^{TOT}(\mu_B)$	$m^{Fe[A,C]}(\mu_B)$	$m^{Fe[B]}(\mu_B)$	$m^{Mn[A,C]}(\mu_B)$	$m^{Mn[B]}(\mu_B)$	$m^{Z}(\mu_B)$	magnetic phase
Fe_3Al	5.966	1.927	2.422	–	–	-0.087	FM
Fe_2MnAl	2.003	-0.152	—	–	2.323	-0.015	FM
$FeMn_2Al$	0.999	0.146	–	-1.798	2.669	-0.006	FM*
Mn_3Al	0.000	–	–	-1.415	2.826	0.012	AF
Fe_3Ge	5.624	1.624	2.575	–	–	-0.057	FM
Fe_2MnGe	3.024	0.209	–	–	2.626	-0.012	FM
Mn_2FeGe	2.013	0.506	–	-1.080	2.562	0.010	FM*
Mn_3Ge	1.002	–	–	-0.918	2.750	0.044	FM*
Fe_3Sb	6.116	1.789	2.730	–	–	-0.028	FM
Fe_2MnSb	4.140	0.670	–	–	2.875	-0.018	FM
Mn_2FeSb	3.000	1.164	–	-1.141	2.948	0.017	FM*
Mn_3Sb	2.000	–	–	-0.472	2.856	0.028	FM*

As given in Table 4.1.2, we note that Fe atom is ferromagnetically coupled to Mn with a small magnetic moment, while the *sp* atoms are antiferromagnetically coupled to Mn. Furthermore, the total spin magnetic moment per unit cell is close to an integer for all compounds except in Fe rich compounds.

Electronic structure calculations suggest that Mn_2FeAl, Mn_2FeGe and Mn_2FeSb are ferrimagnets with antiparallel alignment between Mn moments, but this antiferromagnetic coupling is weakened by increasing the number of valence electrons of Z atoms. Although the Fermi levels of Mn_2FeAl, Mn_2FeGe do not fall into the gap, they are very close to the edge of the gap, thus, they are called nearly HMFs. On the other hand, the Mn_3Al, Mn_2FeSb and Mn_3Sb are true half-metals with non-zero

spin gaps of 0.116, 0.063 and 0.043 eV, respectively. As seen in Figs. 4.1.4 and 4.1.6, the DOSs of these compounds are mainly characterized by large exchange splitting of the Mn *d* states, which leads to the localized magnetic spin moment at Mn site ($\sim 2.85\ \mu_B$). Substitution of the *sp* atoms cannot be responsible for the formation of the band gap, but results in a shift in the Fermi level and a loss of half-metallicity. Our result for the band gap of Mn_2FeAl alloy (0.54 eV) is in agreement with that of Luo *et al.* [Luo *et al.* 2008] (0.44 eV) using ultrasoft pseudopotential method. They argue that this system is a real half-metallic compound. However, we found that the spin gap (the energy difference between the Fermi level and the highest occupied valence state in the minority channel) is close, which means that this alloy is nearly half metallic. Another group, using KKR formalism with LDA parameterization, found that Fe_2MnAl alloy is a candidate of half-metallic material (see References [Galanakis *et al.* 2002c] and [Galanakis 2005]), whereas our calculations for this system show that it is nearly half metallic.

4.2 Non-Stoichiometric $Fe_{3-x}Mn_xZ$ (Z= Al, Ge, Sb) Systems

In this section, the investigation of the three series of non-stoichiometric $Fe_{3-x}Mn_xZ$ (Z= Al, Ge, Sb) systems are presented.

4.2.1 Structural Properties

In this subsection the properties of $Fe_{3-x}Mn_xZ$ (Z= Al, Ge, Sb) with $x = 0.25$, 0.50, 0.75, 1.25, 1.50, 1.75, 2.25, 2.50, and 2.75 are presented. The symmetry and space group of these systems change as a function of Mn concentration(as seen in Table 4.2.3). For $x < 1$, Fe atoms at B-sites in Fe_3Z are replaced by Mn atoms whereas for $x > 1$ the Mn atoms start to replace Fe atoms at A or C sites where Fe atoms still prefer A- or C-site. However, for Mn-rich compounds ($x = 2$) the Mn atoms occupy the three sites A, B and C. The energy versus the lattice parameter for non-stoichiometre $Fe_{3-x}Mn_xZ$ compounds are shown in Figs. 4.2.11 to 4.2.13. Table 4.2.3 summarizes the structural and electronic properties of nonstoichiometric $Fe_{3-x}Mn_xZ$ alloys with $0< x <3$. All compounds are modeled using a cubic supercell of 16 atoms except for $Fe_{2.5}Mn_{0.5}Z$ which is also modeled using a tetragonal primitive cell, which is found to be the most stable structure. The space group is P/4mmm with a lattice parameter ratio of $c/a=\sqrt{2}$. The lattice parameters are a = 4.059, 4.026 and 4.228 Å and c = a_c = 5.741, 5.693 and 5.979 Å for Z= Al, Ge and Sb, respectively, where a_c is the lattice parameter of the initially cubic $L2_1$ cell. The Fe related to the X position occupies the $(\frac{1}{2}, 0, \frac{1}{4})$ position in the supercell, the Fe dedicated to the Y position is now on $(\frac{1}{2}, \frac{1}{2}, \frac{1}{2})$, and Mn is placed on (0,0,0). In this supercell, the Z atoms occupy two different positions, being located at $(\frac{1}{2}, \frac{1}{2}, 0)$ and $(0, 0, \frac{1}{2})$. The other space groups and Wyckoff positions are tabulated in appendix B.

Table 4.2.3. Structure, optimized lattice parameter a, bulk modulus B, band gap E_g and polarization P.

Compound	Space group	$a(\AA)$	B (GPa)	E_g (eV)	P(%)
$Fe_{2.75}Mn_{0.25}Al$	$Pm\bar{3}m$ (221)	5.741	172.9	–	38.5
$Fe_{2.5}Mn_{0.5}Al$	P4/mmm (123)	4.059	132.7	–	40
$Fe_{2.25}Mn_{0.75}Al$	$Pm\bar{3}m$ (221)	5.726	197.4	0.405	100
$Fe_{1.75}Mn_{1.25}Al$	$P\bar{4}3m$ (215)	5.694	194.1	0.311	88
$Fe_{1.5}Mn_{1.5}Al$	$Pn\bar{3}m$ (224)	5.698	180.8	0.274	100
$Fe_{1.25}Mn_{1.75}Al$	$P\bar{4}3m$ (215)	5.731	157.6	0.356	98
$Fe_{0.75}Mn_{2.25}Al$	$P\bar{4}3m$ (215)	5.726	134.3	0.349	100
$Fe_{0.5}Mn_{2.5}Al$	$P4_2$/nnm (134)	5.696	150.7	0.491	100
$Fe_{0.25}Mn_{2.75}Al$	$P\bar{4}3m$ (215)	5.708	156.2	0.595	100
$Fe_{2.75}Mn_{0.25}Ge$	$Pm\bar{3}m$ (221)	5.724	166.4	–	22
$Fe_{2.5}Mn_{0.5}Ge$	P4/mmm (123)	4.026	210.9	–	62
$Fe_{2.25}Mn_{0.75}Ge$	$Pm\bar{3}m$ (221)	5.701	213.0	0.447	100
$Fe_{1.75}Mn_{1.25}Ge$	$P\bar{4}3m$ (215)	5.697	209.2	0.332	90
$Fe_{1.5}Mn_{1.5}Ge$	$Pn\bar{3}m$ (224)	5.703	205.9	0.282	95
$Fe_{1.25}Mn_{1.75}Ge$	$P\bar{4}3m$ (215)	5.715	194.4	0.221	94
$Fe_{0.75}Mn_{2.25}Ge$	$P\bar{4}3m$ (215)	5.729	180.9	0.243	90
$Fe_{0.5}Mn_{2.5}Ge$	$P4_2$/nnm (134)	5.751	190.4	0.389	94
$Fe_{0.25}Mn_{2.75}Ge$	$P\bar{4}3m$ (215)	5.748	192.4	0.292	100
$Fe_{2.75}Mn_{0.25}Sb$	$Pm\bar{3}m$ (221)	5.985	158.1	–	24.4
$Fe_{2.5}Mn_{0.5}Sb$	P4/mmm (123)	4.228	148.8	–	28
$Fe_{2.25}Mn_{0.75}Sb$	$Pm\bar{3}m$ (221)	5.978	160.2	0.063	88
$Fe_{1.75}Mn_{1.25}Sb$	$P\bar{4}3m$ (215)	5.949	197.4	0.045	85
$Fe_{1.5}Mn_{1.5}Sb$	$Pn\bar{3}m$ (224)	5.981	188.4	0.057	86
$Fe_{1.25}Mn_{1.75}Sb$	$P\bar{4}3m$ (215)	6.01	135.4	0.051	99
$Fe_{0.75}Mn_{2.25}Sb$	$P\bar{4}3m$ (215)	5.992	157.7	0.079	95
$Fe_{0.5}Mn_{2.5}Sb$	$P4_2$/nnm (134)	5.975	164.6	0.499	100
$Fe_{0.25}Mn_{2.75}Sb$	$P\bar{4}3m$ (215)	5.988	172.8	0.021	100

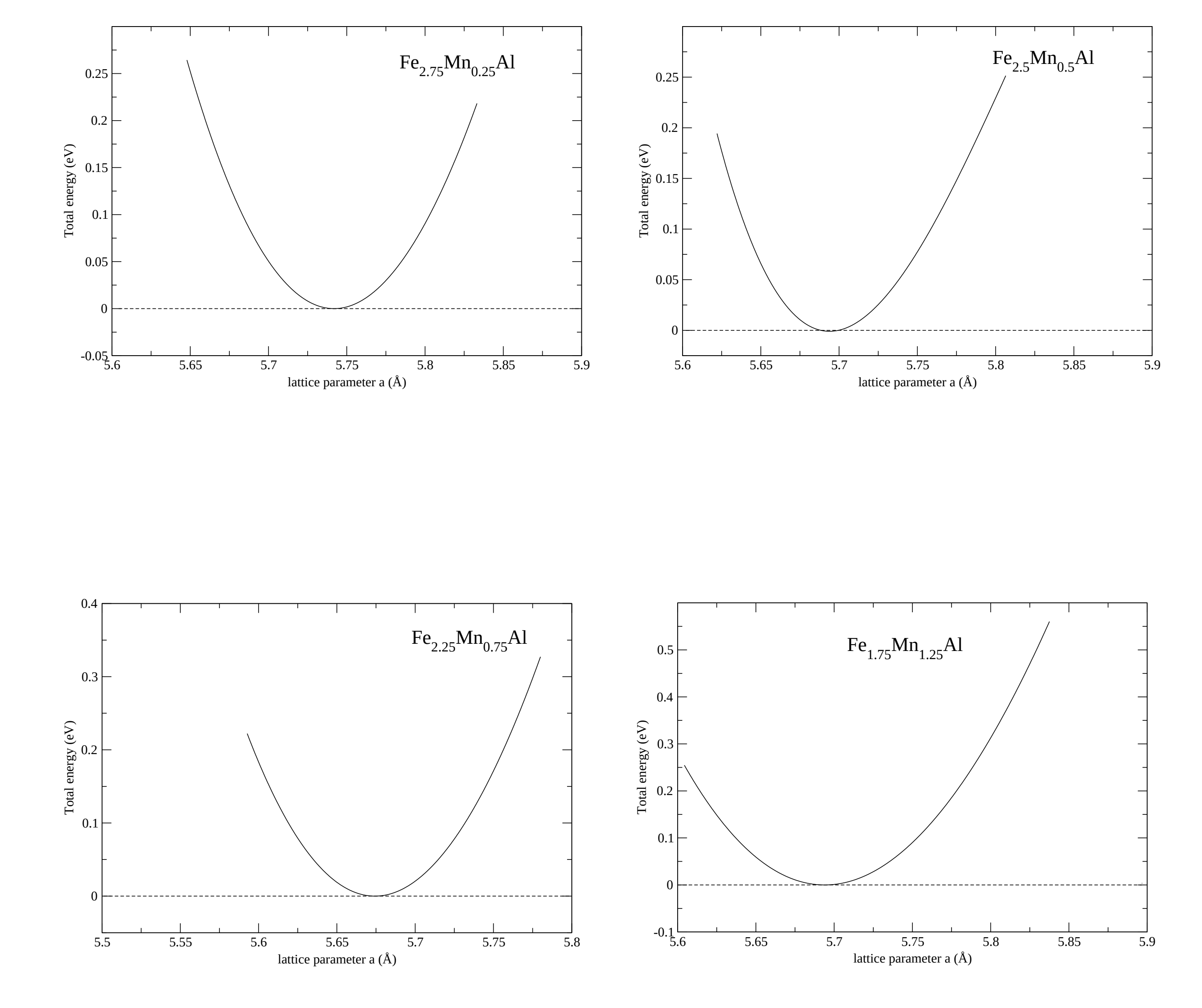


Figure 4.2.11. The energy versus the lattice parameter for non-stoichiometre $Fe_{3-x}Mn_xAl$.

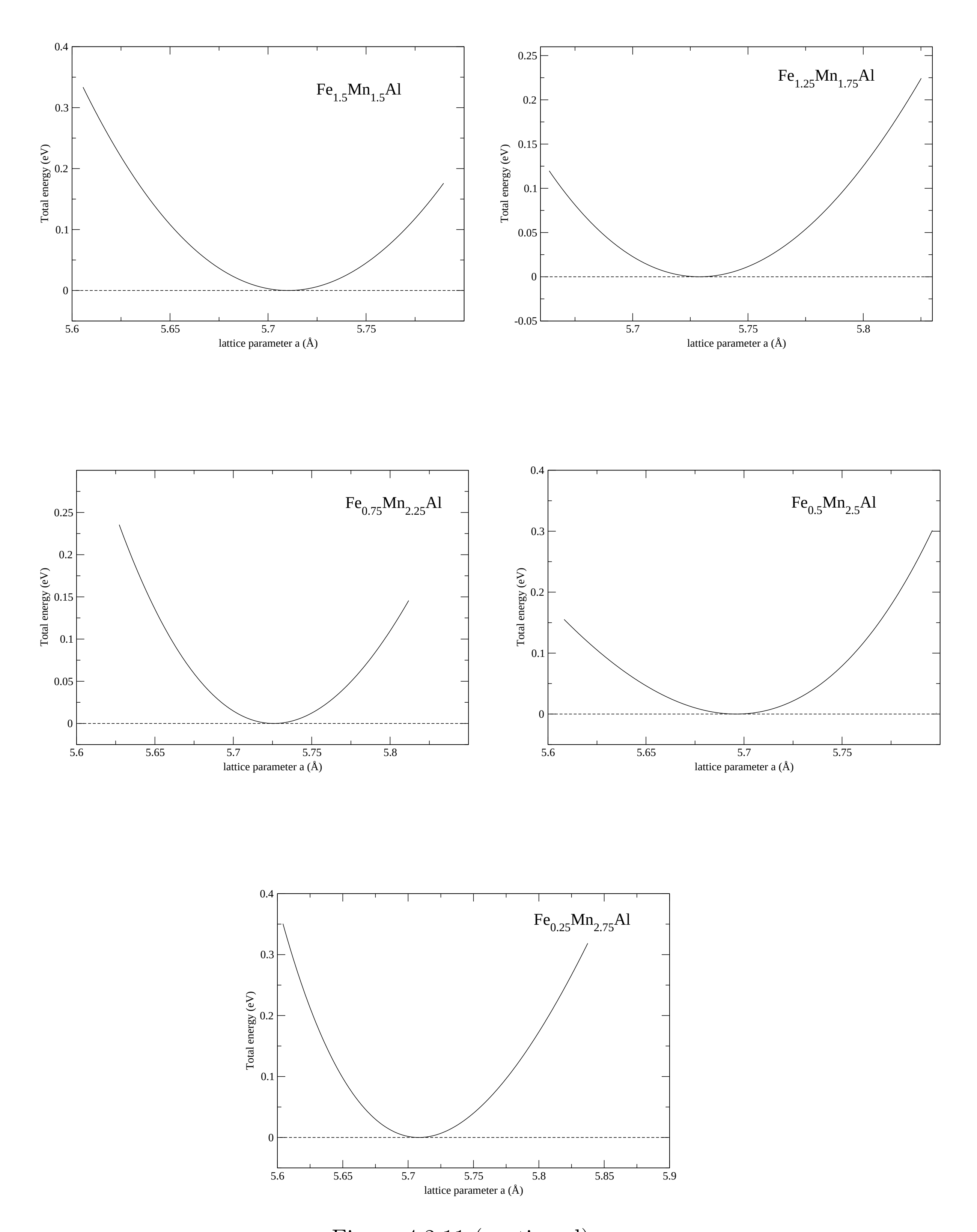


Figure 4.2.11 (continued)

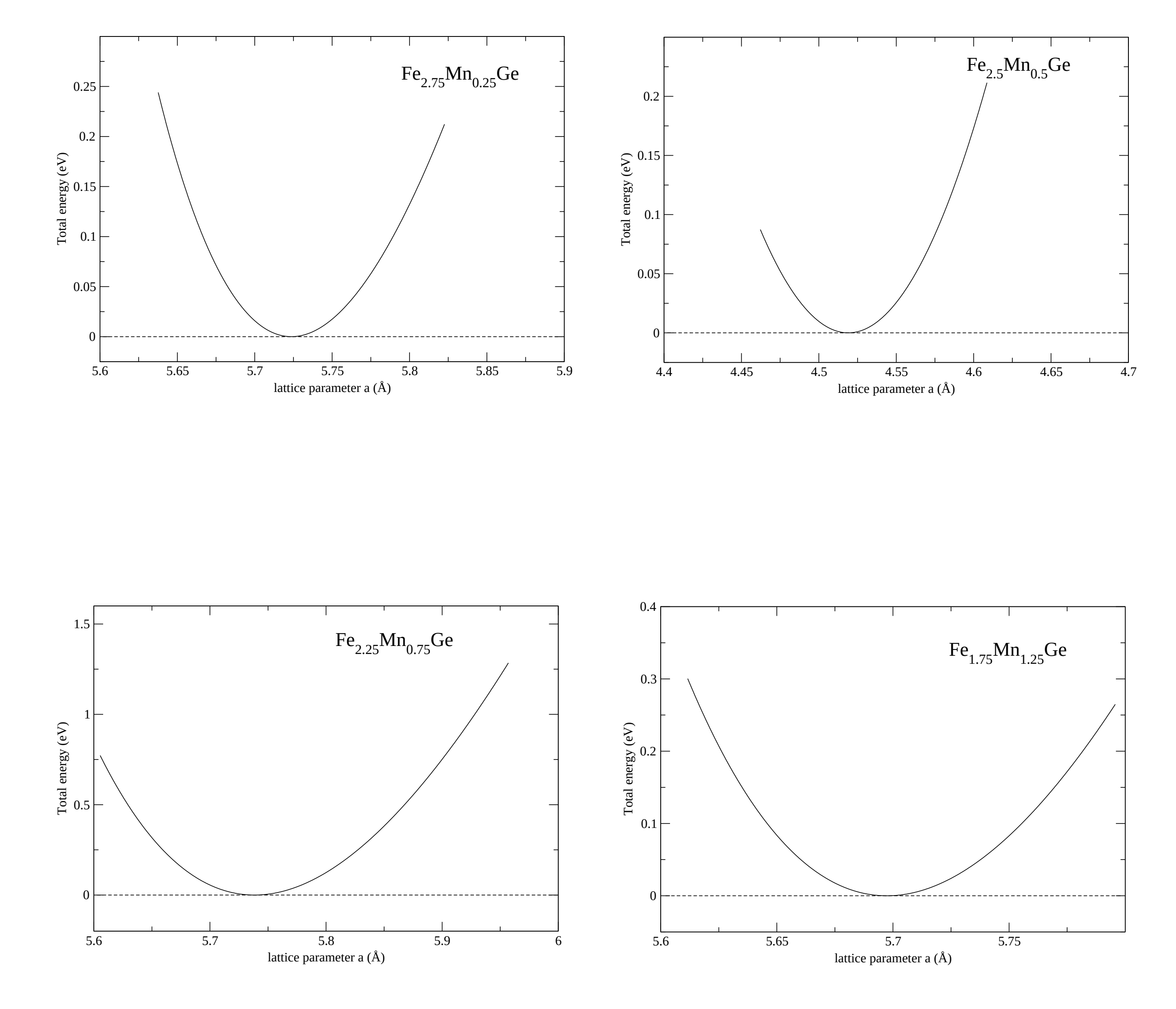


Figure 4.2.12. The energy versus the lattice parameter for non-stoichiometre $Fe_{3-x}Mn_xGe$.

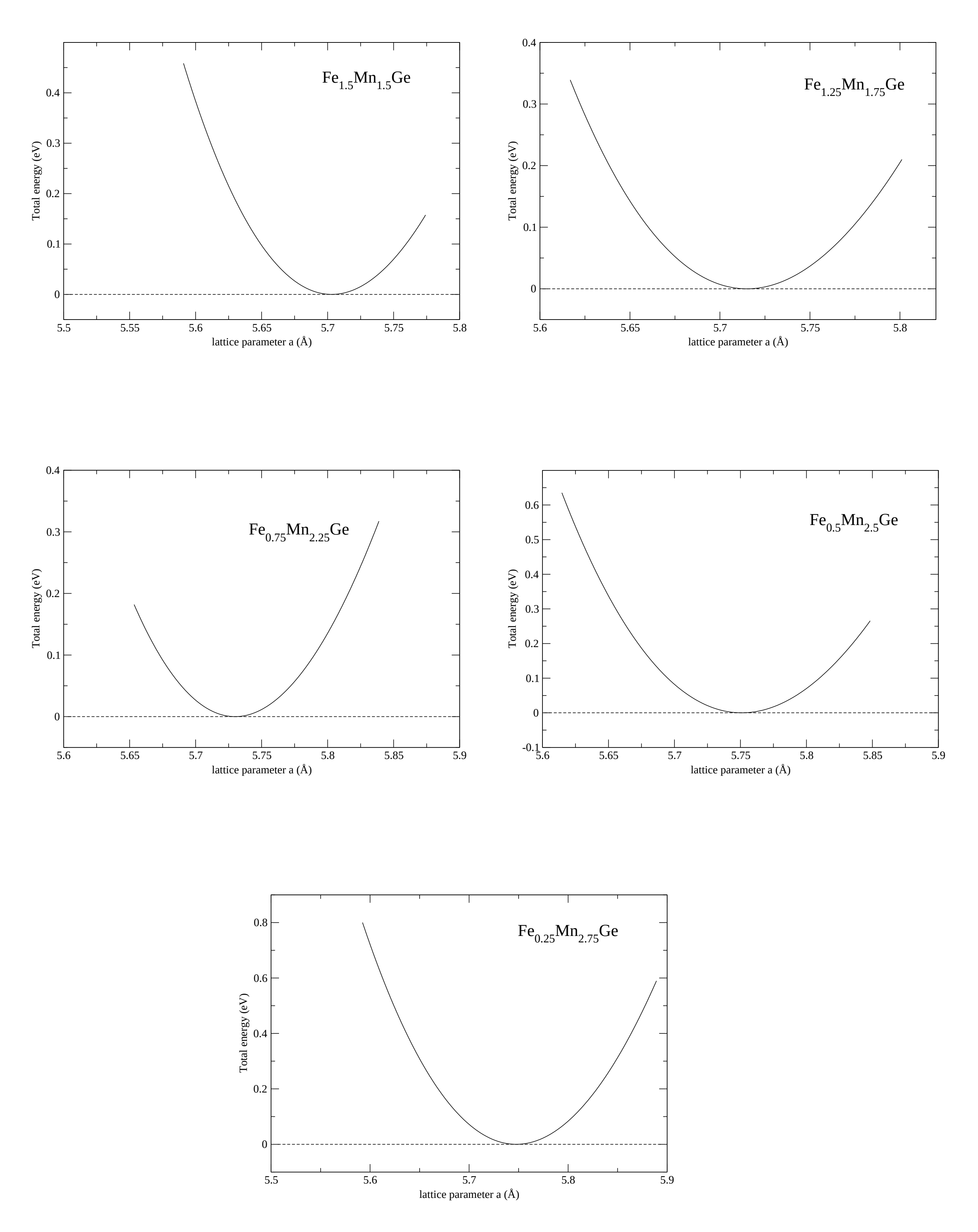


Figure 4.2.12 (continued)

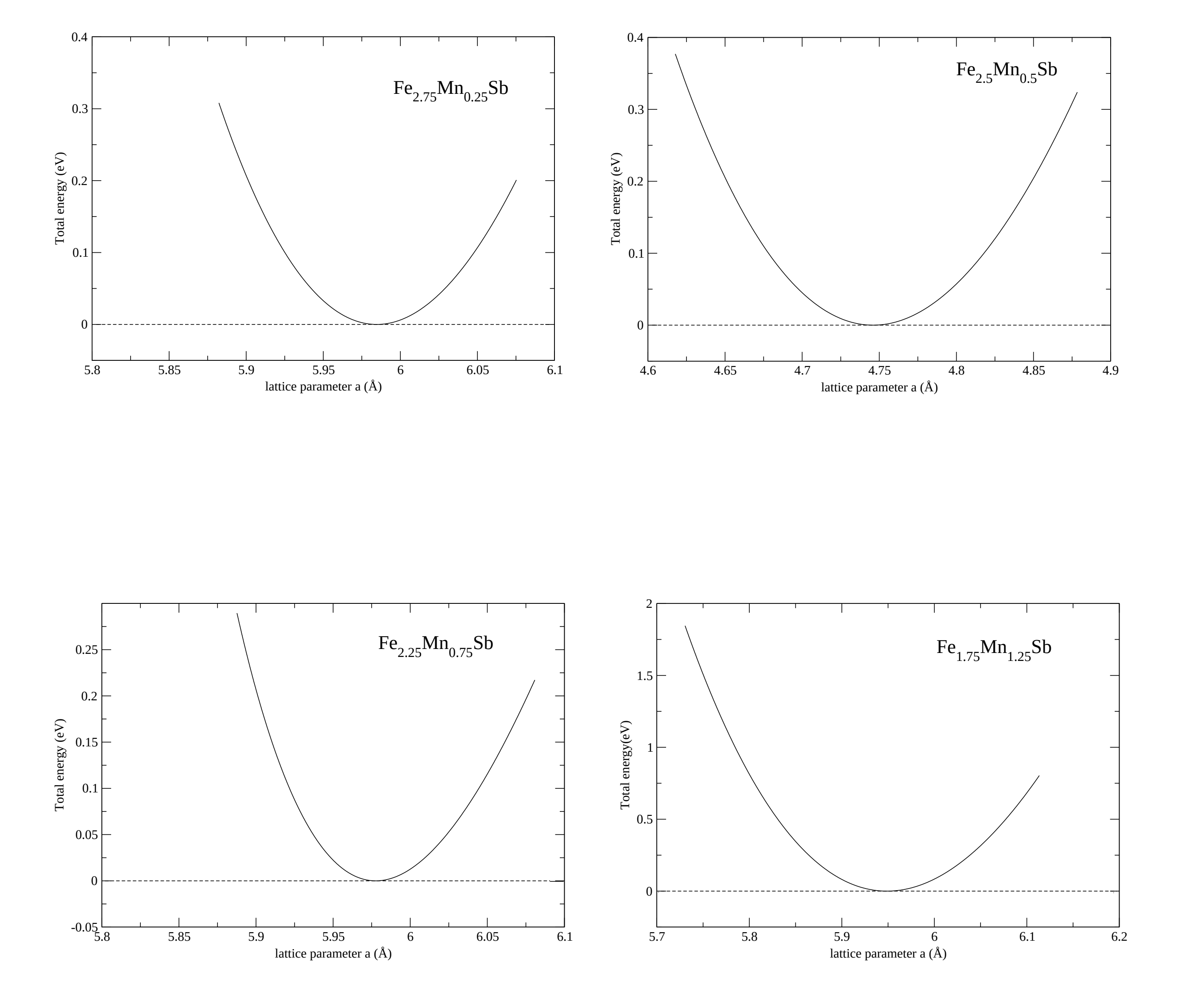


Figure 4.2.13. The energy versus the lattice parameter for non-stoichiometre $Fe_{3-x}Mn_xSb$.

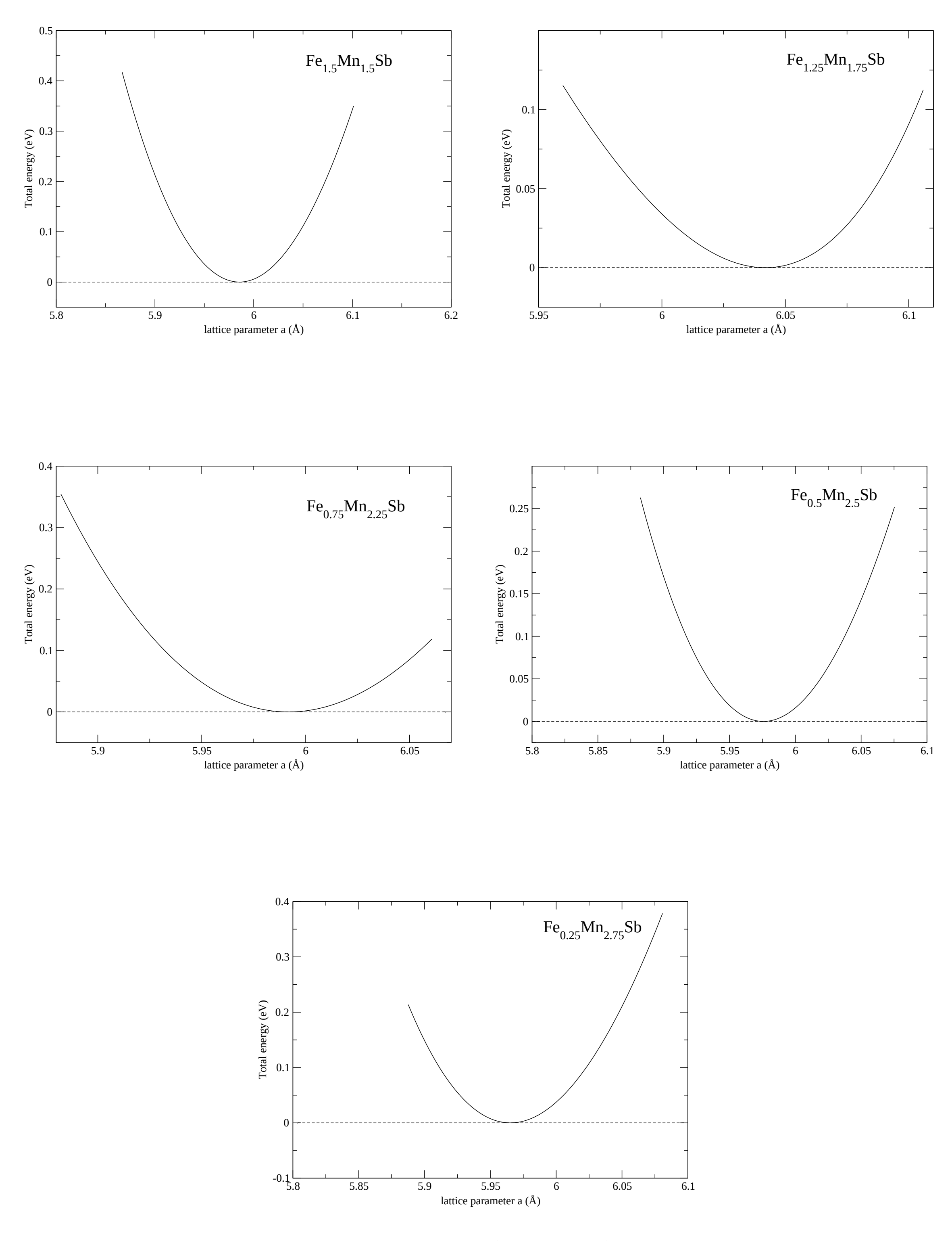


Figure 4.2.13 (continued)

4.2.2 Electronic Structure

The spin polarized total DOSs of $Fe_{3-x}Mn_xZ$ are shown in Figs. 4.2.14 to 4.2.16, where we can notice the shift in the majority spin channels towards higher energies in the conduction bands whereas the minority spin channel towards lower energies in the valence bands. The total DOS figures show that the DOS near E_F slightly varies in shape by partial replacement of constituent atoms. In other words, changes in the composition does not have a drastic effect on spin polarization. The spin polarization increases by increasing Mn concentration till it reaches 100 % as shown in Table 4.2.3. The majority DOS shows a very narrow peak at about -2.8 eV. These highly localized electrons also show up in the majority channel of the band structure as very flat bands through all high-symmetry points in the Brillouin zone. For x >1, the interaction between Mn and Fe atoms on the B sites cause Fe[A,C] DOS to undergoes quite substantial changes.

As we see in Table 4.2.3, the lattice parameter does not change linearly, i.e, does not obey Vegard's law, the spin polarization increases from 30% in $Fe_{2.75}Mn_{0.25}Al$ alloy to 100% in $Fe_{2.25}Mn_{0.75}Al$ alloy. The band gaps in the minority spin channels are found to be direct at Γ point, whereas for stoichiometric alloys, they exhibit an indirect band gap between Γ and X point.

The total spin polarized DOSs of $Fe_{3-x}Mn_xGe$ are shown in Fig. 4.2.15. The Mn impurity on B-site shows upward shift on the two peaks in the majority spin d band. By comparing the DOS for x=0.25 in Fig. 4.2.15 to the DOS for Fe_3Ge (DO_3 structure) in the preceding section, we see that it has the same shape. For intermediate compositions x, it is found that the Fe[B] DOS depends only weakly on the Ge content. The local Fe[D] DOS behaves somewhat similarly but exhibits a more pronounced dependence on x. This is the same for $Fe_{1.5}Mn_{1.5}Al$. For $Fe_{1.5}Mn_{1.5}Sb$ case, its stable structure is tetragonal instead of cubic. This distortion is the reason for the gap shift (see Fig. 4.2.16).

The replacement of Ge by Al or Sb is seen to induce only small changes in the shape of the minority spin DOS on either Fe and Mn. Although the calculations carried out for different structures, different magnetic alignment and ordered.

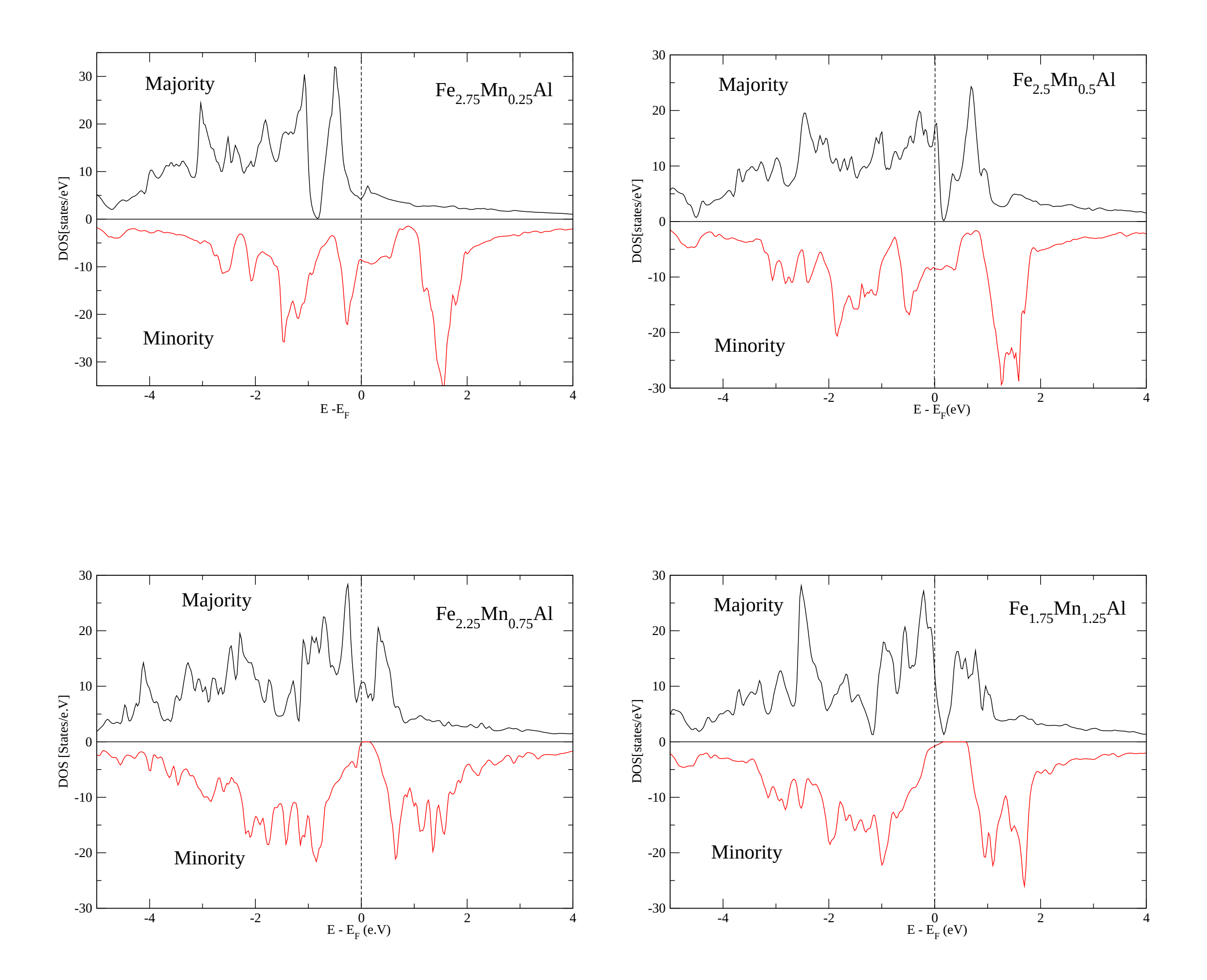


Figure 4.2.14. Total spin polarized DOS for non-stoichiometre $Fe_{3-x}Mn_xAl$.

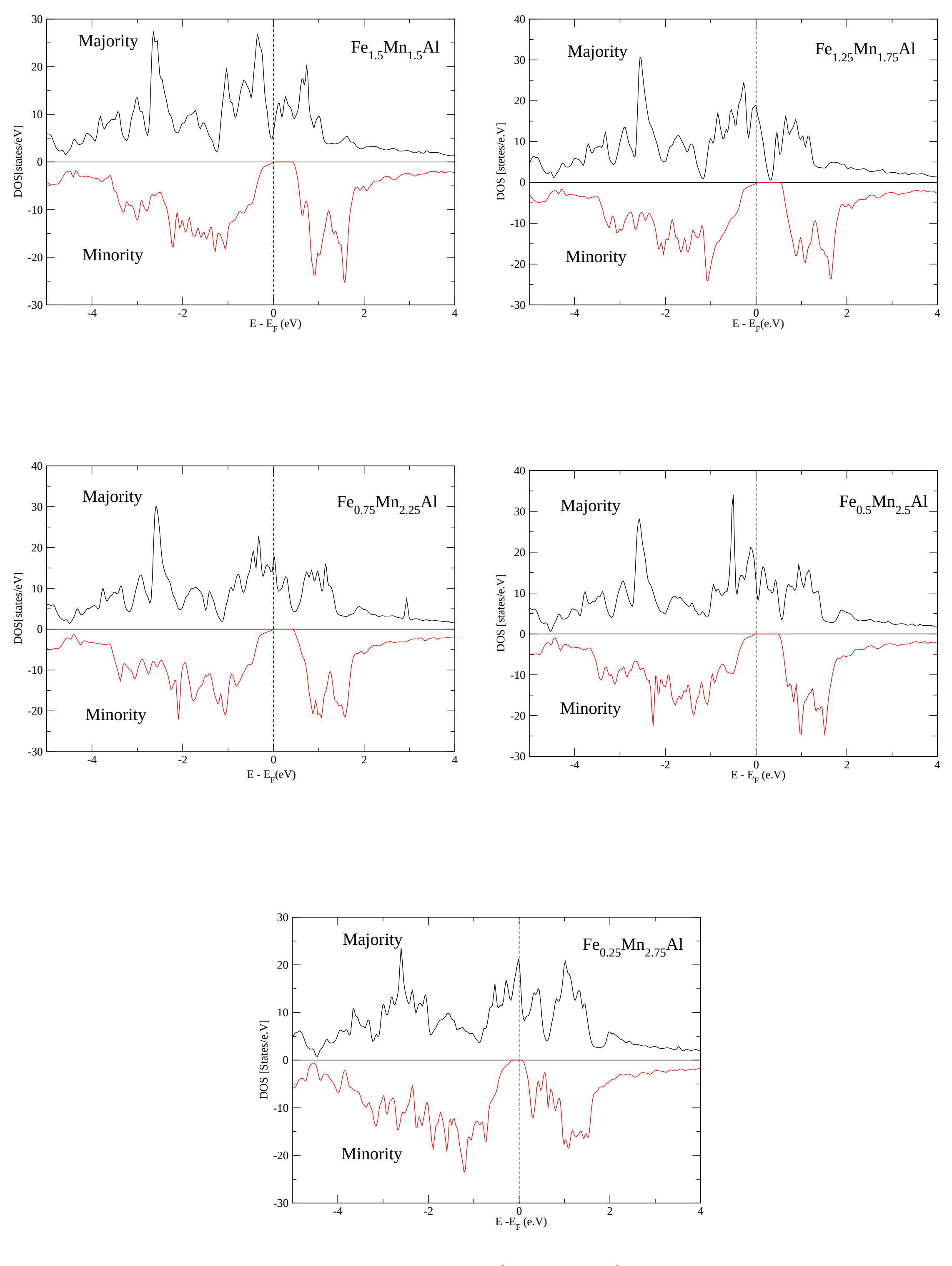


Figure 4.2.14 (continued)

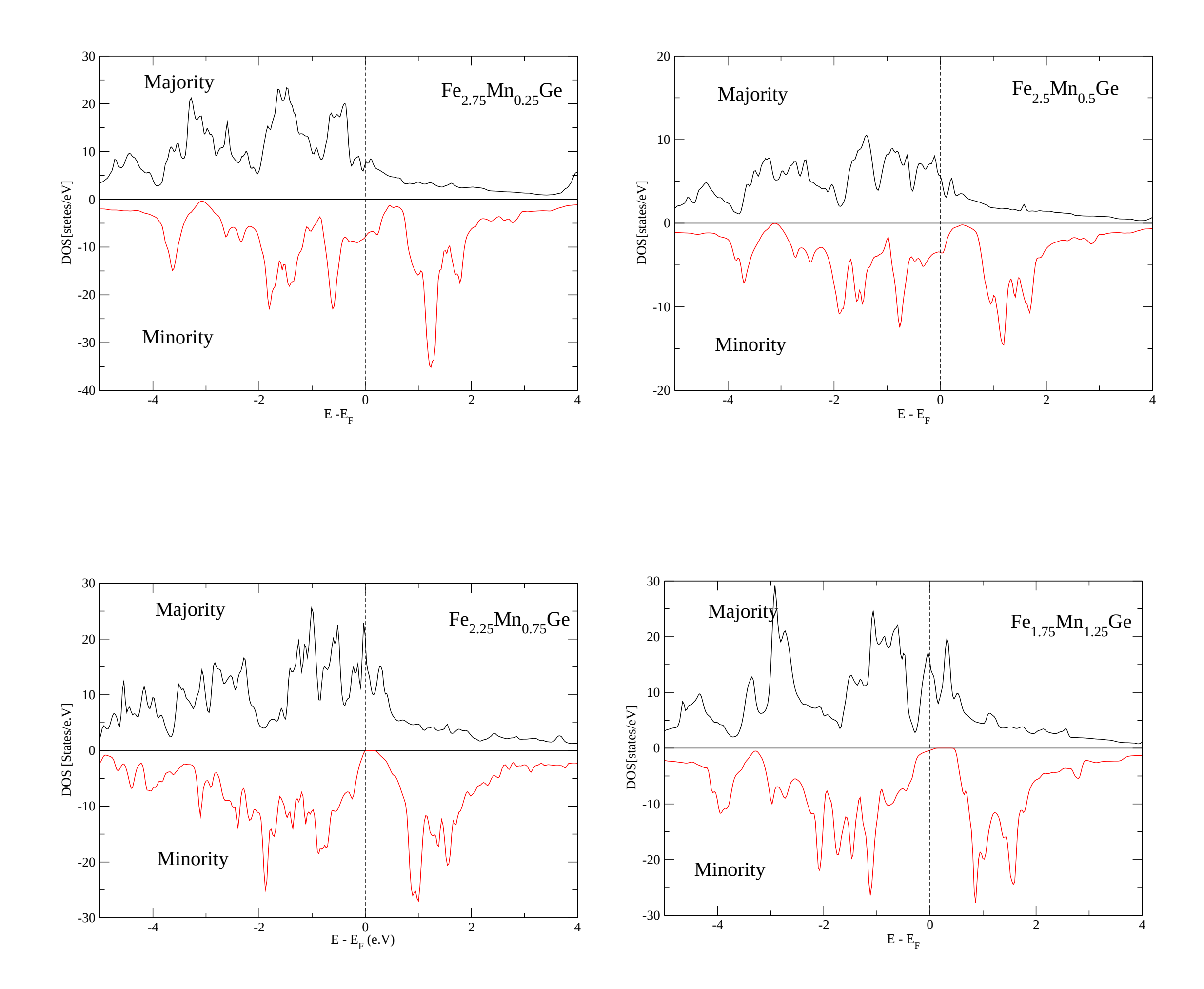


Figure 4.2.15. Total spin polarized DOS for non-Stoichiometre $Fe_{3-x}Mn_xGe$.

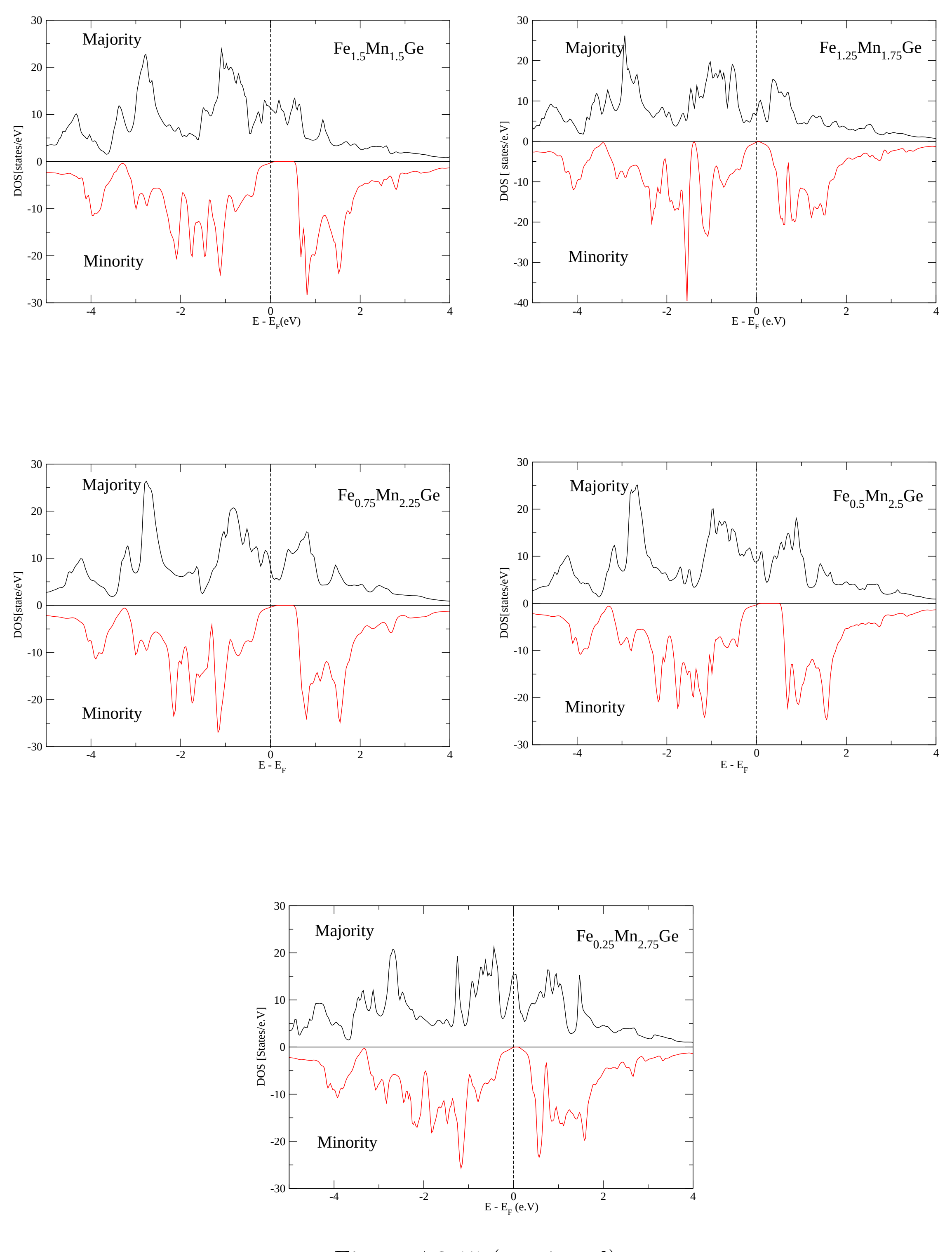


Figure 4.2.15 (continued)

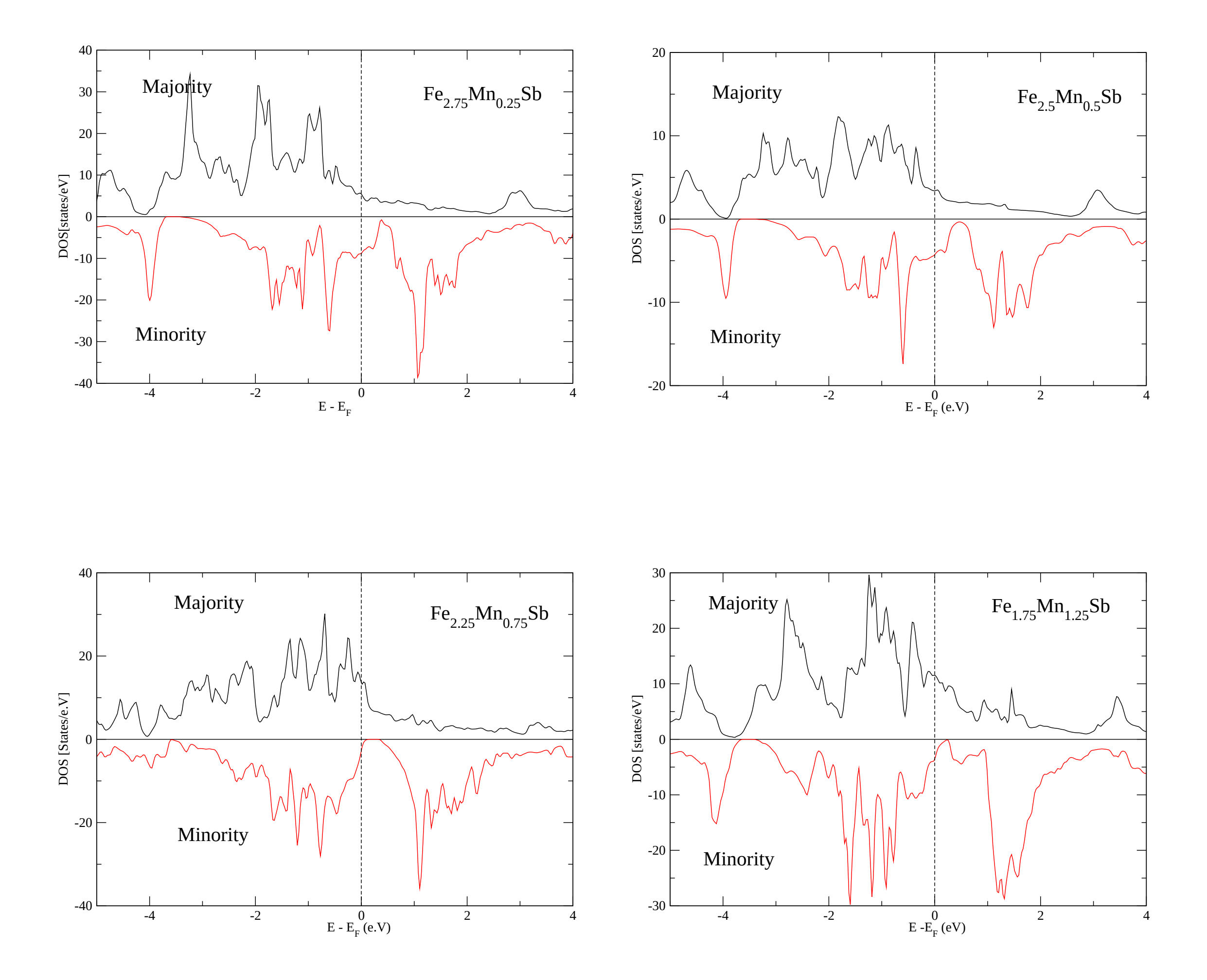


Figure 4.2.16. Total spin polarized DOS for non-Stoichiometre $Fe_{3-x}Mn_xSb$.

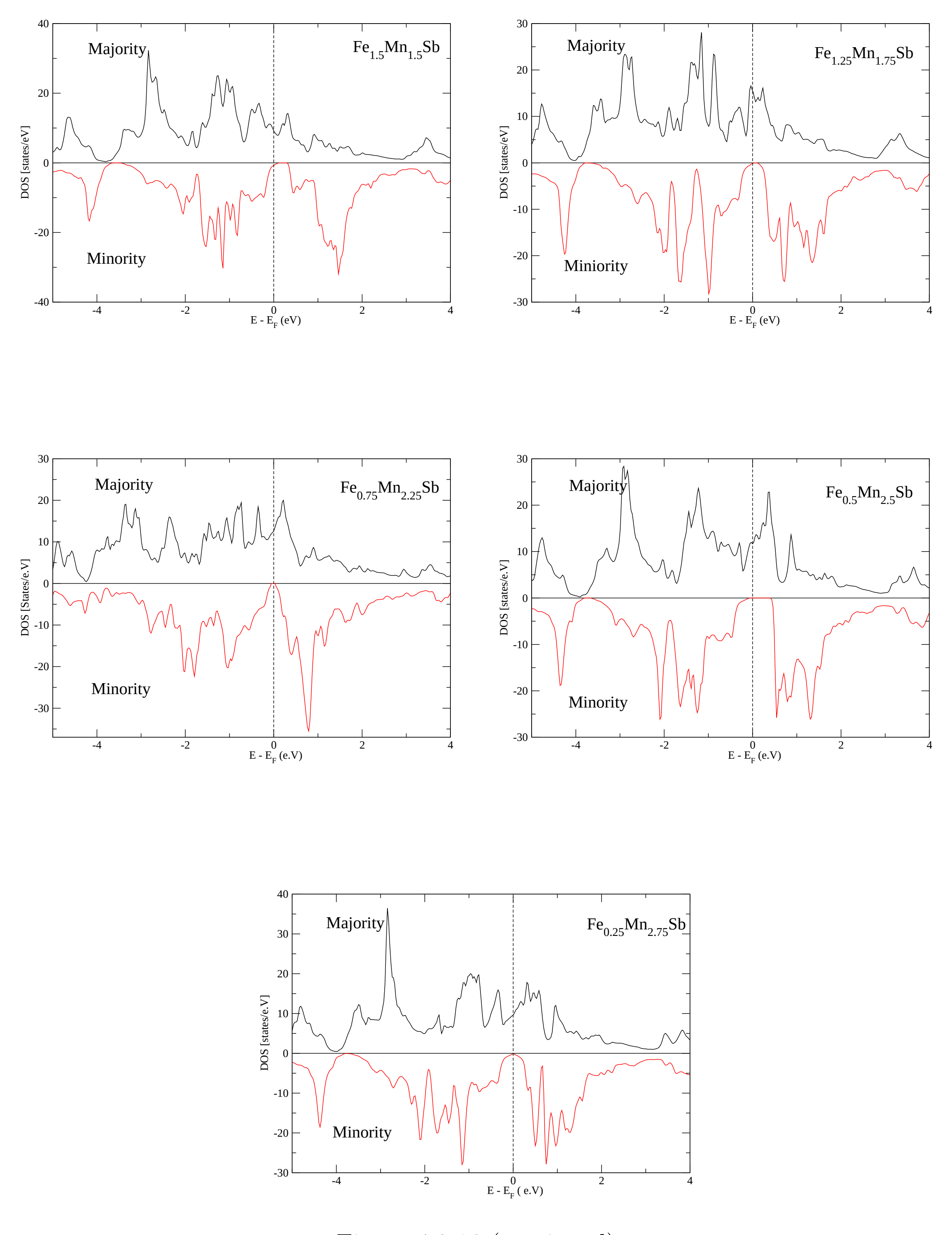


Figure 4.2.16 (continued)

4.2.3 Spin Magnetic Moments

The total and local spin magnetic moment for $Fe_{3-x}Mn_xZ$ are listed in Table 4.2.4. The variation of total magnetic moment with respect to Mn concentration is shown in Fig. 4.2.17. It is consistent with the generalized Slater-Pauling behavior, a modification of the original Slater-Pauling rule which takes into account the size of the cell in nonstoichiometric alloys, and has the form [Hülsen *et al.* 2009],

$$M_{tot} = N_\nu - 24n_Z \tag{4.3}$$

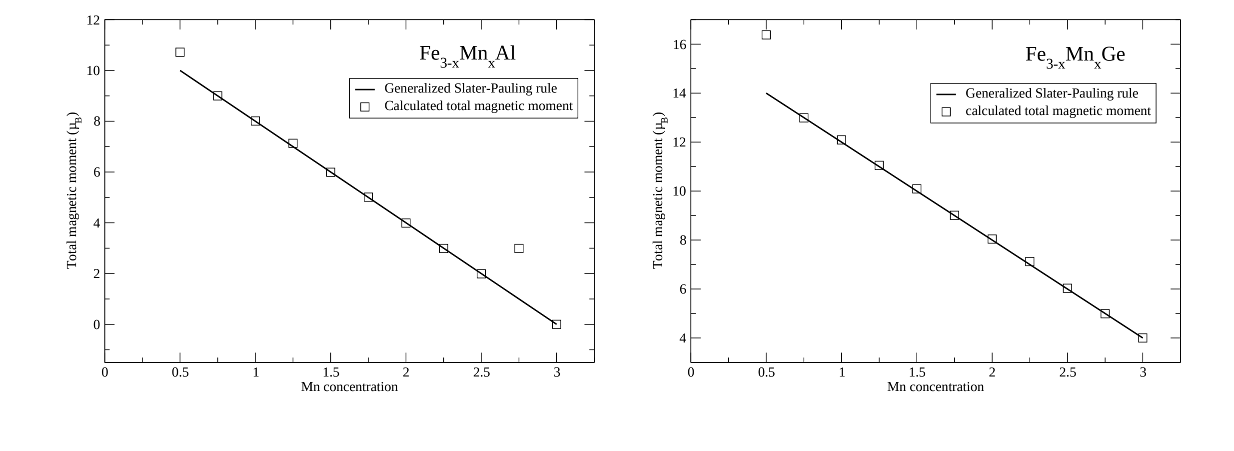
where n_Z is the number of metalloid atoms in each cell. The three compounds series begin to obey the generalized Slater-Pauling rule for x >0.5, except at x=2.75 in $Fe_{3-x}Mn_xAl$ compounds series which has a deviation because of its large spin magnetic moment located on Fe atom (1.42 μ_B). It is seen that the total magnetic moment per cell decreases as a function of Mn concentration, which caused by two reasons, first the decreasing of Fe[A,C] moments up to x=1. Secondly, the antiferromagnetic coupling of Mn[A,C] atoms for x >1. From x=0.25 to x=0.75, the dominant local spin magnetic moment is carried on Fe atom instead of Mn. It is increasing from 2.59 to 2.70, while for x=1.25 to 1.75 it is carried by Mn atom and it is decreasing from 2.61 to 2.47. Again it is increasing from 2.63 to 2.68 for x >2.25. The magnetic moment of Mn atoms are antiferomagnetically coupled with those of Fe at A and C sites and Mn at B sites.

If the Fermi energy is close to the band edges of the minority states, the high densities at those band edges may make the half-metallic behavior of the compound unstable at finite temperatures above 0 K. The Heusler alloys form an octahedrally coordinated half-metal with a relatively small exchange splitting and a narrow HM gap in the covelant octahedral structure.

The Mn-rich ordered compounds have highly symmetric structures that show a certain trend in the incorporation of the Mn at Fe sites. In Mn_2FeZ each second layer of Fe atoms is completely replaced by Mn atoms. When the manganese concentration increases, additional manganese atoms replace Fe in the remaining Fe sites. The general trend in the physics of alloys needs that stable structures have

relatively small and highly symmetric unit cells. The local orbital DOS reveals that the minority spin DOS of Mn atom at [A,C] sites is almost identical to the minority spin DOS of Fe. Furthermore, the magnetic moments of the Mn atoms at [A,C] sites. The generalized Slater-Pauling rule is valid for Mn-rich non-stoichiometric compounds. The linear relation between magnetic moments and Mn concentration, shown in Fig. 4.2.17 confirm this results.

It is found that the spin moment of Mn increases with the sequence of Al-Ge-Sb as the Z atoms are changed. However, the change of Fe spin moment is not so regular; it increases from Al to Ge, then decreases for Sb. The change in the magnetic moment may have several combined causes. First the change in lattice parameter, which may have an obvious influence on the magnetic properties. Second the different number of valence electrons of *sp* elements, where the *p* electrons of *sp* hybridize with the *d* states of Fe and Mn. Finally, the variation in Fe and Mn magnetic moments compensates each other and keeps the total magnetic moment as an integer.



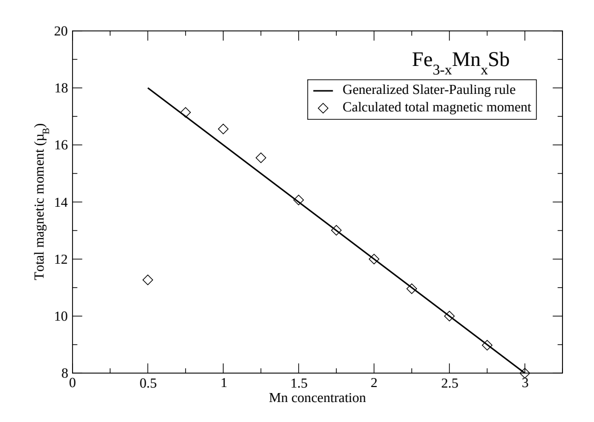


Figure 4.2.17. Slater-Pauling behavior and the calculated total magnetic moment of $Fe_{3-x}Mn_xZ$.

Table 4.2.4. Calculated total spin magnetic moments $M^{TOT}(\mu_B)$, the local magnetic moments $m(\mu_B)$ and the magnetic phase for the $Fe_{3-x}Mn_xZ$ (Z= Al,Ge,Sb) alloys series.

structure	$M^{TOT}(\mu_B)$	$m^a(\mu_B)$	$m^b(\mu_B)$	$m^c(\mu_B)$	$m^d(\mu_B)$	$m^{g,e1}(\mu_B)$	$m^{e2}(\mu_B)$	magnetic phase
Fe_3Al	23.86	1.927	2.422	–	-0.087	–	–	FM
$Fe_{2.75}Mn_{0.25}Al$	22.23	1.640^{Mn}	-0.09	2.410	-0.08	1.810		FM
$Fe_{2.5}Mn_{0.5}Al$	10.72	2.420	-0.07	-0.07	1.74^{Mn}		1.760	FM
$Fe_{2.25}Mn_{0.75}Al$	9.00	2.62	0.000	-0.013	2.39^{Mn}	-0.09		FM*
Fe_2MnAl	8.01	-0.152	2.32^{Mn}	–	-0.015			FM
$Fe_{1.75}Mn_{1.25}Al$	7.13	-0.04	-1.49^{Mn}	-0.04	-0.24	2.38^{Mn}	-0.01	FM*
$Fe_{1.5}Mn_{1.5}Al$	5.99	-1.66	2.429	-0.004	-0.07^{Fe}			FM
$Fe_{1.25}Mn_{1.75}Al$	5.01	0.200	-0.31	0.050	-1.71^{Mn}	0.00	2.54^{Mn}	FM*
$FeMn_2Al$	3.99	0.15^{Fe}	2.669	-1.798	-0.006	–	–	FM*
$Fe_{0.75}Mn_{2.25}Al$	2.99	-1.47	-1.64	0.30^{Fe}	-1.55	2.49	-0.002	FM*
$Fe_{0.5}Mn_{2.5}Al$	1.99	0.38^{Fe}	0.00	2.44	-1.41			FM*
$Fe_{0.25}Mn_{2.75}Al$	2.99	1.42^{Fe}	-0.011	-2.56	-0.005	1.16		FM*
Mn_3Al	0.000	-1.415	2.826		–	0.012	–	AF
Fe_3Ge	22.49	1.624	2.575	–	-0.057			FM
$Fe_{2.75}Mn_{0.25}Ge$	19.9	2.34^{Mn}	-0.04	2.59	-0.06	1.32		FM
$Fe_{2.5}Mn_{0.5}Ge$	8.19	2.61	-0.03	-0.03	2.26^{Mn}	0.88		FM
$Fe_{2.25}Mn_{0.75}Ge$	12.99	2.70	-0.02	-0.02	2.36^{Mn}	0.44		FM
Fe_2MnGe	12.09	0.209	2.626	–	-0.012	–	–	FM
$Fe_{1.75}Mn_{1.25}Ge$	11.05	0.30	-1.34^{Mn}	0.26	0.29	2.60^{Mn}	-0.004	FM*
$Fe_{1.5}Mn_{1.5}Ge$	10.09	-0.96	2.54	0.007	0.28^{Fe}			FM*
$Fe_{1.25}Mn_{1.75}Ge$	9.01	0.003	2.41^{Fe}	0.01	2.47	0.76^{Fe}	-0.98	FM*
$FeMn_2Ge$	8.05	0.506	2.562	-1.080	0.010	–	–	FM*
$Fe_{0.75}Mn_{2.25}Ge$	7.12	-0.83	-1.19	0.60^{Fe}	-1.14	2.63	0.02	FM*
$Fe_{0.5}Mn_{2.5}Ge$	6.03	0.59^{Fe}	-1.02	-1.02		0.03	2.68	FM*
$Fe_{0.25}Mn_{2.75}Ge$	4.99	2.47^{Fe}	0.03	2.66	0.04	-0.73		FM*
Mn_3Ge	4.00	-0.918	2.750	–	0.044	–	–	FM*
Fe_3Sb	24.46	1.789	2.730	–	-0.028	–	–	FM
$Fe_{2.75}Mn_{0.25}Sb$	23.83	2.83^{Mn}	-0.02	2.72	-0.04	1.69		FM
$Fe_{2.5}Mn_{0.5}Sb$	11.27	2.72	-0.04	-0.03	2.78^{Mn}		1.52	FM
$Fe_{2.25}Mn_{0.75}Sb$	17.14	3.04	-0.03	-0.02	2.90^{Mn}	0.74		FM
Fe_2MnSb	16.56	0.670	2.875	–	-0.02	–	–	FM
$Fe_{1.75}Mn_{1.25}Sb$	15.55	1.27	-2.01^{Mn}	0.76	1.03	2.79^{Mn}	-0.01	FM*
$Fe_{1.5}Mn_{1.5}Sb$	14.07	-1.46	2.78	-0.003	0.96^{Fe}			FM*
$Fe_{1.25}Mn_{1.75}Sb$	13.01	0.02	2.81^{Fe}	0.02	2.92	1.29^{Fe}	-0.94	FM*
$FeMn_2Sb$	12.00	1.164	2.948	-1.141	0.017	–	–	FM*
$Fe_{0.75}Mn_{2.25}Sb$	10.96	3.05	0.02	0.03	2.65^{Fe}	0.04		FM*
$Fe_{0.5}Mn_{2.5}Sb$	10.00	0.91^{Fe}	0.02	2.91	-0.62			FM*
$Fe_{0.25}Mn_{2.75}Sb$	8.98	2.70^{Fe}	0.023	2.78	0.025	-0.29		FM*
Mn_3Sb	8.00	-0.472	2.856	–	0.028	–		FM*

FM: Ferromagnetic FM*: Ferrimagnetic AF: Antiferromagnetic

4.2.4 Hyperfine Field (HFF)

Hyperfine field (HFF) on an atomic nucleus can be defined as B_{hf}= B_c+B_{dip}+B_{orb}+B_{lat}, where the first term B_c is the Fermi contact contribution that stems from the spin magnetic moment of the electrons, B_{dip} is the dipolar field from the on-site spin density, B_{orb} is the field associated with the on-site

orbital moment and B_{lat} is classical dipolar field from all other atoms in the system that carry magnetic moment. Using scalar-relativistic approximation with cubic symmetry of the crystal, the last three terms vanish or they are relatively small. As a consequence, in calculating the hyperfine fields of magnetic solids normally only the Fermi contact term is considered which is written in the expression as [Watson and Freeman 1961]

$$B_c = n\mu_B\chi \tag{4.4}$$

$$\chi = (4\pi/n)\sum\{\rho_\uparrow(0) - \rho_\downarrow(0)\} \tag{4.5}$$

where n is the number of unpaired electrons, and $\rho_\uparrow(0)$ ($\rho_\downarrow(0)$) is the density of s electrons at the nucleus for majority (minority) spin. Calculation of B_c is performed in standard spin-polarized WIEN2k calculation.

It is found that the magnetic hyperfine fields on the metalloid atoms Z increase with increasing the Mn concentration as shown in Fig. 4.2.18. Likewise, the calculated hyperfine fields on the B-site decrease in magnitude with increasing Mn concentration for all series compounds as shown in Fig. 4.2.19. Also, the Mn hyperfine field B_{hf}(Mn) in B-site is linearly related to the Mn magnetic moment, while the Fe hyperfine fields B_{hf}(Fe) in A-,C-site are not proportional to the Fe magnetic moment, but decrease with increasing valence electrons of the atom Z. Our calculated hyperfine fields of Fe[A, C] and Fe[B] sites for Fe_3Al are -254 and 299 kG, respectively, whereas the measured hyperfine fields of Fe[A, C] and Fe[B] sites are -215 and 290 kG, respectively (see ref. [Lakshmi *et al.* 1993]). Although Fe[B] has the same number of first-nearest neighbors as that of bulk Fe, the observed (290 kG) and predicted (299 kG) hyperfine fields at this site are different from that of bulk Fe ($\sim$ 330 kG). This is due to the presence of *sp* atoms in the second-nearest neighboring positions, which reduces the overall field at the Fe[B] site.

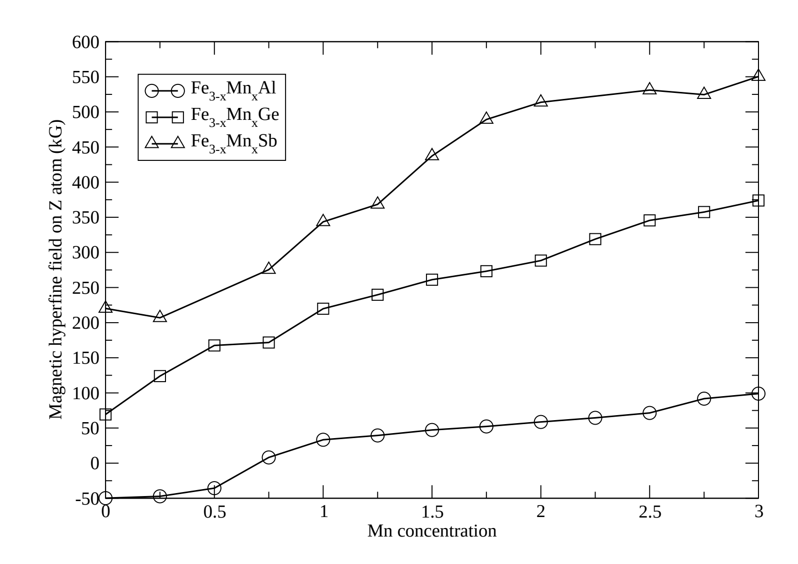


Figure 4.2.18. The calculated magnetic hyperfine field on Z atoms with different Mn concentration of the series $Fe_{3-x}Mn_xZ$(Z = Al, Ge, Sb).

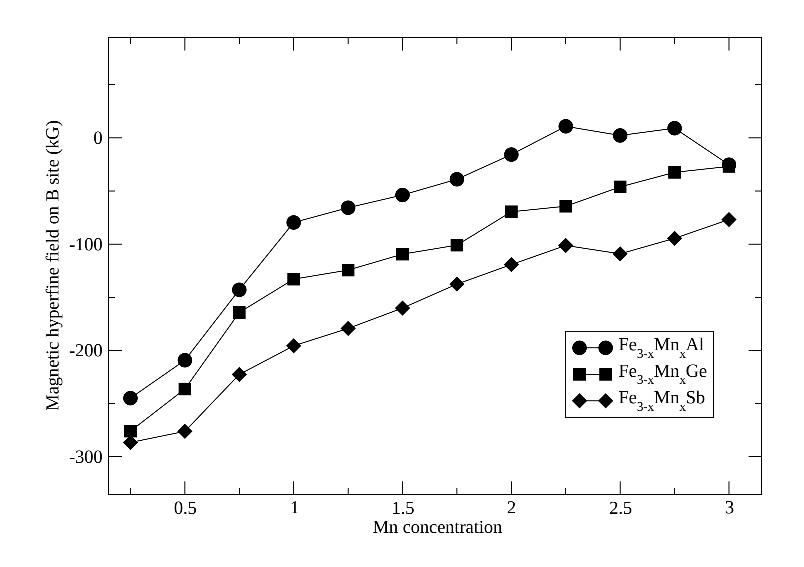


Figure 4.2.19. The calculated hyperfine field on the B-site with different Mn concentration of the series $Fe_{3-x}Mn_xZ$(Z = Al, Ge, Sb).

CHAPTER 5

CONCLUSION

5.1 Conclusions

In this contribution, an extensive first-principle electronic structure computations on $Fe_{3-x}Mn_xZ$ over the entire composition range for three different metalloids Z, namely, Al, Ge, and Sb are reported. We considered the parent systems Fe_3Z for which $x = 0$. By choosing Z=Al or Z=Sb the effect of replacing Ge by either Al or Sb is studied, and by varying x the entire composition range of stoichiometric and non-stoichiometric alloys is covered.

It is found that the Fe rich compounds are metallic and have low spin polarization, when the Mn concentration is increasing the alloys exhibit highly spin polarization. The substitutions of metalloid atoms produce similar DOSs and are not responsible for the origin of the band gap since all compounds have gaps near the Fermi levels, but lead to a shift in the Fermi level; thus the change of metalloid atoms can destroy the half-metallicity. Notably, the DOS of $Fe_{3-x}Mn_xZ$ develops gap or pseudogap for minority spin states around the Fermi energy in the Mn-rich regime, which may play a role in the anomalous behavior of the transport properties. Compounds beyond x >0.75 are strong candidates as half-metals with high spin polarization. The band gaps where found to be direct except for the stoichiometric one, which exhibit indirect band gaps along Γ - X symmetry line. We conclude that the existence of the gap is directly related to the occurrence of X_2 and mixed YZ (001)-planes and that the $L2_1$ phase is not the only possibility for the presence of a HM gap in Heusler alloys. It is delineated clearly how the electronic states and magnetic moments at various sites in $Fe_{3-x}Mn_xZ$ evolve as a function of the Mn content and the metalloid valence.

In summary, it is shown that the variation of the main group element (Al, Ge, Sb, etc.) in Heusler compounds is a strong tool in order to tune their physical properties. The electronic structures of these alloys predict that the high spin polarization is preserved against partial replacement of constituent atoms. Further that, the hyperfine field on both Fe and Mn atoms are decreasing with increasing the Mn concentration.These results are of particular interest to experimentalists searching for new half-metallic materials for spintronic devices.

Finally, since Heusler alloys at the present stage are considered highly defective materials, much work remain to be done in the field of point defects. A comprehensive investigation focused on the whole class of Heusler compound is needed to elucidate the mechanisms that result in losing or keeping the half-metallicity and to determine if the Heusler alloys may be used as basic spintronic materials in the future.

5.2 Open Issues

In this section, several open issues are summarized which can be a subject of future work as follows:

1. Investigation of the effect of disorder on the electric and magnetic properties of $Fe_{3-x}Mn_xZ$ compounds.

2. The optical properties of the $Fe_{3-x}Mn_xZ$ Heusler alloys.

3. Elastic properties and magnetic shape memory alloy for $Fe_{3-x}Mn_xZ$.

4. The transport properties and half-metallicity at elevated temperature of $Fe_{3-x}Mn_xZ$ compounds.

5. The effect of lowering the dimension of $Fe_{3-x}Mn_xZ$ compounds may be studied.
   (surfaces and interfaces)

6. The electronic and magnetic properties of $Mn_2FeAl_{1-x}Ge_x$ quaternary Heusler alloys could be investigated.

7. The half-metallicity search in $Ti_{1+x}FeSb$ Heusler alloys (x= 0, 0.25, 0.5, 0.75, 1).

REFERENCES

[Abragam 1961] A. Abragam. **The principles of nuclear magnetism**. Clarendon, Oxford, 1961.

[Acet *et al.* 2002] M. Acet, E. Duman, E. F. Wassermann, L. Manosa and A. Planes. Coexisting ferro- and antiferromagnetism in Ni_2MnAl Heusler alloys. **J. Appl. Phys.**, vol. 92, page 3867, 2002.

[Akai 1998] H. Akai. Ferromagnetism and Its Stability in the Diluted Magnetic Semiconductor (In, Mn)As. **Phys. Rev. Lett.**, vol. 81, page 3002, 1998.

[Andersen 1975] O. Krogh Andersen. Linear methods in band theory. **Phys. Rev. B**, vol. 12, no. 8, page 3060, 1975.

[Bandyopadhyay 2000] S. Bandyopadhyay. Self-assembled nanoelectronic quantum computer based on the Rashba effect in quantum dots. **Phys. Rev. B**, vol. 61, page 13813, 2000.

[Bansal *et al.* 1994] C. Bansal, Z. Q. Gao, L. B. Hong and B. Fultz. Phases and phase stabilities of Fe_3X alloys (X=Al, As, Ge, In, Sb, Si, Sn, Zn) prepared by mechanical alloying. **J. Appl. Phys.**, vol. 76, page 5961, 1994.

[Blaha *et al.* 1990] P. Blaha, K. Schwarz, P. Sorantin and S. B. Trickey. Full-potential, linearized augmented plane wave programs for crystalline systems. **Comp. Phys. Commun.**, vol. 59, page 399, 1990.

[Blöchl *et al.* 1994] Peter E. Blöchl, O. Jepsen and O. K. Andersen. Improved tetrahedron method for Brillouin-zone integrations. **Phys. Rev. B**, vol. 49, no. 23, pages 16223, 1994.

[Bona *et al.* 1985] G. L. Bona, F. Meier, M. Taborelli, E. Bucher and P. H. Schmidt. Spin polarized photoemission from NiMnSb. **Solid State Commun.**, vol. 56, page 391, 1985.

[Borwn *et al.* 2000] P. J. Borwn, K. U. Neumann, P. J. Webster and K. R. A. Ziebeck. The magnetization distributions in some Heusler alloys proposed as half-metallic ferromagnets. **J. Phys.:Condens. Matter**, vol. 12, page 1827, 2000.

[Bross 1964] H. Bross. **Phys. Kondens. Mater**, vol. 3, page 119, 1964.

[Bross *et al.* 1970] H. Bross, G. Bohn, G. Meister, W. Schubö and H. Stöhr. New Version of the Modified Augmented-Plane-Wave Method. **Phys. Rev. B**, vol. 2, page 3098, 1970.

[Buschow and van Engen 1981] K. H. J. Buschow and P. G. van Engen. Magnetic and magneto-optical properties of heusler alloys based on aluminium and gallium. **J. Magn. Magn. Mater.**, vol. 25, page 90, 1981.

[Caballero *et al.* 1998] J. A. Caballero, Y. D. Park, J. R. Childress, J. Bass, W. C. Chiang, A. C. Reilly, W. P. Partt and F. Petroff. Magnetoresistance of NiMnSb-based multilayers and spin valves. **J. Vac. Sci. Technol. A**, vol. 16, page 1801, 1998.

[Camphausen *et al.* 1972] D. L. Camphausen, J. M. D. Coey and B. K. Chakraverty. One-Electron Energy Levels in Fe_3O_4. **Phys. Rev. Lett.**, vol. 29, page 657, 1972.

[Chioncel *et al.* 2003] L. Chioncel, M. I. Katsnelson, R. A. de Groot and A. I. Lichtenstein. Nonquasiparticle states in the half-metallic ferromagnet NiMnSb. **Phys. Rev. B**, vol. 68, page 144425, 2003.

[Chioncel *et al.* 2006] L. Chioncel, E. Arrigoni, M. I. Katsnelson and A. I. Lichtenstein. Electron Correlations and the Minority-Spin Band Gap in Half-Metallic Heusler Alloys. **Phys. Rev. Lett.**, vol. 96, page 137203, 2006.

[Coey *et al.* 2002] J. M. D. Coey, M. Venkatesan and M. A. Bari. Half-metallic ferromagnets **lecture notes in physics**, volume 595. Berlin :Springer, 2002.

[Datta and Das 1990] S. Datta and B. Das. Electronic analog of the electrooptic modulator. **Appl. Phys. Lett.**, vol. 56, page 665, 1990.

[de Groot *et al.* 1983] R. A. de Groot, F. M. Mueller, P. G. van Engen and K. H. J. Buschow. New Class of Materials: Half-Metallic Ferromagnets. **Phys. Rev. Lett.**, vol. 50, page 2024, 1983.

[de Groot and Buschow 1986] R. A. de Groot and K. H. J. Buschow. Recent Developments in half-metallic magnetism. J. Magn. Magn. Mater., vol. 54-57, page 1377, 1986.

[de Wijs and de Groot 2001] G. A. de Wijs and R. A. de Groot. Towards 100% spin-polarized charge-injection: The half-metallic NiMnSb/CdS interface. **Phys. Rev. B**, vol. 64, no. 2, page 020402, 2001.

[Deijver *et al.* 1976] J. W. Deijver, S. G. Sinnema and F. van der Woude. Magnetic properties of hexagonal and cubic Fe_3Ge. **J. Phys. F: Met. Phys.**, vol. 6, no. 11, page 2165, 1976.

[Dowben and Skomski 2003] P. A. Dowben and R. Skomski. Finite-temperature spin polarization in half-metallic ferromagnets. **J. Appl. Phys.**, vol. 93, page 7948, 2003.

[Ebert and Schutz 1991] H. Ebert and G. Schutz. Theoretical and experimental study of the electronic structure of PtMnSb. **J. Appl. Phys.**, vol. 69, page 4627, 1991.

[Fang *et al.* 2002] C. M. Fang, G. A. de Wijs and R. A. de Groot. Spin-polarization in half-metals (invited). **J. Appl. Phys.**, vol. 91, page 8340, 2002.

[Fermi 1926] E. Fermi. Zur Quantelung des Idealen Einatomigen Gases. **Z. Phys.**, vol. 36, page 902, 1926.

[Fesher *et al.* 2006] G. H. Fesher, H. C. Kandpal, S. Wurmehl, C. Felser and G. Schonhense. Slater-Pauling rule and Curie temperature of Co_2-based Heusler compounds. **J. Appl. Phys.**, vol. 99, page 08J106, 2006.

[Fock 1930] V. Fock. Näherungsmethode zur Lösung des quan- tenmechanischen Mehrkörperproblems. **Z. Phys.**, vol. 61, page 126, 1930.

[Fruchart *et al.* 1988] D. Fruchart, R. Fruchart, Ph. L'Héritier, K. Kanematsu, P. J. Webster and K. R. A. Ziebeck. Magnetic properties of metals: Alloys and compounds of d-elements with main group elements. part 2, volume 19C of **Landolt-Börnstein new series group III**. Berlin :Springer, 1988.

[Fujii *et al.* 1995] S. Fujii, S. Ishida and S. Asano. A Half-Metallic Band Structure and Fe_2MnZ (Z=Al, Si, P). **J. Phys. Soc. Jpn.**, vol. 64, no. 1, page 185, 1995.

[Fujii *et al.* 2008] S. Fujii, M. Okada, S. Ishida and S. Asano. High Spin Polarizaion of Ferrimagnetic Heusler-type Alloys in Mn–Cr–Z System (Z = IIIb, IVb, Vb Elements). **J. Phys. Soc. Jpn.**, vol. 77, no. 7, page 074702, 2008.

[Fujita *et al.* 2004] A. Fujita, K. Fukamichi, F. Gejima, R. Kainuma and K. Ishida. Magnetic properties and large magnetic-field-induced strains in off-stoichiometric Ni–Mn–Al Heusler alloys. **Appl. Phys. Lett.**, vol. 77, page 3054, 2004.

[Galanakis 2002a] I. Galanakis. Surface half-metallicity of CrAs in the zinc-blende structure. **Phys. Rev. B**, vol. 66, page 012406, 2002.

[Galanakis *et al.* 2002b] I. Galanakis, P. H. Dederichs and N. Papanikolaou. Origin and properties of the gap in the half-ferromagnetic Heusler alloys. **Phys. Rev. B**, vol. 66, no. 13, page 134428, 2002.

[Galanakis *et al.* 2002c] I. Galanakis, P. H. Dederichs and N. Papanikolaou. Slater-Pauling behavior and the origin of the half-metallicity of the full-Heusler alloys. **Phys. Rev. B**, vol. 66, page 174429, 2002.

[Galanakis 2003a] I. Galanakis. Surface properties of the half-and full-Heusler alloys. **J. Phys.:Condens. Matter**, vol. 14, page 6329, 2003.

[Galanakis nd Mavropoulos 2003b] I. Galanakis and P. Mavropoulos. Zinc-blende compounds of transition elements with N, P, As, Sb, S, Se, and Te as half-metallic systems. **Phys. Rev. B**, vol. 67, page 104417, 2003.

[Galanakis 2004] I. Galanakis. Appearance of half-metallicity in the quaternary Heusler alloys. **J. Phys.:Condens. Matter**, vol. 16, page 3089, 2004.

[Galanakis 2005] I. Galanakis. Orbital magnetism in the half-metallic Heusler alloys. **Phys. Rev. B**, vol. 71, page 012413, 2005.

[Gebauer 2010] Ralph Gebauer. Privite communications, 2010.

[Goodenough 1971] J. B. Goodenough. Metallic oxides. **Prog. Solid State Chem.**, vol. 5, page 145, 1971.

[Gori-Giorgi *et al.* 2000] P. Gori-Giorgi, F. Sacchetti and G. B. Bachelet. Analytic structure factors and pair correlation functions for the unpolarized electron gas. **Phys. Rev. B**, vol. 61, page 7353, 2000.

[Hamad *et al.* 2010] B. A. Hamad, J. M. Khalifeh, I. A. Aljarayesh, C. Demangeat, H. B. Luo and Q. M. Hu. The Electronic Structure and Spin Polarization of $Fe_{3-x}Mn_xSi$ and $Fe_{3-y}MnSi_y$ Alloys. **J. Appl. Phys.**, vol. 107, page 093911, 2010.

[Hamad *et al.* 2011] B. A. Hamad, J. M. Khalifeh, Q. M. Hu and C. Demangeat. Electronic and magnetic properties of $Fe_{3-x}Cr_xSi$ ordered alloys from first principles. **J. Materials Science**, 2011 accepted.

[Hamann 1979] D. R. Hamann. Semiconductor Charge Densities with Hard-Core and Soft-Core Pseudopotentials. **Phys. Rev. Lett.**, vol. 42, page 662, 1979.

[Hamann *et al.* 1981] D. R. Hamann, L. F. Mattheiss and H. S. Greenside. Comparative LCAO-LAPW study of C1 chemisorption on the Ag(001) surface. **Phys. Rev. B**, vol. 24, page 6151, 1981.

[Hanssen *et al.* 1990] K. E. H. M. Hanssen, P. E. Mijnarends, L. P. L. M. Rabou and K. H. J. Buschow. Positron-annihilation study of the half-metallic ferromagnet NiMnSb: Experiment. **Phys. Rev. B**, vol. 42, page 1533, 1990.

[Hartree 1928] D. R Hartree. The Wave Mechanics of an Atom with a Non-Coulomb Central Field. Part I. Theory and Methods. **Proc. Campridge Philos. Soc.**, vol. 24, page 426, 1928.

[Helmholdt *et al.* 1984] R. B. Helmholdt, R. A. de Groot, F. M. Mueller, G. P. van Engen and K. H. J. Buschow. Magnetic and crystallographic properties of several $C1_b$ type Heusler compounds. **J. Magn. Magn. Mater.**, vol. 43, page 249, 1984.

[Herman *et al.* 1969] F. Herman, J.P. Van Dyke and I.P. Ortenburger. Improved statistical exchange approximation for inhomogeneous many-electron systems. **Phys. Rev. Lett.**, vol. 22, page 807, 1969.

[Heusler 1903] F. Heusler. Heusler. **Verh. Dtsch. Phys. Ges.**, vol. 5, page 219, 1903.

[Hohenberg and Kohn 1964] P. Hohenberg and W. Kohn. In Homogeneous Electron Gas. **Phys. Rev. B**, vol. 136, page 864, 1964.

[Hordequin *et al.* 1998] C. Hordequin, J. P. Noziéres and J. Pierre. Half metallic NiMnSb-based spin-valve structures. **J. Magn. Magn. Mater.**, vol. 183, page 225, 1998.

[Horne *et al.* 2004] M. Horne, P. Strange, W. M. Temmerman, Z. Szotek, A. Svane and H. Winter. The electronic structure of europium chalcogenides and pnictides. **J. Phys.:Condens. Matter**, vol. 16, page 5061, 2004.

[Hülsen *et al.* 2009] B. Hülsen, M. Scheffler and P. Kratzer. Thermodynamics of the Heusler alloy $Co_{2-x}Mn_{1+x}Si$: a combined density functional theory and cluster expansion study. **Phys. Rev. B**, vol. 79, page 094407, 2009.

[Irkhin and Katstelson 1990] V Yu Irkhin and M I Katsnelson. Ground state and electron-magnon interaction in an itinerant ferromagnet: half-metallic ferromagnets. **J. Phys.: Condens Matter**, vol. 2, no. 34, page 7151, 1990.

[Irkhin and Katsnelson 2002] V Yu Irkhin and M. I. Katsnelson. Temperature dependences of resistivity and magnetoresistivity for half-metallic ferromagnets. **Eur. Phys. J. B**, vol. 30, page 481, 2002.

[Ishida *et al.* 1989] S. Ishida, S. Fujii, N. Shinmura and S. Asano. Site preference of the M atom in $(Fe_{1-x}M_x)_3Ga$ (M identical to Cr, Mn, Co or Ni). **J. Phys.:Condens. Matter**, vol. 1, page 5115, 1989.

[Ishida *et al.* 1995] S. Ishida, S. Fujii, S. Kashiwagi and S. Asano. Search for Half-Metallic Compounds in Co_2MnZ (Z=IIIb, IVb, Vb Element). **J. Phys. Soc. Jpn.**, vol. 64, page 2152, 1995.

[Itoh *et al.* 2000] H. Itoh, T. Ohsawa and J. Inouc. Magnetoresistance of Ferromagnetic Tunnel Junctions in the Double-Exchange Model. **Phys. Rev. Lett.**, vol. 84, page 2501, 2000.

[Jepsen *et al.* 1978] O. Jepsen, J. Madesen and O. K. Andersen. Band structure of thin films by the linear augmented-plane-wave method. **Phys. Rev. B**, vol. 18, page 605, 1978.

[Kämmerer *et al.* 2004] S. Kämmerer, A. Thomas, A. Hütten and G. Reiss. Co_2MnSi Heusler alloy as magnetic electrodes in magnetic tunnel junctions. **Appl. Phys. Lett.**, vol. 85, page 79, 2004.

[Katsnelson *et al.* 2008] M. I. Katsnelson, V. Yu. Irkhin, L. Chioncel, A. I. Lichtenstein and R. A. de Groot. Half-metallic ferromagnets: From band structure to many-body effects. **Rev. Mod. Phys.**, vol. 80, no. 2, pages 315–378, 2008.

[Kilian and Victora 2000] K. A. Kilian and R. H. Victora. Electronic structure of Ni_2MnIn for use in spin injection. **J. Appl. Phys.**, vol. 87, page 7064, 2000.

[Kino *et al.* 2003] H. Kino, F. Aryasetiawan, I. Solovyev, T. Miyake, T. Ohno and K. Terakura. GW study of half-metallic electronic structure of $La_{0.7}Sr_{0.3}MnO_3$. **Physica B**, vol. 329-333, page 858, 2003.

[Koelling and Arbman 1975] D. D. Koelling and G. O. Arbman. Use of energy derivative of the radial solution in an augmented plane wave method: application to copper. **J. Phys. F: Met. Phys.**, vol. 5, page 2041, 1975.

[Koelling and Harmon 1977] D. D. Koelling and B. N. Harmon. A technique for relativistic spin-polarised calculations. **J. Phys. C**, vol. 10, page 3107, 1977.

[Kohn and Sham 1965] W. Kohn and L. J. Sham. Self-Consistent Equations Including Exchange and Correlation Effects. **Phys. Rev.**, vol. 140, page A1133, 1965.

[Kübler *et al.* 1983] J. Kübler, A. R. William and C. B. Sommers. Formation and coupling of magnetic moments in Heusler alloys. **Phys. Rev. B**, vol. 28, no. 4, page 1745, 1983.

[Kuneš *et al.* 2001] J. Kuneš, P. Novák, R. Schmid, P. Blaha and K. Schwarz. Electronic structure of fcc Th: Spin-orbit calculation with $6p_{1/2}$ local orbital extension. **Phys. Rev. B**, vol. 64, no. 15, page 153102, 2001.

[Lakshmi *et al.* 1993] N. Lakshmi, K. Venngopalan and J. Varma. Hyperfine-field studies of Fe_3Al and $Fe_{3-x}Cr_xAl$ alloys. **Phys. Rev. B**, vol. 47, no. 21, page 14054, 1993.

[Lechermann *et al.* 2002] F. Lechermann, F. Welsch, C. Elsasser, C. Ederer, M. Fahnle, J. M. Sanchez and B. Meyer. Density-functional study of Fe_3Al: LSDA versus GGA. **Phys. Rev. B**, vol. 65, page 132104, 2002.

[Lehmann *et al.* 1970] G. Lehmann, P. Rennert, M. Taut and H. Wonn. Elektronenzustandsdichte in der Lavesphase $MgZn_2$. **Phys. Status Solidi**, vol. 37, page K27, 1970.

[Ležaić *et al.* 2006] M. Ležaić, Ph. Mavropoulos, J. Enkovaara, G. Bihlmayer and S. Blügel. Thermal Collapse of Spin Polarization in Half-Metallic Ferromagnets. **Phys. Rev. Lett.**, vol. 97, no. 2, page 026404, 2006.

[Liberman *et al.* 1965] D. Liberman, J. T. Waber and D. T. Cromer. Self-Consistent-Field Dirac-Slater Wave Functions for Atoms and Ions. I. Comparison with Previous Calculations. **Phys. Rev.**, vol. 137, page A27, 1965.

[Liu *et al.* 2006] G. D. Liu, X. F. Dai, S. Y. Yu, Z. Y. Zhu, J. L. Chen, G. H. Wu, H. Zhu and John Q. Xiao. Physical and electronic structure and magnetism of Mn_2NiGa: Experiment and density-functional theory calculations. **Phys. Rev. B**, vol. 74, page 054435, 2006.

[Luo *et al.* 2008] H. Z. Luo, H. W. Zhang, Z. Y. Zhu, L. Ma, S. F. Xu, G. H. Wu, X. X. Zhu, C. B. Jiang and H. B. Xu. Half-metallic properties for the Mn_2FeZ (Z = Al, Ga, Si, Ge, Sb) Heusler alloys: A first-principles study. **J. Appl. Phys.**, vol. 103, page 083908, 2008.

[Luo *et al.* 2009] Hongzhi Luo, Guodong Liu, Zhongqiu Feng, Yangxian Li, Li Ma, Guangheng Wu, Xiaoxi Zhu, Chengbao Jiang and Huibin Xu. Effect of the main-group elements on the electronic structures and magnetic properties of Heusler alloys Mn_2NiZ (Z = In, Sn, Sb). **J. Magn. Magn. Mater.**, vol. 321, page 4063, 2009.

[MacDonald *et al.* 1980] A H MacDonald, W E Picket and D D Koelling. A linearised relativistic augmented-plane-wave method utilising approximate pure spin basis functions. **J. Phys. C: Solid State Phys.**, vol. 13, no. 14, page 2675, 1980.

[Mancoff *et al.* 1999] F. B. Mancoff, B. M. Clemens, E. J. Singley and D. N. Basov. Infrared probe of the electronic structure and carrier scattering in NiMnSb thin films. **Phys. Rev. B**, vol. 60, page R12565, 1999.

[Martin 2004] Richard M. Martin. **Electronic structure: Basic theory and practical methods**. Cambridge University Press, 2004.

[Mavropoulos *et al.* 2004] Ph. Mavropoulos, K. Sato, R. Zeller, P. H. Dederichs, V. Popescu and H. Ebert. Effect of the spin-orbit interaction on the band gap of half metals. **Phys. Rev. B**, vol. 69, no. 5, page 054424, 2004.

[Mazin 1999] I. I. Mazin. How to Define and Calculate the Degree of Spin Polarization in Ferromagnets. **Phys. Rev. Lett.**, vol. 83, no. 7, page 1427, 1999.

[Mermin 1965] N. David Mermin. Thermal properties of the inhomogeneous electron gas. **Phys. Rev.**, vol. 137, page A1441, 1965.

[Monkhorst *et al.* 1976] Hendrik J. Monkhorst and James D. Pack. Special points for Brillouin-zone integrations. **Phys. Rev. B**, vol. 13, no. 12, page 5188, 1976.

[Moodera *et al.* 1995] J. S. Moodera, Lisa R. Kinder, Terrilyn M. Wong and R. Meservey. Large Magnetoresistance at Room Temperature in Ferromagnetic Thin Film Tunnel Junctions. **Phys. Rev. Lett.**, vol. 74, no. 16, page 3273, 1995.

[Murnaghan 1944] F. D. Murnaghan. The Compressibility of Media under Extreme Pressures. **Proc. Natl. Acad. Sci.**, vol. 30, page 244, 1944.

[Nadgorny *et al.* 2001] B. Nadgorny, I. I. Mazin, M. Osofsky, R. J. Soulen, P. Broussard, R. M. Stroud, D. J. Singh, V. G. Harris, A. Arsenov and Ya. Mukovskii. Origin of high transport spin polarization in $La_{0.7}Sr_{0.3}MnO_3$: Direct evidence for minority spin states. **Phys. Rev. B**, vol. 63, no. 18, page 184433, 2001.

[Niculescu *et al.* 1983] V. A. Niculescu, T. J. Burch and J. I. Budnick. A local environment description of hyperfine fields and atomic moments in $Fe_{3-x}T_xSi$ alloys. **J. Magn. Magn. Mater.**, vol. 39, page 223, 1983.

[Nishino *et al.* 1997] Y. Nishino, M. Kato, S. Asano, K. Soda, M. Hayasaki and U. Mizutani. Semiconductorlike Behavior of Electrical Resistivity in Heusler-type Fe_2VAl Compound. **Phys. Rev. Lett.**, vol. 79, no. 10, page 1909, 1997.

[Nozieres 1964] P. Nozieres. **Theory of interacting fermi systems**. Benjamin, New York, 1964.

[Orgassa *et al.* 1999] D. Orgassa, H. Fujiwara, T. C. Schulthess and W. H. Bulter. First-principles calculation of the effect of atomic disorder on the electronic structure of the half-metallic ferromagnet NiMnSb. **Phys. Rev. B**, vol. 60, page 13237, 1999.

[Otto *et al.* 1989] M. J. Otto, R. A. M. van Woerden, P. J. van der Valk, J. Wijngaard, C. F. van Bruggen and C. Haas. Half-metallic ferromagnets. II. Transport properties of NiMnSb and related inter-metallic compounds. **J. Phys.:Condens. Matter**, vol. 1, page 2351, 1989.

[Özdogan *et al.* 2006] K. Özdogan, I. Galanakis, E. Sasioglu and B. Aktas. Search for half-metallic ferrimagnetism in V-based Heusler alloys Mn_2VZ (Z = Al, Ga, In, Si, Ge, Sn). **J. Phys.:Condens. Matter**, vol. 18, page 2905, 2006.

[Pack and Monkhorst 1977] James D. Pack and Hendrik J. Monkhorst. "Special points for Brillouin-zone integrations"—a reply. **Phys. Rev. B**, vol. 16, no. 4, pages 1748–1749, 1977.

[Park *et al.* 1998] J. H. Park, E. Vescovo, H. J. Kim, C. Kwon, R. Ramesh and T. Venkatesan. Direct evidence for a half-metallic ferromagnet. **Nature(London)**, vol. 392, page 794, 1998.

[Pecharsky and Gschneidner 1997] V. K. Pecharsky and jr. K. A. Gschneidner. Giant Magnetocaloric Effect in $Gd_5(Si_2Ge_2)$. **Phys. Rev. Lett.**, vol. 78, page 4494, 1997.

[Perdew *et al.* 1996] John P. Perdew, Kieron Burke and Matthias Ernzerhof. Generalized Gradient Approximation Made Simple. **Phys. Rev. Lett.**, vol. 77, no. 18, pages 3865–3868, 1996.

[Picozzi *et al.* 2002] S. Picozzi, A. Continenza and A. J. Freeman. Co_2MnX(X=Si, Ge, Sn) Heusler compounds: An ab initio study of their structural, electronic, and magnetic properties at zero and elevated pressure. **Phys. Rev. B**, vol. 66, page 094421, 2002.

[Picozzi *et al.* 2004] S. Picozzi, A. Continenza and A. J. Freeman. Role of structural defects on the half-metallic character of Co_2MnGe and Co_2MnSi Heusler alloys. **Phys. Rev. B**, vol. 69, page 094423, 2004.

[Pierre *et al.* 1993] J. Pierre, R. V. Skolozdra and Yu. V. Stadnyk. Influence of cobalt vacancies and nickel substitution on the magnetic properties of $TiCo_2Sn$ Heusler-type compound. **J. Magn. Magn. Mater.**, vol. 128, page 93, 1993.

[Prinz 1998] Gary A. Prinz. Magnetoelectronics. **Science**, vol. 282, page 1660, 1998.

[Pugaczowa-Michalska *et al.* 2005] M. Pugaczowa-Michalska, A. Go and L. Dobrzynski. Electronic structure and magnetism of $Fe_{3-x}Mn_xAl$ alloys. **phys. stat. sol. (b)**, vol. 242, no. 2, pages 463, 2005.

[Ritche *et al.* 2003] L. Ritche, G. Xiao, Y. Ji, T. Y. Chen, C. L. Chien, M. Zhang, J. Chen, Z. Liu, G. Wu and X. X. Zhang. Magnetic, structural, and transport properties of the Heusler alloys Co_2MnSi and NiMnSb. **Phys. Rev. B**, vol. 68, page 104430, 2003.

[Rodriquez-Carvajal 1993] J. L. Rodriquez-Carvajal. Recent Advances in Magnetic Structure Determination by Neutron Powder Diffraction. **Physica B**, vol. 192, page 55, 1993.

[Sandratskii 2001] L. M. Sandratskii. Magnetic structure of relativistic systems with low symmetry. **Phys. Rev. B**, vol. 64, no. 13, page 134402, 2001.

[Sanvito and Hill 2000] Stefano Sanvito and Nicola A. Hill. Ground state of half-metallic zinc-blende MnAs. **Phys. Rev. B**, vol. 62, no. 23, pages 15553, 2000.

[Sasioglu *et al.* 2005] E. Sasioglu, L. M. Sandratskii and P. Bruno. First-principles study of exchange interactions and Curie temperatures of half-metallic ferrimagnetic full Heusler alloys Mn_2VZ (Z = Al, Ge). **J. Phys.:Condens. Matter**, vol. 17, page 995, 2005.

[Satua *et al.* 1993] D. Satua, K. Szymaski, L. Dobrzyski and J. Waliszewski. Mössbauer study of $Fe_{3-x}Cr_xSi$ alloys with DO_3-type ordering. **J. Magn. Magn. Mater.**, vol. 119, no. 3, page 309, 1993.

[Schlomka *et al.* 2000] J. P. Schlomka, M. Tolan and W. Press. In situ growth study of NiMnSb films on MgO(001) and Si(001). **Appl. Phys. Lett.**, vol. 76, page 2005, 2000.

[Schmidt *et al.* 2000] G. Schmidt, D. Ferrand, L. W. Molenkamp, A. T. Filip and B. J. van Wees. Fundamental obstacle for electrical spin injection from a ferromagnetic metal into a diffusive semiconductor. **Phys. Rev. B**, vol. 62, page R4790, 2000.

[Schwarz 1986] K. Schwarz. CrO_2 predicted as a half-metallic ferromagnet. **J. Phys. F: Met. Phys.**, vol. 16, page L211, 1986.

[Shishidou *et al.* 2001] Tatsuya Shishidou, A. J. Freeman and Ryoji Asahi. Effect of GGA on the half-metallicity of the itinerant ferromagnet CoS_2. **Phys. Rev. B**, vol. 64, no. 18, page 180401, 2001.

[Singh 1989] D. Singh. Simultaneous solution of diagonalization and self-consistency problems for transition-metal systems. **Phys. Rev. B**, vol. 40, page 5428, 1989.

[Singh 1991] D. Singh. Ground-state properties of lanthanum: Treatment of extended-core states. **Phys. Rev. B**, vol. 43, page 6388, 1991.

[Singh *et al.* 2004] L. J. Singh, Z. H. Barder, Y. Miyoshi, Y. Bugoslavsky, W. R. Branford and L. F. Cohen. Structural, magnetic, and transport properties of thin films of the Heusler alloy Co_2MnSi. **Appl. Phys. Lett.**, vol. 84, page 2367, 2004.

[Singh *et al.* 2006] L. J. Singh, Z. H. Barder, A. Kohn, A. K. Petford-Long, Y. Miyoshi, Y. Bugoslavsky and L. F. Cohen. Interface effects in highly oriented films of the Heusler alloy Co_2MnSi on GaAs(001). **J. Appl. Phys.**, vol. 99, page 013904, 2006.

[Sjöstedt *et al.* 2000] E. Sjöstedt, L. Nordström and D. J. Singh. An alternative way of linearizing the augmented plane-wave method. **Solid State Commun.**, vol. 114, page 15, 2000.

[Skomski 2007] R. Skomski. Finite-temperature depolarization in half metals. **J. Phys.:Condens. Matter**, vol. 19, page 315202, 2007.

[Slater 1937] J. C. Slater. Wave Functions in a Periodic Potential. **Phys. Rev.**, vol. 51, no. 10, pages 846, 1937.

[Slater 1951] J. C. Slater. A Simplification of the Hartree-Fock Method. **Phys. Rev.**, vol. 81, no. 3, pages 385, 1951.

[Soulen *et al.* 1998] R. J. Soulen, Jr., J. M. Byers, M. S. Osofsky, B. Nadgorny, T. Ambrose, S. F. Cheng, P. R. Broussard, C. T. Tanaka, J. Nowak, J. S. Moodera, A. Berry and J. M. D. Coey. Measuring the Spin Polarization of a Metal with a Superconducting Point Contact. **Science**, vol. 282, page 85, 1998.

[Ślebarski *et al.* 2000] A. Ślebarski, M. B. Maple, E. J. Freeman, C. Sirvent, D. Tworuszka, M. Orzechowska, A. Wrona, A. Jezierski, S. Chiuzbaian and M. Neumann. Weak ferromagnetism induced by atomic disorder in Fe_2TiSn. **Phys. Rev. B**, vol. 62, no. 5, pages 3296, 2000.

[Takizawa *et al.* 2002] H. Takizawa, T. Yamashita, K. Uheda and T. Endo. High-pressure synthesis of ferromagnetic Mn_3Ge with the Cu_3Au-type structure. **J. Phys.:Condens. Matter**, vol. 14, page 11147, 2002.

[Tanaka *et al.* 1999] C. T. Tanaka, J. Nowak and J. S. Moodera. Spin-polarized tunneling in a half-metallic ferromagnet. **J. Appl. Phys.**, vol. 86, page 6239, 1999.

[Thomas 1926] L. H. Thomas. The calculation of atomic fields. **Proc. Campridge Philos. Soc.**, vol. 23, page 542, 1926.

[Tobola *et al.* 1996] J. Tobola, J. Pierre, S. Kaprzyk, R. V. Skolozdra and M. A. Kouacou. Electronic structure and magnetism in Co—Ni Heusler compounds. **J. Magn. Magn. Mater.**, vol. 159, page 192, 1996.

[van Engen *et al.* 1983] P. G. van Engen, K. H. J. Buschow and M. Erman. Magnetic properties and magneto-optical spectroscopy of Heusler alloys based on transition metals and Sn. **J. Magn. Magn. Mater.**, vol. 30, page 374, 1983.

[Vinesh *et al.* 2009] A. Vinesh, Hina Bhargava, N. Lakshmi and K. Venugopalan. Magnetic anisotropy induced by high energy ball milling of Fe_2MnAl. **J. Appl. Phys.**, vol. 105, page 07A309, 2009.

[von Barth and Hedin 1972] U. von Barth and L. Hedin. A local exchange-correlation potential for the spin polarized case. i. **J. Phys. C**, vol. 5, page 1629, 1972.

[Vonsovsky and Katsnelson 1989] S. V. Vonsovsky and M. I. Katsnelson. **Quantum solid state physics**. Springer, Berlin, 1989.

[Watson and Freeman 1961] R. E. Watson and A. J. Freeman. Origin of Effective Fields in Magnetic Materials. **Phys. Rev.**, vol. 123, no. 6, pages 2027, 1961.

[Webster *et al.* 1984] P. J Webster, K. R. A. Ziebeck, S. L. Town and M. S. Peak. Magnetic Order and Phase Transformation in Ni_2MnGa. **Phil. Mag. B**, vol. 49, page 295, 1984.

[Weht and Pickett 1999] Ruben Weht and Warren E. Pickett. Half-metallic ferrimagnetism in Mn_2VAl. **Phys. Rev. B**, vol. 60, no. 18, pages 13006, 1999.

[Weinert 1981] M. Weinert. Solution of Poissons equation: Beyond Ewald-type methods. **J. Math. Phys.**, vol. 22, page 2433, 1981.

[Weinert *et al.* 1982] M. Weinert, E. Wimmer and A. J. Freeman. Total-energy all-electron density functional method for bulk solids and surfaces. **Phys. Rev. B**, vol. 26, page 4571, 1982.

[Wiesendanger *et al.* 1990] R. Wiesendanger, H.-J. Güntherodt, G. Güntherodt, R. J. Gambino and R. Ruf. Observation of vacuum tunneling of spin-polarized electrons with the scanning tunneling microscope. **Phys. Rev. Lett.**, vol. 65, no. 2, pages 247, 1990.

[Wimmer *et al.* 1981] E. Wimmer, H. Krakauer and A. J. Freeman. Full-potential self-consistent linearized-augmented-plane-wave method for calculating the electronic structure of molecules and surfaces: O_2 molecule. **Phys. Rev. B**, vol. 24, page 864, 1981.

[Wurmehl *et al.* 2005] Sabine Wurmehl, Gerhard H. Fecher, Hem C. Kandpal, Vadim Ksenofontov, Claudia Felser, Hong-Ji Lin and Jonder Morais. Geometric, electronic, and magnetic structure of Co_2FeSi : Curie temperature and magnetic moment measurements and calculations. **Phys. Rev. B**, vol. 72, no. 18, page 184434, 2005.

[Xie *et al.* 2003] Wen-Hui Xie, Ya-Qiong Xu, Bang-Gui Liu and D. G. Pettifor. Half-Metallic Ferromagnetism and Structural Stability of Zincblende Phases of the Transition-Metal Chalcogenides. **Phys. Rev. Lett.**, vol. 91, no. 3, page 037204, 2003.

[Yamashita *et al.* 2003] T. Yamashita, H. Takizawa, T. Sasaki, K. Uheda and T. Endo. **J. Alloys and compounds**, vol. 348, page 220, 2003.

[Yu *et al.* 1991] R. Yu, D. Singh and H. Krakauer. All-electron and pseudopotential force calculations using the linearized-augmented-plane-wave method. **Phys. Rev. B**, vol. 43, page 6411, 1991.

[Zhou and Bakker 1995] G. F. Zhou and H. Bakker. Phase Transformation in the $L1_2$-Structure of Fe_3Ge Driven by Mechanical Milling. **Europhys. Lett**, vol. 30, no. 7, page 433, 1995.

[Ziese and Thompson 2001] M. Ziese and M. Thompson. **Spin electronics**. Springer series. Springer-Verlag, 2001.

[Ẑutić *et al.* 2004] I. Ẑutić, J. Fabian and S. Das Sarma. Spintronics: Fundamentals and applications. **Rev. Mod. Phys.**, vol. 76, page 323, 2004.

APPENDIX A

WIEN2K PACKAGE AND PARALLEL CALCULATIONS

A.1 WIEN2k Package

The main programs in the Wien2k code:

1. **Initialization process**

   It is used to prepare the needed files to start the main calculations

   (a) **LSTART** (atomic LSDA program)

   It is a relativistic atomic LSDA code. LSTART generates atomic densities which are used by **DSTART** to generate a starting density for a scf calculation and all the input files for the scf run. In addition it creates atomic potentials and optional atomic valence densities. Relativistic quantum numbers [Liberman *et al.* 1965]

   Table A.1.1 tabulate the relativistic quantum numbers which are defined as follows:

   Spin quantum number: s= +1 or s= -1

   Orbital quantum number j= l + s/2

   Relativistic quantum number κ = -s(j + 1/2)

   (b) mixing factor(α)

   The simplest mixing scheme is straight mixing:

$$\rho_{in}^{i+1} = (1-\alpha)\rho_{in}^{i} + \alpha\rho_{out}^{i}$$

(c) **DSTART** (Superposition of atomic densities)

It is generates an initial crystalline charge density by a superposition of atomic densities generated with **lstart**.

2. **Programs for running an scf cycle**

(a) **LAPW0** (generates potential)

This program computes the total potential V_{tot} as the sum of the Coulomb V_c and the exchange-correlation potential V_{xc} using the total electron (spin) density as input. It generates the spherical part (l=0) and the non-spherical part for both spin channels. The Coulomb potential is calculated by the multipolar Fourier expansion [Weinert 1981] and the exchange-correlation potential is calculated numerically on a grid. Inside the atomic spheres a least squares procedure is used to reproduce the potential using a lattice harmonics representation. In the interstitial region a 3-D fast Fourier transformation (FFT) is used. The integral of the form $\rho*V$ is calculated according to Weinert formalism [Weinert *et al.* 1982]. The Hellmann-Feynman force contribution to the total force is also calculated [Yu *et al.* 1991].

(b) **LAPW1** (generates eigenvalues and eigenvectors)

This program sets up the Hamiltonian and the overlap matrix [Koelling and Arbman 1975] and finds the diagonalization eigenvalues and eigenvectors. The diagonalization is the most time consuming

Table A.1.1. Relativistic quantum numbers

		j=l+s/2		κ		max. occupation	
	l	s=-1	s=+1	s=-1	s=+1	s=-1	s=+1
s	0		$\frac{1}{2}$		-1		2
p	1	$\frac{1}{2}$	$\frac{3}{2}$	1	-2	2	4
d	2	$\frac{3}{2}$	$\frac{5}{2}$	2	-3	4	6
f	3	$\frac{5}{2}$	$\frac{7}{2}$	3	-4	6	8

part of the calculations. In wien2k we used two kinds of diagonalization: First, full diagonalization (highly optimized modifications of LAPACK routines). Second, iterative diagonalization (a block-Davdson method [Singh 1989]).

(c) **LAPW2** (generates valence charge density expansions)
It is computes the Fermi energy and the expansions of the electronic charge densities for each occupied state and each k-point.

(d) **LCORE** (generates core states)
It is a relativistic LSDA atomic code to calculate the core states (relativistically including SO, or non-relativistically if NREL calculations) for the spherical part of the potential.

(e) **MIXER** (adding and mixing of charge densities)
This program adds the electron densities of core, semi-core, and valence states to yield the total new output density. To keep stability in the iterative SCF process the new output density are mixed with the old input density to obtain new density to be used in the next iteration.

The self-consistency cycle is illustrated in Fig. A.1.1. While Fig. A.1.2 illustrate the flow and usage of the different programs in Wien2k.

Computational Considerations

In the newest version WIEN2k the alternative basis set (APW+lo) is used the atomic spheres for the chemically important orbitals, whereas LAPW is used for the others. In addition new algorithms for the computer intensive general eigensolver were implemented. The combination of algorithmic

developments and increased computer power has led to a significant improvement in the possibilities of simulating relatively large systems on moderate computer hardware. Now, PCs or a cluster of PCs can be used efficiently instead of the powerful workstations or supercomputers that were needed about a decade ago. Several considerations are essential for a modern computer code and were made in the development of the new WIEN2k package:

- Accuracy: extremely important in the present case. It is achieved by the well-balanced basis set, which contains numerical radial functions that are recalculated in each iteration cycle. Thus these functions adapt to effects due to charge transfer or hybridization, are accurate near the nucleus (important for the electric field gradient (EFG)) and satisfy the cusp condition. The plane-wave (PW) convergence can be essentially controlled by one parameter, namely the cutoff energy corresponding to the highest PW component. There is no dependence on selecting atomic orbitals or pseudo-potentials. It is a full-potential and all electron method. Relativistic effects (including spin orbit coupling) can be treated with a quality comparable to solving Diracs equation. All atoms in the periodic table can be handled.

- Efficiency and good performance: should be as high as possible. The new mixed basis APW+lo/LAPW optimally satisfies this criterion. The smaller matrix size helps to save computer time and thus larger systems can be studied.

- Parallelization: the program can run in parallel, either in a coarse grain version where each k-point is computed on a single processor, or if the memory requirement is larger than that available on a single CPU in a fine grain scheme that requires special attention for the eigensolver, the most time consuming part. Both options, full and iterative diagonalization, are implemented to (automatically) select the most efficient routines.

- Architecture: the hardware in terms of processor speed, memory access and communication is crucial. Depending on the given architecture, optimized algorithms and libraries are used during installation of the program package.

- Portability: requires the use of standards as far as possible, such as FORTRAN90, Message Passing Interface (MPI), Basic Linear Algebra Subprograms (BLAS) -(level 3), Scalable Linear Algebra PACKage (SCALAPACK), etc.

- User friendliness: is achieved by a web based graphical user interface (GUI), called w2web. The program package provides an automatic choice of default options and is complemented by an extensive Users Guide.

A.2 Parallel calculation

There are three methods for running Wien2k on parallel computers:

1. k-points parallelization

   parallelizing k-points over processors, utilizes c-shell scripts. By distributing subsets of the k-mesh to different processors and subsequent summation of the results. Figures A.2.3 and A.2.4 show how files are handled by the scripts in Wien2k.

2. MPI Fine grained parallelization

   MPI parallelization is based on parallelization libraries, including MPI, Scalapack and PBlas.

3. Hybrid parallelization

   Hybrid parallelization does both k-point parallelization and MPI parallelization.

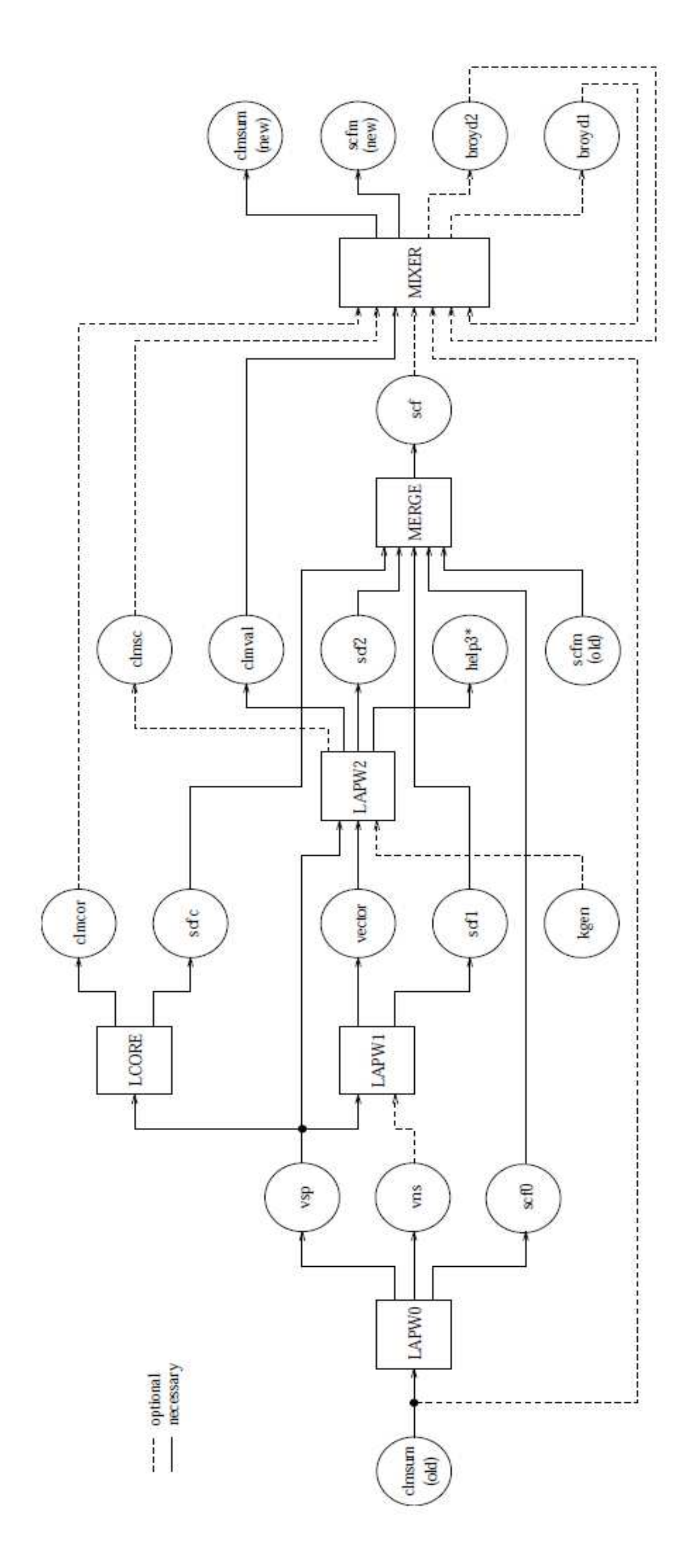


Figure A.1.1. Data flow during a SCF cycle in Wien2k.

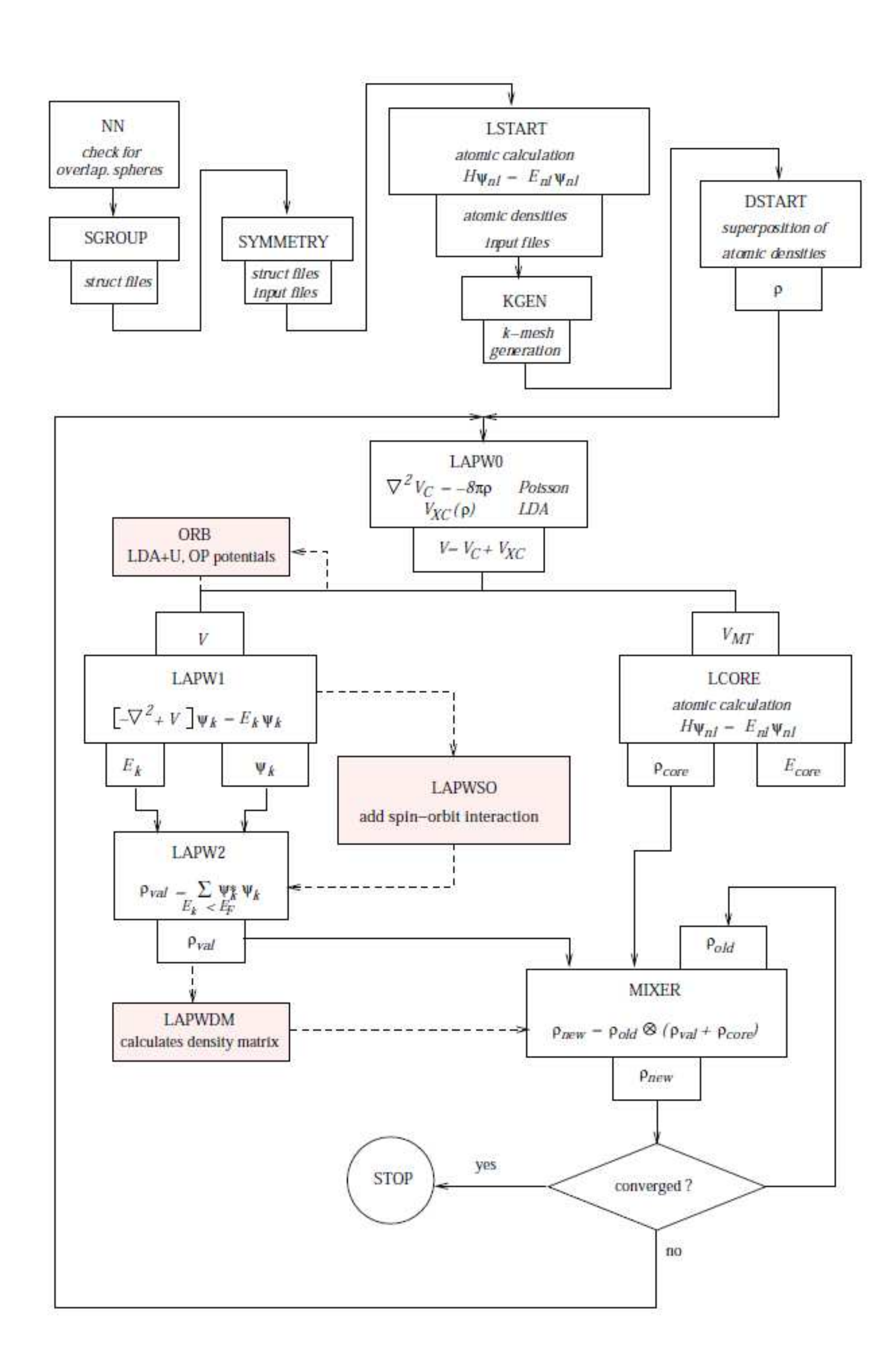


Figure A.1.2. Program flow in Wien2k.

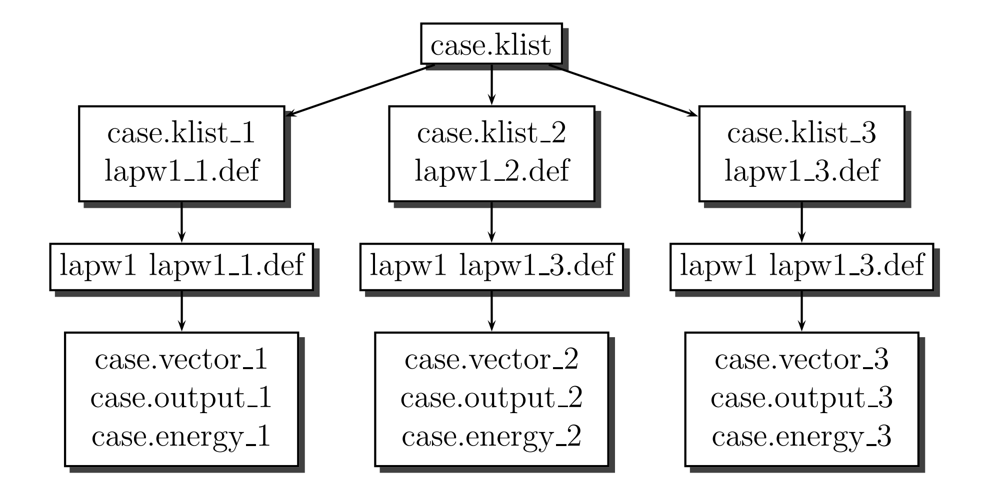


Figure A.2.3. Flow chart of lapw1para in Wien2k.

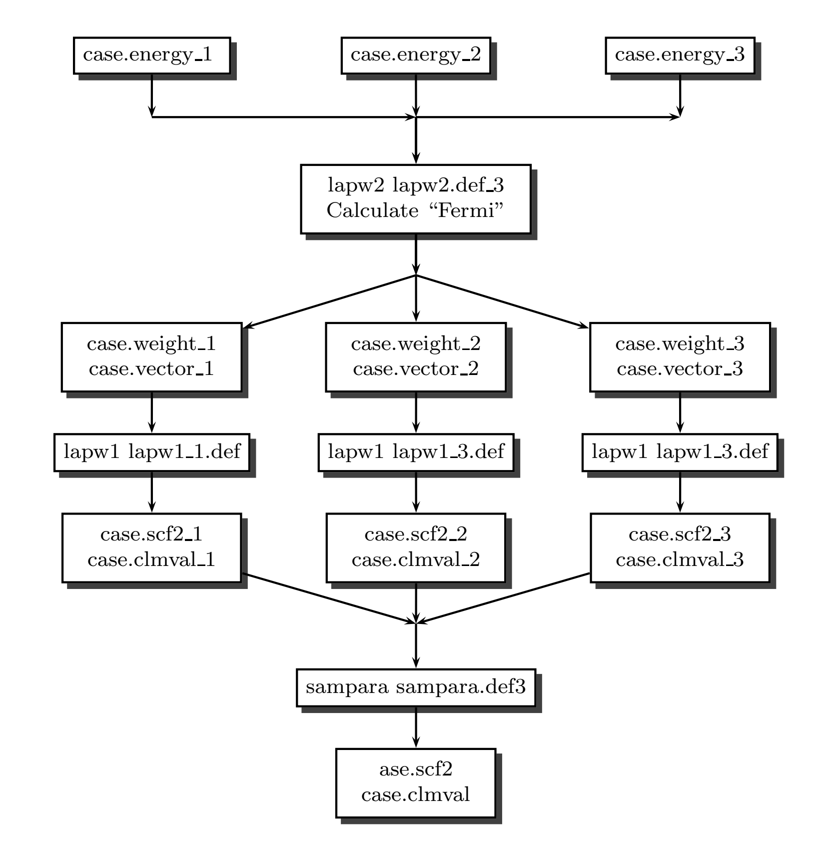


Figure A.2.4. Flow chart of lapw2para in Wien2k.

APPENDIX B

SPACE GROUP AND WYCKOFF POSITIONS

B.1

In this appendix, tabulated the space groups and their Wyckoff positions that used in the different compositions which were carried out in our calculations.

Table B.1.1. Multiplicity, Wyckoff position, site symmetry and coordinates for (123) P4/mmm space group.

(225) Fm$\bar{3}$m			
Multiplicity	Wyckoff Positions	Site Symmetry	Coordinates
1	a	4/mmm	(0,0,0)
1	b	4/mmm	$(0,0,\frac{1}{2})$
1	c	4/mmm	$(\frac{1}{2},\frac{1}{2},0)$
1	d	4/mmm	$(\frac{1}{2},\frac{1}{2},\frac{1}{2})$
4	i	2mm	$(0,\frac{1}{2},\frac{1}{4})(\frac{1}{2},0,\frac{1}{4})(0,\frac{1}{2},\frac{3}{4})(\frac{1}{2},0,\frac{3}{4})$

Table B.1.2. Multiplicity, Wyckoff position, site symmetry and coordinates for (134) $P4_2/nnm$ (two origins) space group.

(134) $P4_2$/nnm (two origins)			
Multiplicity	Wyckoff Positions	Site Symmetry	Coordinates
2	a	-42m	$(\frac{1}{4},\frac{3}{4},\frac{1}{4})$ $(\frac{3}{4},\frac{1}{4},\frac{3}{4})$
2	b	-42m	$(\frac{3}{4},\frac{1}{4},\frac{1}{4})$ $(\frac{1}{4},\frac{3}{4},\frac{3}{4})$
4	c	222.	$(\frac{1}{4}),\frac{1}{4},\frac{1}{4})$ $(\frac{1}{4},\frac{1}{4},\frac{3}{4})$ $(\frac{3}{4},\frac{3}{4},\frac{3}{4})$ $(\frac{3}{4},\frac{3}{4},\frac{1}{4})$
4	f	..2/m	(0,0,0) $(\frac{1}{2},\frac{1}{2},0)$ $(\frac{1}{2},0,\frac{1}{2})$ $(0,\frac{1}{2},\frac{1}{2})$
4	e	..2/m	$(0,0,\frac{1}{2})$ $(\frac{1}{2},\frac{1}{2},\frac{1}{2})$ $(\frac{1}{2},0,0)$ $(0,\frac{1}{2},0)$

Table B.1.3. Multiplicity, Wyckoff position, site symmetry and coordinates for (215) $P\bar{4}3m$ space group.

(215) $P\bar{4}3m$			
Multiplicity	Wyckoff Positions	Site Symmetry	Coordinates
1	a	-43m	(0,0,0)
1	b	-43m	$(\frac{1}{2},\frac{1}{2},\frac{1}{2})$
3	c	-42.m	$(0,\frac{1}{2},\frac{1}{2})(\frac{1}{2},0,\frac{1}{2})(\frac{1}{2},\frac{1}{2},0)$
3	d	-42.m	$(0,0,\frac{1}{2})(\frac{1}{2},0,0)(0,\frac{1}{2},0)$
4	e	.3m	$(\frac{1}{4},\frac{1}{4},\frac{1}{4})(\frac{3}{4},\frac{3}{4},\frac{1}{4})(\frac{3}{4},\frac{1}{4},\frac{3}{4})(\frac{1}{4},\frac{3}{4},\frac{3}{4})$
4	e	.3m	$(\frac{3}{4},\frac{3}{4},\frac{3}{4})(\frac{1}{4},\frac{1}{4},\frac{3}{4})(\frac{1}{4},\frac{3}{4},\frac{1}{4})(\frac{3}{4},\frac{1}{4},\frac{1}{4})$

Table B.1.4. Multiplicity, Wyckoff position, site symmetry and coordinates for (216) $F\bar{4}3m$ space group.

(216) $F\bar{4}3m$			
Multiplicity	Wyckoff Positions	Site Symmetry	Coordinates
1	a	-43m	(0,0,0)
1	b	-43m	$(\frac{1}{4},\frac{1}{4},\frac{1}{4})$
3	c	-42.m	$(\frac{1}{2},\frac{1}{2},\frac{1}{2})$
3	d	-42.m	$(\frac{3}{4},\frac{3}{4},\frac{3}{4})$

Table B.1.5. Multiplicity, Wyckoff position, site symmetry and coordinates for (221) Pm$\bar{3}$m space group.

(221) Pm$\bar{3}$m			
Multiplicity	Wyckoff Positions	Site Symmetry	Coordinates
1	a	m-3m	(0,0,0)
1	b	m-3m	$(\frac{1}{2}, \frac{1}{2}, \frac{1}{2})$
3	c	4/mm.m	$(0,\frac{1}{2}, \frac{1}{2})(\frac{1}{2}, 0, \frac{1}{2})(\frac{1}{2}, \frac{1}{2},0)$
3	d	4mm.m	$(0,0,\frac{1}{2})(\frac{1}{2}, 0, 0)(0, \frac{1}{2},0)$
8	g	.3m	$(\frac{1}{4}, \frac{1}{4}, \frac{1}{4})(\frac{3}{4}, \frac{3}{4}, \frac{1}{4})(\frac{3}{4}, \frac{1}{4}, \frac{3}{4})(\frac{1}{4}, \frac{3}{4}, \frac{3}{4})$ $(\frac{3}{4}, \frac{3}{4}, \frac{3}{4})(\frac{1}{4}, \frac{1}{4}, \frac{3}{4})(\frac{1}{4}, \frac{3}{4}, \frac{1}{4})(\frac{3}{4}, \frac{1}{4}, \frac{1}{4})$

Table B.1.6. Multiplicity, Wyckoff position, site symmetry and coordinates for (224) Pn$\bar{3}$m space group.

(224) Pn$\bar{3}$m			
Multiplicity	Wyckoff Positions	Site Symmetry	Coordinates
2	a	-43m	$(\frac{1}{4}, \frac{1}{4}, \frac{1}{4})(\frac{3}{4}, \frac{3}{4}, \frac{3}{4})$
4	b	.-3m	(0,0,0) $(\frac{1}{2}, \frac{1}{2}, 0)(\frac{1}{2}, 0, \frac{1}{2})(0, \frac{1}{2}, \frac{1}{2})$
4	c	.-3m	$(\frac{1}{2}, \frac{1}{2}, \frac{1}{2})(0, 0, \frac{1}{2})(0, \frac{1}{2}, 0)(\frac{1}{2},0,0)$
6	d	-42.m	$(\frac{1}{4}, \frac{3}{4}, \frac{3}{4})(\frac{3}{4}, \frac{1}{4}, \frac{3}{4})(\frac{3}{4}, \frac{1}{4}, \frac{3}{4})$ $(\frac{1}{4}, \frac{3}{4}, \frac{1}{4})(\frac{3}{4}, \frac{1}{4}, \frac{1}{4})(\frac{1}{4}, \frac{1}{4}, \frac{3}{4})$

Table B.1.7. Multiplicity, Wyckoff position, site symmetry and coordinates for (225) Fm$\bar{3}$m space group.

(225) Fm$\bar{3}$m			
Multiplicity	Wyckoff Positions	Site Symmetry	Coordinates
4	a	m-3m	(0,0,0)
4	b	m-3m	$(\frac{1}{2}, \frac{1}{2}, \frac{1}{2})$
8	c	-43m	$(\frac{1}{4}), \frac{1}{4}, \frac{1}{4})(\frac{1}{4}, \frac{1}{4}, \frac{3}{4})$

استقصاء السلوك نصف الفلزي والاستقطاب البرمي لسبائك هيسلر $Fe_{3-x}Mn_xZ(Z = Al, Ge, Sb)$: دراسة باستخدم المبادئ الأولية

إعداد
سعيد محمد شريف الأزعر

المشرف
الأستاذ الدكتور جميل محمود خليفة

المشرف المشارك
الدكتورة بثينة عبدالله حمد

استخدمنا في هذة الاطروحة نظرية الكثافة الداليّة (DFT) المبنية على طريقة الموجة المستوية المعدلة الخطية لجهد كامل (FPLAPW) ضمن تقريب الممال الاتجاهي المعمم (GGA) لدراسة الخصائص التركيبية، والإلكترونية والمغناطيسية لسبائك هيسلر $Fe_{3-x}Mn_xZ$ (Z = Al, Ge, Sb) حيث $(0< x < 3)$.

أظهرت بعض السبائك سلوكاً نصف فلزي من خلال تغيير تركيز المنغنيز وتغيير العنصر اللافلزي (Z) (ممثلة بأعداد تكافؤها المختلفة), فقد وجد أن السبائك التي يكون تركيز المنغنيز فيها أقل من 2 تظهر في الطور الفرومغناطيسي في حين أن الباقي تظهر في طور الفريمغناطيسي. أمّا العزم المغناطيسي البرمي الكلي فأظهر أتجاهاً يتوافق مع منحنى سلاتر-باولينغ حيث تتراوح قيمته بين صفر و أربعة (بور مغنتون), وتبين لنا أن معظم السبائك التي تركيز المنغنيز فيها اكبر من 1 تبدي سلوكاً نصف فلزي, تمّيزت بفجوات حزمة غير مباشرة على طول خط التماثل في المركبات ذات قيم $x =0, 1, 2, 3$. في حين ظهرت فجوات حزمة مباشرة في المركبات التي لها قيم x كسرية. لقد وجد ان السبائك الغنية بالمنغنيز تكون عالية الاستقطاب البرمي. ووجد كذلك ان المجال

فائق الدقة المغناطيسي على ذرة اللافلز يزداد بزيادة تركيز المنغنيز, حيث أنها تتغير من ‎-49.8 KG‎ عند ‎x=0‎ إلى ‎98.9 KG‎ عند ‎x=3‎ لسبائك التي تحتوي ألمنيوم, من ‎69.3 KG‎ عند ‎x=0‎ إلى ‎373.7 KG‎ عند ‎x=3‎ للسبائك التي تحتوي الجرمانيوم, من ‎220.2 KG‎ عند ‎x=0‎ إلى‎550.3 KG‎ عند ‎x=3‎ للسبائك التي تحتوي أنتيمون. أن القيم التي حسبناها للعزم المغناطيسي البرمي و المجال فائق الدقة المغناطيسي تتوافق بشكل جيد مع النتائج التجريبية السابقة.